Planetary and Space Science 127 (2016) 44–90

Contents lists available at ScienceDirect

Planetary and Space Science

journal homepage: www.elsevier.com/locate/pss

Review Article

Mars Express 10 years at Mars: Observations by the Mars Express Radio Science Experiment (MaRS)

M. Pätzold [a,*], B. Häusler [b], G.L. Tyler [c], T. Andert [b], S.W. Asmar [d], M.K. Bird [a], V. Dehant [e], D.P. Hinson [c], P. Rosenblatt [e], R.A. Simpson [c], S. Tellmann [a], P. Withers [f], M. Beuthe [e], A.I. Efimov [g], M. Hahn [a], D. Kahan [d], S. Le Maistre [e], J. Oschlisniok [a], K. Peter [a], S. Remus [h]

[a] Rheinisches Institut für Umweltforschung, Abteilung Planetenforschung, An der Universität Zu Köln, Cologne, Germany
[b] Institut für Raumfahrttechnik und Weltraumnutzung, Universität der Bundeswehr München, Neubiberg, Germany
[c] Department of Electrical Engineering, Stanford University, Stanford, CA, USA
[d] Jet Propulsion Laboratory, California Institute of Technology, Pasadena, CA, USA
[e] Royal Observatory of Belgium, Brussels, Belgium
[f] Astronomy Department, Boston University, Boston, MA, USA
[g] Kotel'nikov Institute of Radio Engineering & Electronics, Russian Academy of Science, 125009 Moscow, Russia
[h] ESA-ESTEC, Noordwijk, The Netherlands

ARTICLE INFO

Article history:
Received 3 March 2015
Received in revised form
19 February 2016
Accepted 26 February 2016
Available online 25 March 2016

Keywords:
Mars Express
Mars
Atmosphere
Ionosphere
Radio science
Radio occultation

ABSTRACT

The Mars Express spacecraft is operating in Mars orbit since early 2004. The Mars Express Radio Science Experiment (MaRS) employs the spacecraft and ground station radio systems (i) to conduct radio occultations of the atmosphere and ionosphere to obtain vertical profiles of temperature, pressure, neutral number densities and electron density, (ii) to conduct bistatic radar experiments to obtain information on the dielectric and scattering properties of the surface, (iii) to investigate the structure and variation of the crust and lithosphere in selected target areas, (iv) to determine the mass, bulk and internal structure of the moon Phobos, and (v) to track the MEX radio signals during superior solar conjunction to study the morphology of coronal mass ejections (CMEs). Here we report observations, results and discoveries made in the Mars environment between 2004 and 2014 over almost an entire solar cycle.

1. Introduction and science objectives

The Mars Express (MEX) spacecraft was inserted into Mars orbit on Christmas Day, 2003, arriving in its working orbit in mid January 2004 (Chicarro et al., 2004). Observations by the Mars Express Radio Science experiment (MaRS) began with the first Earth occultation season in April 2004 (Pätzold et al., 2004), following spacecraft and instrument commissioning. The prime mission continued through November 2005 (Pätzold et al., 2009), after which it was succeeded by four extensions of two years each. An additional extension, which would last until the end of 2018, is currently being negotiated.

MaRS employs the spacecraft and ground radio systems to:

(1) Conduct radio occultation observations of (a) the atmosphere to obtain vertical profiles of the neutral number density, pressure, and temperature as a function of height up to 30–50 km above the surface, and (b) vertical profiles of electron density from the base of the ionosphere at about 80 km to the ionopause, if detectable. Each profile provides the vertical structure at the time of observation parameterized by local time, season, solar longitude, planetary latitude and longitude, solar zenith angle, solar flux and activity proxy F10.7.
(2) Measure the oblique scattering properties of the Martian surface on the centimeter wavelength radio downlink—also referred to as bistatic radar (BSR). Such observations provide information on the dielectric and scattering properties of the surface in selected target areas by measuring the Fresnel reflectivity and the spectral dispersion of the echo signal.
(3) Investigate (a) the structure and variation of the crust and lithosphere in selected target areas, (b) the temporal evolution of the low–degree and order gravity coefficients resulting from seasonal mass exchange of volatiles between the poles, and (c) the mass, density, and interior structure of Phobos, from perturbations in the radio tracking data for information on the origin and evolution of the Martian moon.

* Corresponding author. Tel.: +49 221 27781810; fax: +49 221 4002320.
E-mail address: martin.paetzold@uni-koeln.de (M. Pätzold).

http://dx.doi.org/10.1016/j.pss.2016.02.013
0032-0633/

(4) Track the radio signals of the MEX spacecraft during superior solar conjunction to determine the large-scale morphology and turbulence of the solar corona. Particular emphasis is placed on detection and measurement of the electron content of coronal mass ejections (CMEs). The MaRS coronal sounding observations extend from 2004 to 2013, thereby covering almost an entire solar activity cycle.

2. Measurement methods, operational modes and constraints

MaRS observations were carried out with the same resources as for spacecraft tracking and navigation, primarily the use of ESA and US ground station antennas working in concert with the onboard spacecraft radio system for studies of Mars' atmosphere and gravity. In addition, observations of Mars' surface were obtained by the study of carom signals along a reflected MEX–Mars–Earth ray path.

The MaRS investigation was constrained by a combination of spacecraft limitations:

(1) The necessity of an uplink signal to provide the frequency stability required for precise radio occultation measurements on a coherent downlink limits the observations to only the entry phase of each occultation. The MaRS experiment was originally proposed to perform the atmospheric sounding experiments with a dual-frequency one-way downlink using an Ultrastable Oscillator (USO) to obtain the required frequency stability. Although the USO was endorsed by the German national space agency DLR, it was not accepted by ESA for implementation on the spacecraft.
(2) The reduced power output from the solar cell arrays due to faulty wiring detected after launch reduced the charging rate of the spacecraft batteries. As a consequence of the then imposed mission rules, use of the spacecraft transmitter was prohibited during solar eclipses. Because solar eclipse seasons at Mars regularly occur together with Earth occultation seasons, some complete occultation seasons were lost while others were effectively foreshortened by 50% or more.

Arriving at Mars a few years earlier than MEX, Mars Global Surveyor (MGS) produced a very comprehensive set of Mars radio science occultation data (Tyler et al., 2001; Tyler et al., "PDS SDP Data Set"). Comparing the two missions, the orbits and instrumentation are complimentary. MaRS transmissions at two downlink frequencies provide much stronger constraints on plasma distributions than do the X-band only transmissions of MGS. The near-circular, two-hour orbit of MGS, however, resulted in a much more uniform, and a significantly higher spatial sampling rate of the Mars atmosphere than with MEX. The orbit of MEX provides practically global coverage in occultation latitude, much better than was the case for MGS, where dayside occultations were essentially limited to the northern polar regions. The highly elliptical MEX orbit provides also periapsis passes (at 250 km altitude) that are significantly lower than those of MGS (at 400 km altitude), thereby increasing the sensitivity of the orbit to gravitational anomalies, improving observations of the ionopause, and providing close flybys of Phobos with the spacecraft near apoapsis.

In order to obtain the required frequency stability in the absence of a stable on-board frequency source (USO), MaRS operations, with the exception of BSR observations, were necessarily carried out with two-way tracking. In this configuration, the ground station transmits an uplink signal at $f_{up}=7.1$ GHz (4.2 cm), which is received by the spacecraft and immediately retransmitted to the ground simultaneously at two coherent downlink frequencies of $f_{S,down}=2.3$ GHz and $f_{X,down}=8.4$ GHz (13.1 cm and 3.6 cm), referred to as S-band and X-band, respectively.

The two downlink frequencies are constructed from the output of the received uplink signal in the exact constant transponder ratios $k_X=880/749$ and $k_S=240/749$,

$$f_{X,down} = k_X \cdot f_{up,received}$$
$$f_{S,down} = k_S \cdot f_{up,received} \quad (2.1)$$

The uplink frequency $f_{up,received}$ received by the spacecraft is the sum of the transmitted frequency f_{up} = 7100 MHz, the Doppler shift resulting from the relative motions of Earth based transmitter and the spacecraft $\frac{v_r}{c}f_{up}$, and a net phase advance imposed by the turbulent solar wind plasma along the ray path

$$f_{up,received} = f_{up} - \frac{v_r}{c}f_{up} + \Delta f_{SW} \quad (2.2)$$

If the uplink radio signal is received during an occultation, then there is an additional frequency shift caused by the bending of the radio ray path in the atmosphere/ionosphere. The transponder ratios k_X and k_S are constant, so the transmitted downlink frequencies $f_{X,transmitted}$ and $f_{S,transmitted}$ at X-band and S-band, respectively, have the constant ratio of 11/3 by design at the time of transmission:

$$\frac{f_{X,transmitted}}{f_{S,transmitted}} = \frac{k_X}{k_S} = \frac{880}{240} = \frac{11}{3} \quad (2.3)$$

The ground station observes the downlink signals which also have contributions from Doppler effects and plasma perturbations similar to those discussed for the uplink (2.2).

MaRS obtains information on the surface of Mars by directing radio transmissions from the MEX spacecraft toward selected areas of Mars' surface, and capturing the resulting carom signal at the same ground tracking stations employed for telemetry. These observations require considerable planning and effort to implement a unique spacecraft maneuver by which the center of the high-gain antenna (HGA) beam is slewed along the moving track calculated to direct the specularly reflected echo signal to Earth. Such BSR experiments are performed in the one-way radio mode. The scattered signals at X-band and S-band are received at a 70-m antenna of the NASA DSN.

3. Data recording and processing

Radio science data are recorded at the ground station antenna site. MaRS is supported by two antenna networks:

(1) The European System of Tracking Antennas (ESTRACK) with 35-m deep space antennas at New Norcia (NNO) in West-Australia, and Cebreros (CEB), near Madrid, Spain. The NNO antenna can transmit an X-band uplink and receive X-band and S-band downlinks simultaneously. The CEB antenna transmits and receives X-band. only.
(2) The NASA Deep Space Network (DSN) comprises antenna complexes at Goldstone (Complex 10) in the California Mojave desert; Robledo de Chavela (Complex 60) near Madrid, Spain; and Tidbinbilla (Complex 40), near Canberra, Australia. Each complex supports one 70-m and one or more 34-m High Efficiency (HEF) antennas. A 70 m antenna can be configured to receive downlinks at both X- and S-band, and at both right- and left-hand circular polarizations (RCP and LCP). The HEF antennas can receive X-band and S-band at one polarization (RCP only).

Table 3.1 gives an overview of the antenna parameters, system temperatures and noise levels.

Table 3.1
Radio Frequency System Parameters relevant for the MaRS Experiment

Spacecraft (transmit)		
Frequency Band	X-band	S-band
High Gain Antenna Diameter (m)	1.6	1.6
Antenna Gain (dBi)	39.6	28.0
Transmitter output power (watt)	65	5
Transmitter output power (dBm)	48.1	37.0

Ground Station (receive)				
	ESA New Norcia		**NASA DSN**	
Frequency Band (X/S)	X-band	S-band	X-band	S-band
Antenna Diameter (m)	35	35	70	70
Antenna Gain (dBi)	68.2	55.8	73.3	63.1
Eff. G/T @ 10° elev. (dB/K)	49.5	39	57.0	47.8

MEX observables, essentially received signal frequency and power, are recorded at the receiving ground station, and written to an electronic file which is delivered to the MaRS team. These 'raw' data originating from either DSN or ESTRACK complexes, also referred internally to as Level-1a data, have distinct formats and representations which are first converted to physical values (Level-1b data). The received, or 'antenna' frequency, is reconstructed and calibrated for the propagation delay in transiting Earth's troposphere and ionosphere. The received signal power is expressed in decibels relative to 1 mW (dBm). The noise level is computed from the system temperature and the bandwidth. The relative strength of the received signal power to this noise floor is expressed as the signal-to-noise ratio (SNR).

It is not the classical Doppler shift caused by the relative motion between the spacecraft HGA phase center and the ground station antenna phase center which is of interest, but rather the incremental Doppler shift caused by the perturbed spacecraft velocity in the asymmetric Martian gravity field or by the attracting forces of Phobos during flybys. Of interest are also additional frequency shifts caused by the bending of the radio ray paths in the Martian ionosphere and atmosphere. These frequency shifts are very small (fractions of Hertz; see Figs. 3.1–3.3) compared to an unperturbed classical Doppler shift (of the order of 28 kHz, one-way, for a relative radial velocity of 1 km/s at X-band). In order to extract these small frequency shifts for further investigation, a predicted sky-frequency (which does not consider contributions from the gravity field, Phobos or propagation through the Mars atmosphere/ionosphere) is calculated and subtracted from the received sky-frequency to obtain frequency residuals.

This prediction for the received frequency, called "The Predict" by the MaRS team, is computed by a complex force model that accounts for gravitational forces (planetary gravity field, all other planets as third body attractions) and non-gravitational forces (like solar radiation pressure), acting on the spacecraft based on the reconstructed spacecraft orbit. Also included in the calculation are the motion of Mars in its orbit, the motion and rotation of the Earth, solid Earth tides, plate tectonics, the relativistic Doppler effect and the finite light time between transmission and reception of radio signals. The important quantity from this calculation is Δv_r, the relative velocity component along the line-of-sight (LOS). The Doppler shifts for the uplink path at 7.1 GHz and the downlink paths at 8.4 GHz and 2.3 GHz are computed from the carrier frequencies by

$$\Delta f = -f_0 \frac{\Delta v_r}{c} \tag{3.1}$$

where f_0 is the relevant carrier frequency, Δv_r is the relative velocity component for the uplink or downlink path and c is the speed of light. The predicted received frequency is then

$$\begin{aligned} f_{pred} &= f_{down} - f_{down} \cdot \frac{\Delta v_{r,down}}{c} \\ &= k f_{up} - k f_{up} \frac{\Delta v_{r,up}}{c} - k\left(f_{up} - f_{up}\frac{\Delta v_{r,up}}{c}\right) \cdot \frac{\Delta v_{r,down}}{c} \\ &= k f_{up}\left(1 - \frac{\Delta v_{r,up}}{c}\right) - k f_{up}\frac{\Delta v_{r,down}}{c} + k f_{up}\frac{\Delta v_{r,up}}{c}\frac{\Delta v_{r,down}}{c} \\ &\approx k f_{up}\left(1 - \frac{\Delta v_{r,up}}{c} - \frac{\Delta v_{r,down}}{c} + \ldots\right) \end{aligned} \tag{3.2}$$

where $f_{up} = 7.1$ GHz is the uplink carrier frequency, and k is the transponder ratio, given by $k_X = \frac{880}{749}$ for the predicted received X-band frequency, and $k_S = \frac{240}{749}$ for the predicted received S-band frequency.

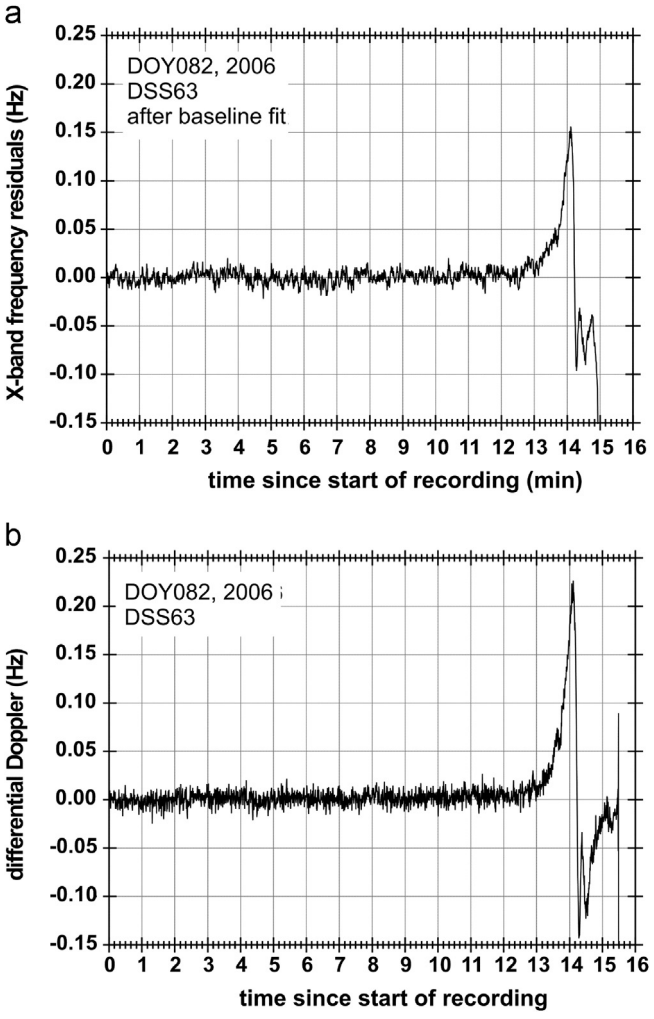

Fig. 3.1. Upper panel (a): Baseline corrected frequency residuals (received sky-frequency minus predicted sky-frequency) at X-band from the occultation entry on DOY 082, 2006, recorded at the DSN 70-m antenna DSS 63 near Madrid, Spain. A baseline fit of first order computed from the first ten minutes was subtracted from the "raw" residuals to correct for a bias (typically 10 MHz to 50 MHz) arising from contributions not considered in the prediction or orbit errors. The first deviation from the zero line at 12.5 minutes is the start of the sensible ionosphere. The peaks at 14 minutes and 14.2 minutes are the ionospheric main layer and secondary layer, respectively. The frequency residuals drop to typically −10 Hz in the neutral atmosphere before going into geometrical occultation by the Mars limb. lower panel (b): differential Doppler computed from the simultaneously received X-band and S-band frequencies according to (3.6). It is assumed that the differential Doppler contains only contributions from the radio propagation through plasmas.

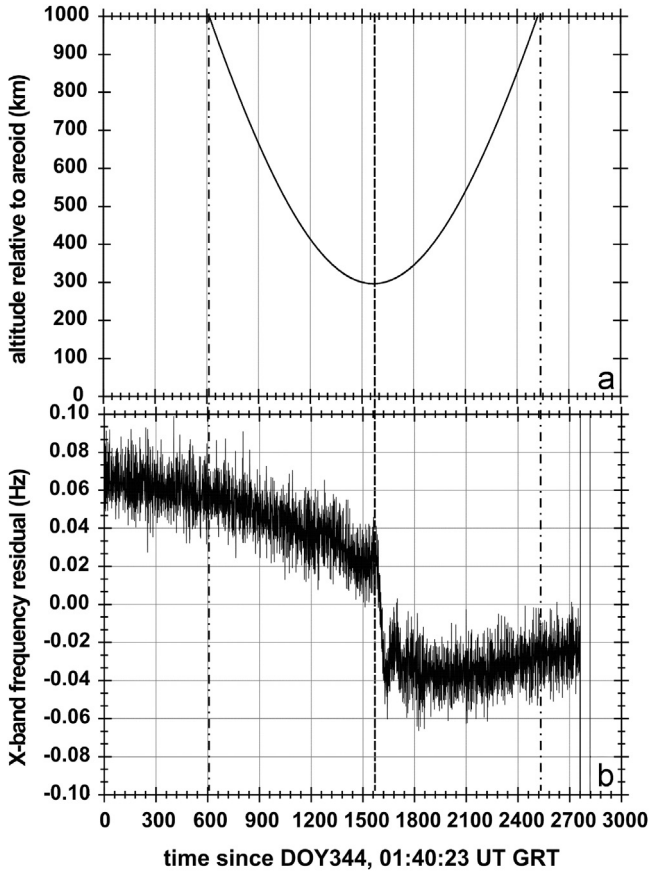

Fig. 3.2. Gravity pass during orbit 1044 over Olympus Mons on DOY 344, 2004. Upper panel (a): MEX altitude below 1000 km. MEX passed through pericenter at an altitude of 280 km (dashed line) over the caldera. Lower panel (b): Frequency residuals at X-band caused by the Martian gravity field beyond degree and order 50. Relevant for crustal studies are altitudes below 1000 km (time between the two dashed-dotted lines). A clear signal from the massive volcano body is visible at the time of pericenter passage.

If $\Delta\nu_{r,up} = \Delta\nu_{r,down} = \Delta\nu_r$ (and they are to a good approximation), then the Doppler shift relation may be written as

$$f_{pred} = kf_{up}\left(1 - 2\frac{\Delta\nu_r}{c}\right) \tag{3.3}$$

Frequency residuals are computed for each received frequency from the difference between the received sky-frequency and the predicted received frequency:

$$f_{res} = f_{sky} - f_{pred} \tag{3.4}$$

The frequency residuals contain all frequency shifts not considered in the prediction. These arise either generally or during certain mission events:

(1) General: orbit errors from gravitational and non-gravitational forces not considered in the prediction, mostly characterized by a constant, which is removed by a baseline fit (Fig. 3.1a).
(2) Occultations: bending of the ray path in the ionosphere and neutral atmosphere starting about two minutes before the geometrical occultation (Fig. 3.1b).
(3) Target gravity passes: contributions from the planetary gravity field beyond degree and order 50 and below 1000 km altitude (Fig. 3.2).
(4) Phobos flybys: the frequency shift caused by the gravitational attraction of Phobos (mass) acting on the spacecraft and perturbing the orbit (Fig. 3.3).

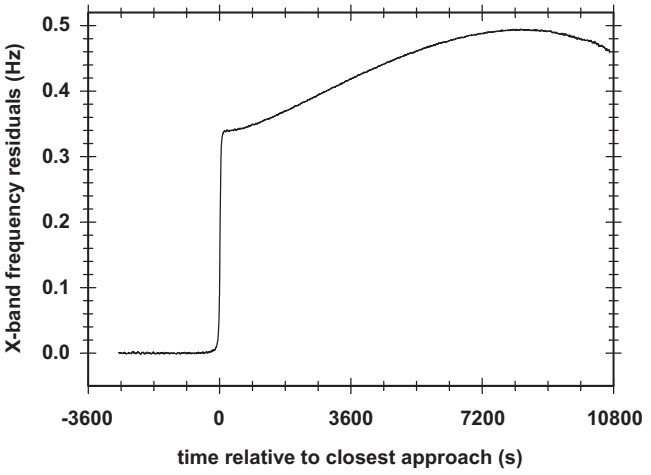

Fig. 3.3. Calibrated and filtered ($\Delta t = 5$ s) frequency residuals at X-band from the MEX flyby at Phobos on DOY 062, 2010, at a distance of 72 km (Pätzold et al., 2014). The attracting force of Phobos perturbed the velocity and orbit of MEX, clearly visible as a perturbed Doppler shift. Considering the flyby geometry, the frequency shift at closest approach is a measure of the mass of Phobos.

The contributions from the propagation of the radio signal through the terrestrial troposphere and ionosphere are corrected by models (see online material in Pätzold et al., 2011) using real-time meteorological measurements (temperature, pressure, humidity, wind) from the ground station antenna site and GPS observations, respectively.

MaRS uses the two phase-coherent downlink frequencies at X-band and S-band. The frequency ratio of these downlinks is

$$\frac{f_{X,down}}{f_{S,down}} = \frac{11}{3} \tag{3.5}$$

The so-called differential Doppler δf , for which Doppler shifts from motion or residual motion have been eliminated,.is computed from both received frequencies

$$\delta f = f_{S,received} - \frac{3}{11} f_{X,received} \tag{3.6}$$

Usually, the frequency residuals (3.4) at X-band are the starting point for further data analysis of gravity observations, flybys or the sounding of the neutral atmosphere. The differential Doppler, which contains only the frequency shifts from the propagation through plasmas, is used for the sounding of planetary ionospheres and the solar corona. The differential Doppler is essentially equivalent to a one-way S-band downlink (Pätzold et al., 2012).

The Level-1b data are processed in such a way that the Level-2 data present a standard format, independent of the recording mode (closed-loop or open-loop) or the tracking antenna (ESTRACK or DSN). The Level-2 data file contains time stamps of various formats, the reconstructed calibrated sky-frequency, the predicted sky-frequency, the frequency residuals, the differential Doppler, the received signal power and other ancillary (time-dependent) data for completeness. The Level-2 data product is ready to use and serves as the starting input for gravity studies, flybys, occultations and solar corona studies. The occultation Level-2 data need further processing in order to derive profiles of

temperature, pressure, number density and electron density (see chapter 4). The BSR data, due to their inherently different nature and complexity, are formatted differently (see Chapter 5). The Level-2 data are archived with the Planetary Science Archive at ESA (PSA) and the Planetary Data System (PDS) at NASA.[1] At the time of this publication, two-thirds of the MaRS data base is available for the interested user.

4. Occultations

4.1. Principles, method and coverage

4.1.1. From frequency residuals to the atmospheric refractivity

The atmosphere and ionosphere are sensed by their effects on radio carrier waves traveling between the MEX spacecraft and Earth during periods of Earth occultation, i.e., those intervals when the spacecraft moves behind the atmosphere in the plane-of-sky as seen from the Earth. These events occur during "seasons" which last from a few weeks up to many months depending on the orientation of the MEX orbit plane with respect to the Earth-Mars line-of-sight. Table 4.1 lists the number of daytime ($>50^\circ$ as the minimal feasible solar zenith angle (SZA)), nighttime ($SZA > 95^\circ$) and near-terminator ($85^\circ < SZA < 95^\circ$) occultations for the MEX occultation seasons from 2004 to 2013.

The radio subsystem of the spacecraft is configured as X-band uplink and coherent dual-frequency downlink. The recordings of the downlinks at X-band and S-band start about twenty minutes before the geometrical occultation of the spacecraft by the planetary limb. Fig. 3.1 shows an example of frequency residuals at both X-band and S-band observed at an Earth tracking station. The actual sounding of the ionosphere and the neutral atmosphere by the radio signals occurs during the last few minutes of the recording. The initial (positive) frequency shift in Fig. 3.1, caused by the radially outward bending of the radio ray path in the ionosphere, reaches values of up to one Hertz at X-band, depending on the electron density within the main ionospheric layer. When the radio signal propagates through the neutral atmosphere and the ray path bends radially inward, the frequency shift becomes negative and may reach -10 Hz near the time of signal extinction at the planetary surface.

The frequency recordings contain biases caused by contributions not considered in the calculation for the predicted sky-frequency that are unique to each occultation. These biases can be constant or show a slight trend and are corrected by a polynominal baseline fit of first or second order. The corrected X-band frequency residuals are used to compute the bending angle for the neutral atmosphere below 70 km altitude. The differential Doppler (3.6), computed from both downlink frequencies, is used to derive the bending angle for the ionosphere. The differential Doppler eliminates all frequency shifts that are linear in frequency (e.g., residual orbit errors or vibrational motion of the spacecraft body) such that only contributions from radio propagation through plasma remain. This is applied at heights from the top of the ionosphere down to 70 km. If the S-band downlink is not available, the X-band residual frequency profile can still be used, but potential Doppler contributions not connected to plasma propagation are still contained in the frequency residuals and could be incorrectly translated into electron density. These residual Doppler motions may then appear as perturbations within the electron density profile.

[1] PSA: http://www.rssd.esa.int/index.php?project= PSA; PDS: https://pds.nasa.gov/.

Table 4.1
Occultation seasons: number of profile

				Daytime $50^\circ < SZA < 85^\circ$						Terminator $85^\circ < SZA < 95^\circ$						Nighttime $SZA > 95^\circ$					
				X-Band		diff. Dop. ionosphere		neutral atmosphere		X-Band		diff. Dop. ionosphere		neutral atmosphere		X-Band		diff. Dop. ionosphere		neutral atmosphere	
OCC	Start	End	Ls (°)	NNO CEB	DSN	NNO CEB	DSN	NNO CEB	DSN	NNO CEB	DSN	NNO CEB	DSN	NNO CEB	DSN	NNO CEB	DSN	NNO CEB	DSN	NNO CEB	DSN
OCC 1	2004-04-02	2004-08-14	13.6–73.8	33	37	24	34	33	37	3	0	0	0	3	0	3	3	1	0	2	0
OCC 2	2004-12-08	2005-01-04	126.3–139.4	5	0	5	0	5	0	8	3	8	3	8	3	11	6	10	6	11	6
OCC 3	2005-07-19	2006-04-24	253.2–43.5	115	97	90	86	115	97	10	5	7	5	10	5	42	16	32	15	42	16
OCC 7	2007-04-25	2007-06-03	225.9–250.1	3	10	3	9	3	10	0	0	0	0	0	0	9	6	9	6	9	6
OCC 8	2008-06-21	2008-09-23	88.3–131.6	17	21	17	20	17	21	5	4	6	4	0	4	8	1	8	1	3	1
OCC 9	2009-01-29	2009-03-08	200.0–222.9	6	2	6	1	0	2	0	5	0	5	0	5	0	0	0	0	0	0
OCC 10	2009-09-20	2009-11-12	341.6–8.6	20	5	20	5	20	5	8	2	6	2	8	2	12	0	11	0	12	0
OCC 11	2010-03-03	2010-06-27	59.2–110.3	19	0	19	0	19	0	11	9	11	9	11	9	0	0	0	0	0	0
OCC 12	2011-06-11	2011-08-07	308.9–341.0	20	16	19	16	20	16	11	7	11	7	11	7	5	2	5	2	5	2
OCC 14	2012-10-16	2012-12-12	189.7–223.9	18	0	15	0	18	0	7	0	7	0	7	0	0	0	0	0	0	0

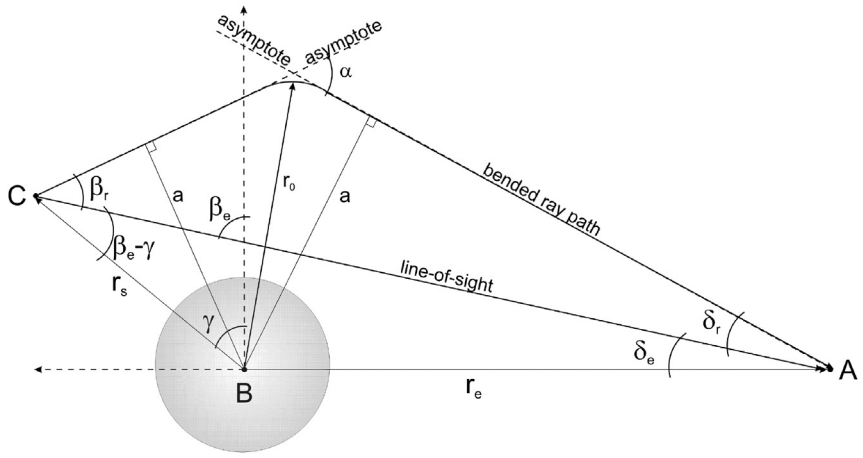

Fig. 4.1. Occultation geometry: The corners of the triangle A, B, C are the positions of Earth, Mars and the spacecraft, respectively, in an 2-D coordinate system centered at B with the *z*-axis pointing from B to A and the *r*-axis perpendicular to the *z*-axis. A radio signal transmitted by the spacecraft at C and received at A would travel along the line-of-sight if no atmosphere around the planet at B is present. If the planet has an atmosphere, then the radio signal travels along the true bent ray path. An extra frequency shift occurs relative to the frequency shift along the line-of-sight (straight line Doppler). The bending angle α (the angle between the two ray asymptotes) is computed from the extra frequency shift and the occultation geometry. r_0 is the closest approach of the bended ray path to the planet. The geometry angles need to be computed from the known ephemerides of Mars and Earth and the spacecraft orbit file for each time step of the observation.

The frequency residuals as shown in Fig. 3.1 and the state vectors of the Earth and the spacecraft are the starting points for the derivation of a profile of atmospheric bending angles.

Fig. 4.1 shows the occultation geometry with the triangle *ABC*, where *A* is the position of the Earth, *B* is the position of Mars and *C* is the position of the spacecraft. The (exaggerated) refracted ray path from C to A is assumed to lie in a plane defined by the vectors between A, B and C due to the spherical symmetry of the refracting atmosphere/ionosphere. The two ray asymptotes to Earth and spacecraft have impact parameters denoted by *a*. The angle between the two ray asymptotes is the bending (refraction) angle α. The direct line-of-sight distance between *A* and *C* is the geometric separation of spacecraft and ground station, the path the radio signals would travel if there were no atmosphere. The frequency residuals in Fig. 3.1 would be zero if the radio signal would travel along the straight line from C to A.

Propagation through the atmosphere and ionosphere, however, requires that the ray path bends. The goal is to determine the angles between the two ray asymptotes, β_r and δ_r , which define the bending angle α:

$$\alpha = \beta_r + \delta_r \tag{4.1.1}$$

where β_r and δ_r are the angles between the line of sight between A and C and the asymptotes to the spacecraft and the ground station, respectively (Fig. 4.1). The residual frequency shift Δf of the signal due to the bending of the ray path in the atmosphere is determined by

$$\begin{aligned}\Delta f = &\frac{f_0}{c}[v_{r,Earth}\ \sin(\delta_e+\delta_r)+v_{z,Earth}\ \cos(\delta_e+\delta_r)\\ &-v_{r,s/c}\ \sin(\beta_e+\beta_r)-v_{z,s/c}\ \cos(\beta_e+\beta_r)]\\ &-\frac{f_0}{c}[v_{r,Earth}\ \sin(\delta_e)+v_{z,Earth}\ \cos(\delta_e)\\ &-v_{r,s/c}\ \sin(\beta_e)-v_{z,s/c}\ \cos(\beta_e)]\end{aligned} \tag{4.1.2}$$

where the first bracket is the frequency shift of the signal taking the true bended ray path and the second bracket is the frequency shift of the signal along the line-of-sight (straight line Doppler), f_0 and *c* are the carrier frequency at X-band or S-band and the speed of light, respectively, $v_{r,Earth,}$ $v_{z,Earth,}$ and $v_{r,s/c,}$ $v_{z,s/c}$ are the velocity components of the Earth and the spacecraft, respectively, in the coordinate system as shown in Fig. 4.1, where the unit vector ***z*** is defined along the distance from B to A, and ***r*** is the unit vector perpendicular to ***z*** in the occultation plane.

The velocity components are known from the ephemerides of the Earth, Mars and the spacecraft at the time of observation. The ray impact parameter *a*, the distance between the ray asymptotes to the center of the planet is (Fig. 4.1)

$$a = r_e\ \sin(\delta_e+\delta_r)$$

and

$$a = r_s\ \sin(\beta_r+\beta_e-\gamma) \tag{4.1.3}$$

where r_e is the distance between A and B, δ_e is the angle between re and the line-of-sight and δr is the angle between the line-of-sight and the true ray asymptote starting at A, r_s is the distance between the center of the planet and the spacecraft, β_r is the angle between the line-of-sight and the ray asymptote and β_e-γ is the angle between the line-of-sight and the distance between B and C. Again r_e, r_s, δ_e and β_e are known from the ephemerides at the time of the observation. The angles β_r and δ_r are determined iteratively from the residual frequency shift using the successful standard method described by Gunnar Fjeldbo at Stanford University, first described in his PhD thesis 50 years ago (Fjeldbo, 1964; Fjeldbo and Eshleman, 1965) and first applied to the Mariner-4 flyby at Mars in 1965 (Kliore et al., 1965) and used for all other planetary radio occultation experiments thereafter.

It is important to note that the method for extracting the bending angles and ray asymptotes described by Fjeldbo et al. (1971) is valid for one-way experiments only. The approach must be modified for two-way experiments. In this case, the initial (X-band) signal is transmitted from a hydrogen maser on Earth and received on the spacecraft. The signal is transformed into two coherent signals that are immediately transmitted to Earth. Jenkins et al. (1994) provide a good overview of the two-way approach.

The next important step is the derivation of refractivity $\mu(r)=(n(r)-1)\cdot 10^6$ from knowledge of the bending angle $\alpha(a)$ where $n(r)$ is the refractive index as a function of radius relative to the centre of the planet. These two parameters are connected via an Abel transform

$$\alpha(a) = -2a\int_{r=r_0}^{\infty}\frac{1}{n}\frac{\partial n}{\partial r}\frac{\partial r}{\sqrt{(nr)^2-a^2}} \tag{4.1.4}$$

with r_0 the ray periapsis, the closest approach of the ray path from the center of the planet, related to the ray asymptote by

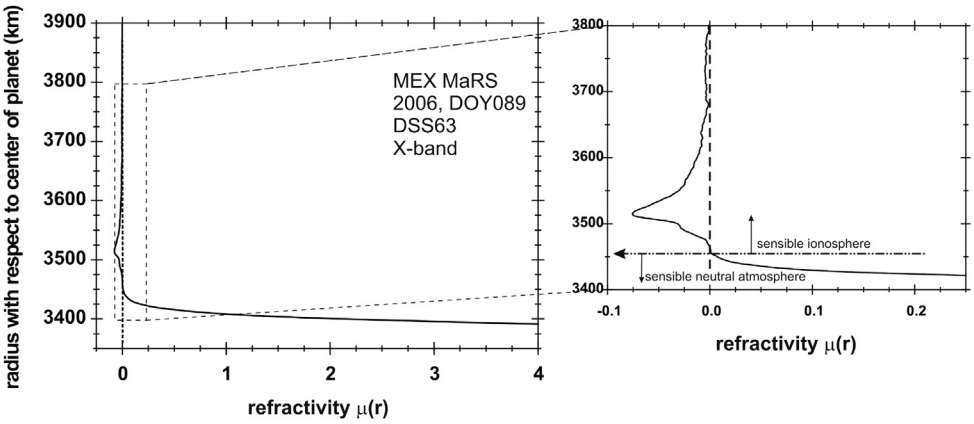

Fig. 4.2. Refractivity profile observed during the Earth occultation on DOY082, 2006, at the 70-m antenna DSS-63 near Madrid as a function of radius with respect to the center of the planet from the surface at 3389 km to a radius of 5900 km well above the ionopause (only shown here up to 3900 km). The ionosphere is reflected in the negative refractivity above 3460 km (seen best in the expanded inset). The refractivity changes sign at about 3450 km (about 60 km above the surface). The propagation of the radio wave is dominated by the ionosphere and the neutral atmosphere above and below that radius, respectively.

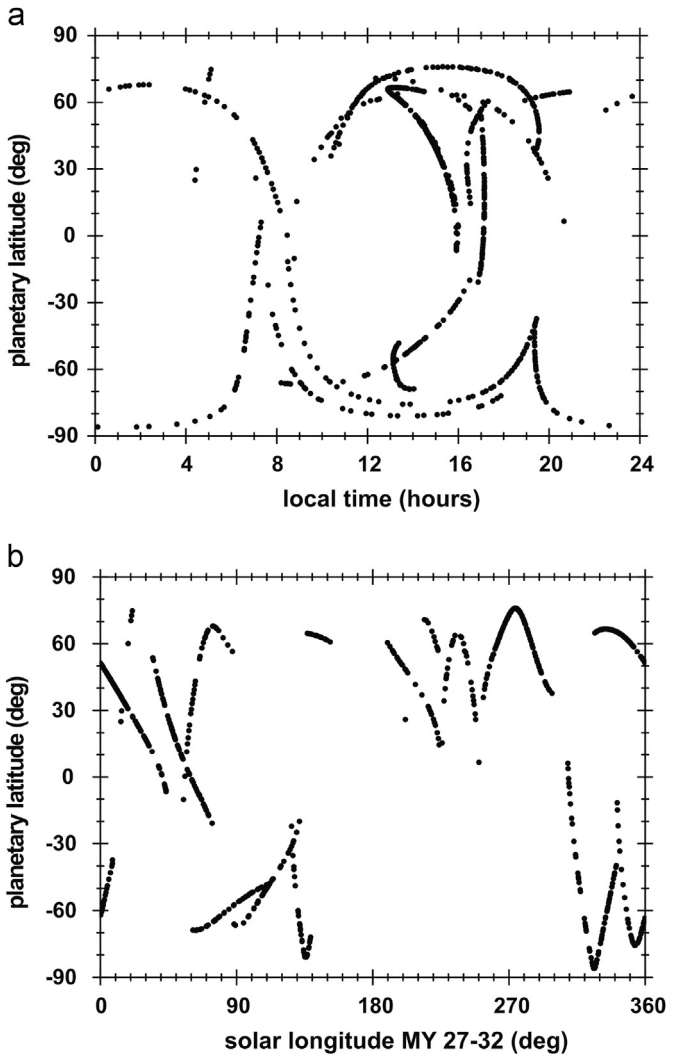

Fig. 4.3. Distribution of MaRS measurements in the neutral atmosphere from April 2004 (early MY 27) through July 2014 (early MY 32). Left panel: The MEX orbit yields observations at unique combinations of local time and latitude, including broad coverage of the tropics in late afternoon. Right panel: Coverage in latitude and Mars season See Figures 2 and 3 in Tellmann et al. (2013) for alternate displays of the coverage distribution.

Bouger's Law (see Fjeldbo et al., 1971):

$$r_0 = \frac{a}{n(r_0)} \tag{4.1.5}$$

Using (4.1.5), the inverse transform of equation (4.1.4) may be written as

$$\ln(n(r_{01})) = -\frac{1}{\pi}\int_{a=a_1}^{\infty} \frac{\alpha(a)}{\sqrt{a^2 - a_1^2}} da \tag{4.1.6}$$

where a_1 is the asymptotic impact parameter for a ray with closest approach r_{01} (see Fjeldbo et al. (1971) for details).

We have now a table of refractivity as well as the associated asymptotic impact parameter a, the bending angle α, and the ray periapsis r_0, for each time step, effectively yielding a vertical altitude profile of refractivity (Fig. 4.2).

The refractivity is proportional to the electron density profile $N_e(r)$ in the ionosphere

$$\mu(r) = -\frac{40.31 \cdot 10^6 m^3 s^{-2}}{f_0^2} N_e(r) \tag{4.1.7}$$

and to the neutral number density $N(r)$ in the neutral atmosphere

$$\mu(r) = \kappa \cdot N(r) \tag{4.1.8}$$

where $\kappa = 1.804 \cdot 10^{-29}\ \mathrm{m}^3$ (Hinson et al., 1999) is the refractive volume which is computed from the composition of the neutral atmosphere (95.32% CO_2, 2.7% N_2, 1.6% Ar taken from Owen, 1992). The neutral number profile is crucially dependent on the correct knowledge of the atmospheric composition. The derivation of the atmospheric profiles starts therefore with the neutral number density profile $N(r)$ from (4.1.8) and the electron density profile $N_e(r)$ from (4.1.7).

The approach by Fjeldbo et al. (1971) assumes spherical symmetry around the center of the planet. Whenever the planet has a certain oblateness, such as with Mars, Jupiter or Saturn, this approach must be modified by assuming local symmetry around a local center of gravity given by the gravitational acceleration (Hubbard et al, 1975; Eshleman, 1975). A thorough analysis of the uncertainties in radio occultation profiles can be found in Lipa & Tyler (1979). Atmospheric spherical symmetry is broken at or near the terminator. Derived vertical profiles for solar zenith angles between 85° and 95° must therefore considered with caution. The influence of the effect of departures from spherical symmetry in the Martian atmosphere was investigated by Ahmad and Tyler

(1999). They demonstrated that the impact of this effect strongly depends on the geometry and season of the measurement. They estimated the fractional errors to be as large as a few percent above 20 km in the worst case, decreasing in magnitude closer to the surface.

The derived atmospheric profiles of neutral number density $N(r)$, temperature $T(r)$ and pressure $p(r)$ and electron density $N_e(r)$ are considered vertical although the electron density profiles are somewhat slanted over a horizontal distance of 400 km for altitudes between 100 km and 350 km.

4.1.2. Observational coverage

The MEX occultation measurements have yielded more than 700 profiles of the neutral atmosphere spanning 5 Mars years (MY), across a range of solar longitudes from $L_s = 14°$ of MY 27 through $L_s = 90°$ of MY 32. The measurements are widely distributed in latitude, local time, and season, as shown in Fig. 4.3, but the coverage is not uniform. For example, few profiles are available in the northern hemisphere during the northern summer season (Ls = 90–180°) and none are available in the southern hemisphere during southern spring (Ls = 180–270°). These gaps arise from the absence of observations at occultation egress. In addition, measurements in the tropics are restricted to local times near the morning and evening terminators.

The spacecraft orbit determines the coverage of the occultation measurements. The MEX orbit is highly elliptical with an inclination of 86° relative to the equator and a radius at periapsis of less than 3700 km (Chicarro et al., 2004). The orbital plane drifts steadily with respect to local time on Mars, completing the cycle in about 1 Mars year, with several notable consequences. First, the occultations are restricted to discrete 'seasons', which typically last 2–4 months and recur roughly twice per Mars year when the angle between the Mars-Earth line and the MEX orbital plane is sufficiently small. In the intervening periods, the orbital plane is more nearly perpendicular to the Mars-Earth line so that occultations are absent. Second, because of the limitation to occultation entry, the radio occultation measurements alternate between the northern and southern hemispheres in successive seasons. Third, and most importantly, MEX can sound the tropics at the morning and evening terminators – at local times near both sunrise and sunset. In contrast, low-latitude radio occultation measurements by both Mars Global Surveyor (MGS) and Mars Reconnaissance Orbiter (MRO) are limited to local times a few hours before sunrise, owing to the phasing of their sun-synchronous polar orbits. (These three characteristics of the MEX radio occultation coverage are also illustrated in Fig. 4.5, below.)

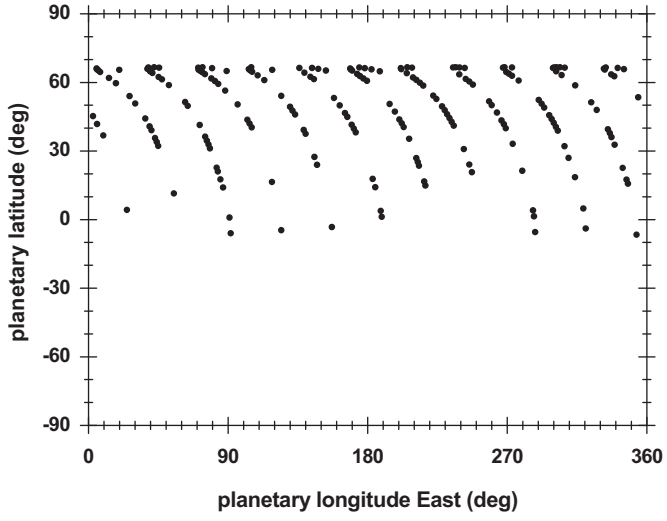

Fig. 4.4. Spatial distribution of radio occultation measurements from November 2005 (late MY 27) through April 2006 (early MY 28). This subset of observations covered latitudes from 67°N to 7°S at 11 evenly spaced longitudes.

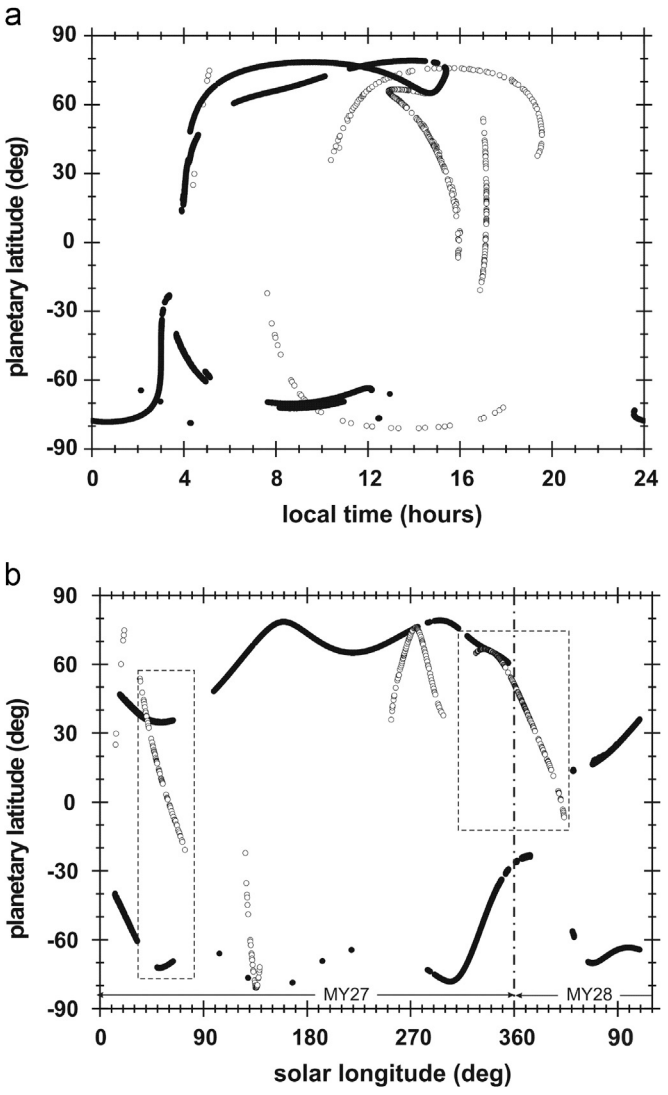

Fig. 4.5. Coverage of radio occultation measurements by MEX (open circles) and MGS (filled circles) from April 2004 through September 2006. The boxes in panel (b) enclose concurrent observations by MEX and MGS that were used to study Kelvin waves (left box in panel b) and for validation and to characterize the polar vortex (right box in panel b).

The longitude distribution of the measurements is determined primarily by the rotation of Mars and the period of the MEX orbit. For example, Fig. 4.4 shows the spatial coverage over a 6-month span of observations that began near 65°N in November 2005, at Ls=327° of MY 27. The latitude first drifted slightly northward to 67°N and then moved steadily southward, reaching 7°S at Ls=44° of MY 28. MEX completed 11 orbits every 3 solar days at the time of these observations, yielding radio occultation measurements with a uniform separation in longitude of approximately 33°.

Concurrent MEX and MGS occultation measurements began in April 2004, the start of the MEX observations, and continued through September 2006, the end of the MGS observations. Fig. 4.5 compares the radio occultation coverage during this interval, which extends from Ls=0° of MY 27 through Ls=120° of MY 28. The measurements by the two spacecraft are highly complementary. For example, MEX acquired numerous afternoon observations equatorward of 50° – yielding the first definitive measurements of the depth of the Martian convective boundary

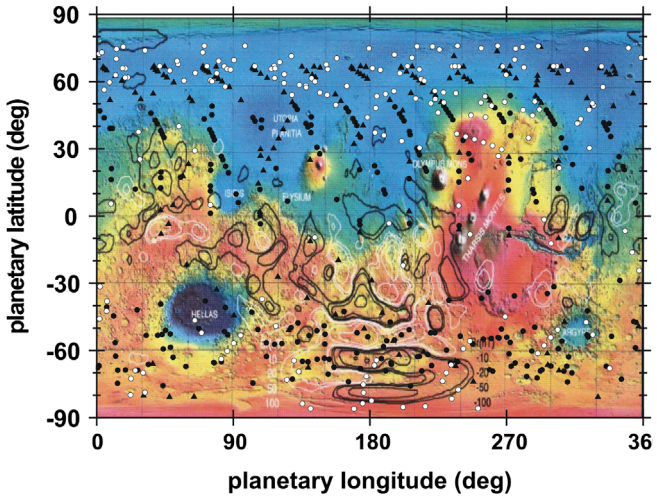

Fig. 4.6. Footprints of the ionospheric electron density profiles superimposed on a map of crustal magnetization (Connerney et al., 2001). The magnetic field is strongest in the southern hemisphere at longitudes of 120–240°E, whereas the occultations are more numerous in the north. Most of these measurements coincide with periods of decreasing and low solar activity, beginning in the declining phase of solar cycle 23 (open circles) in 2004-2008, continuing through the unusually long solar minimum in 2008-2009 (filled circles) and the rising phase of solar activity starting with the new solar cycle 24 (triangles).

layer (CBL) (Hinson et al., 2008b) – while the afternoon coverage by MGS is restricted to latitudes poleward of 60°. Conversely, MGS provided near-continuous coverage at mid-to-high northern latitudes throughout summer, autumn, and winter of MY 27 (Ls=90–360°), which has been used to investigate the characteristics and seasonal evolution of short-period baroclinic waves and their influence on regional dust storms in the topographic basins of the northern hemisphere (Hinson and Wang, 2010; Hinson et al., 2012). On one occasion – Ls=35–70° of MY 27 – the two spacecraft sounded a combination of latitudes and local times that enabled a unique investigation of both diurnal and semidiurnal Kelvin waves (Hinson et al., 2008a).

Fig. 4.6 shows the footprints of the ionospheric electron density profiles superimposed on a map of crustal magnetization (Connerney et al., 2001). The magnetic field is strongest in the southern hemisphere at longitudes of 120–240°E, whereas the occultations are more numerous in the north. Most of these occultation measurements coincide with periods of declining and low solar activity, beginning in the late phase of solar cycle 23 in 2004–2008 and continuing through the unusually long solar minimum in 2008–2009. Less numerous occultations have been observed in the early phase of solar cycle 24 with increasing solar activity and during maximum solar activity from 2012 to 2014.

4.2. Radio sounding of the neutral atmosphere

4.2.1. Methodology

The conventional two-way retrieval algorithm is used to derive atmospheric profiles from the MEX radio occultation data (Hinson et al., 2008a; Tellmann et al., 2013). The initial steps of analysis make use of the Abel transform, which leads directly to a profile of refractive index $\mu(r)$ versus planetocentric radius r, as discussed in Section 4.1.1. We convert $\mu(r)$ to a profile of neutral number density $N(r)$ by using established values for the mixing ratios and refractive properties of the primary constituents of the lower atmosphere (cf. Hinson et al., 1999). The resulting profile extends over the radial range $r_a < r < r_b$, where r_a is typically ~1 km above the surface and r_b is determined by the data quality. Profiles of pressure $p(r)$ and temperature $T(r)$ are derived from $N(r)$ by assuming hydrostatic balance, integrating vertically, and applying the ideal gas law. In a well-mixed atmosphere, it is

$$T(r) = \frac{N_b T_b}{N(r)} + \frac{\overline{m}}{N(r)k}\int_r^{r_b} N(r')\, g(r')dr' \qquad (4.2.1)$$

where $\overline{m}$ is the average molecular mass, k is the Boltzmann constant, and g is the acceleration of gravity. Integration extends to radius r_b where the density N_b is known but the temperature T_b must be provided as a boundary condition.

The radio occultation retrieval algorithm calculates the planetocentric radius r (the proximate distance of the ray path r_0), east longitude λ, and latitude ϕ associated with each discrete sample of N, T and p (e.g., Hinson et al., 1999). The uncertainty in position is less than 100 m, commensurate with the accuracy of the MEX orbit reconstructions (e.g., Rosenblatt et al., 2008). We then use a well-established model for the gravity field of Mars (Konopliv et al., 2006a, 2006b) to compute the geopotential height z at the location of each sample in the retrieved profile. This step also yields a standard vertical coordinate that serves as the reference for Martian topography (e.g., Smith et al., 2001a, 2001b). The pressure at $z=0$ is typically about 500 Pa.

Two factors determine the vertical resolution of the MEX profiles considered here. First, the retrieval algorithm relies on standard formulas of geometrical optics (e.g., Fjeldbo et al., 1971; Karayel and Hinson, 1997), which constrains the vertical resolution of the retrieved profiles to the characteristic Fresnel scale of diffraction – typically of the order of less than 1 km. Second, the uplink and downlink signals follow different paths through the atmosphere of Mars which is typically in the order of the Fresnel scale, and the measurements cannot resolve structure on spatial scales smaller than their separation. The net result is a vertical resolution in the order of the Fresnel scale of less than 1 km for radio occultation measurements with MEX.

The effective length of the propagation path through the Martian atmosphere is about $L_{eff} \approx \sqrt{2\pi r_0 H}$, where H is the neutral scale height and r_0 is the radius at the point of closest approach to Mars. The horizontal resolution of the radio occultation profiles is therefore $L_{eff} \approx 400$ km along the line of sight from spacecraft to Earth (for comparison, 1° of latitude is 59 km).

Each observation requires a baseline at altitudes exceeding roughly 300 km, where the effects of the neutral atmosphere and ionosphere are usually negligible. This baseline provides an intrinsic reference for measuring the changes in signal frequency associated with the atmosphere of Mars, enabling accurate absolute calibration of the retrieved profile. In addition, information extracted from the baseline is used for error analysis, as described below.

Fig. 4.7 shows a representative occultation profile, illustrating the quality of the MEX measurements. The results are displayed for three quantities: temperature T, potential temperature θ, and static stability S, where

$$\theta \equiv T\left(\frac{p_0}{p}\right)^{R/c_p} \qquad (4.2.2)$$

and

$$S \equiv \frac{dT}{dz} + \frac{g}{c_p} \qquad (4.2.3)$$

The reference pressure p_0 is set to 610 Pa in order to be consistent with previous publications (e.g. Smith, 2004; Hinson et al., 2008b). The exponent in (4.2.2), the ratio of the gas constant to the specific heat at constant pressure, is $R/c_p \approx 0.25$ under the conditions considered here (Hinson et al., 2008b). The ratio $g/c_p \approx 5\ \mathrm{K\ km^{-1}}$ is the adiabatic lapse rate. Each quantity – T, θ, or S – illustrates different aspects of the vertical structure. For example, the derivative dT/dz in (4.2.3) accentuates the modulation produced by small-scale atmospheric waves.

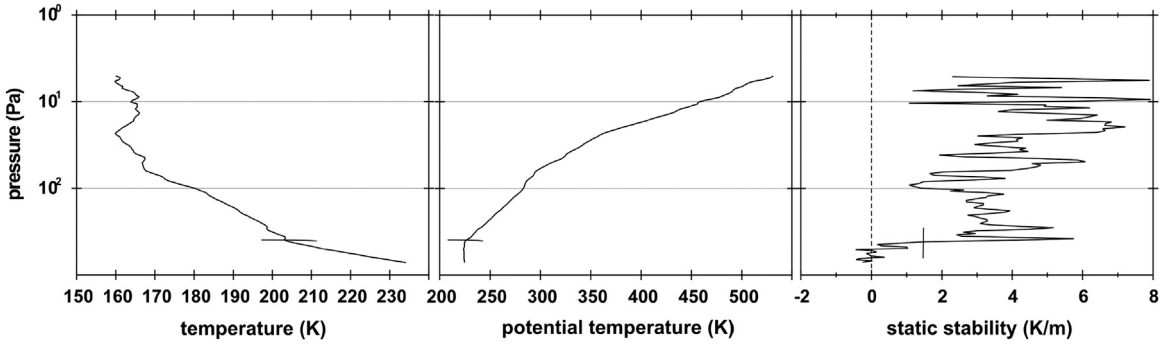

Fig. 4.7. Representative profiles of (left panel) temperature T, (center panel) potential temperature θ, and (right panel) static stability S retrieved from MaRS measurements on 23 March 2006. The location is 183°E, 18°N, in western Amazonis Planitia. The local time is 15.7 h. The season is early spring, Ls=29.3° of MY 28. The top of the CBL is marked by a horizontal line for T and θ and by a vertical line for S. The base of each profile is about 1 km above the ground.

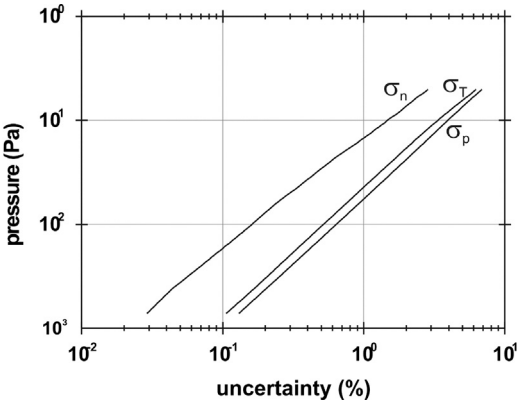

Fig. 4.8. The 1-sigma uncertainties in number density (σ_n), temperature (σ_T), and pressure (σ_p) for the profile in Fig. 4.7.

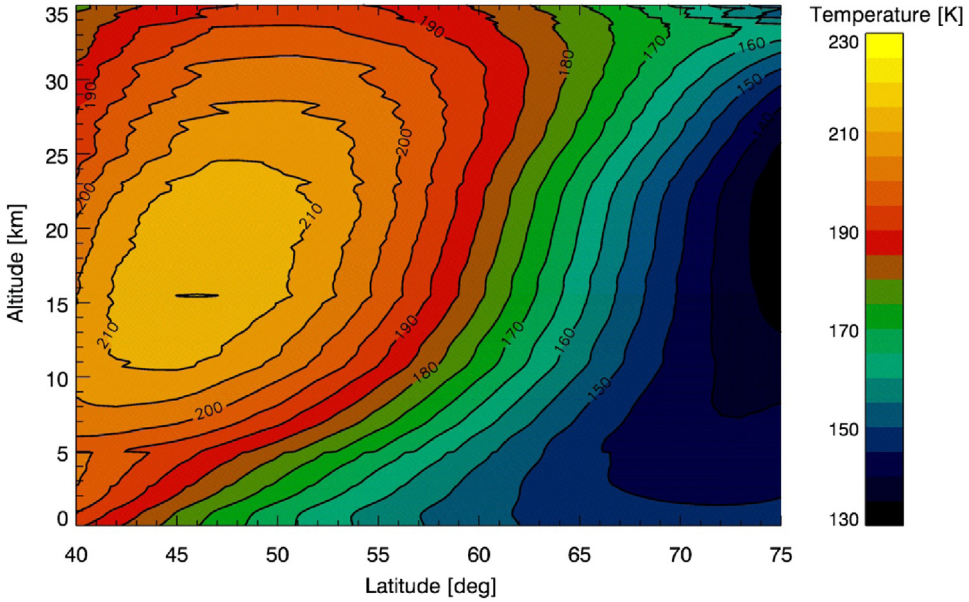

Fig. 4.9. Temperature structure around northern winter solstice (Ls ≈ 253°–274°, MY 27). The measurements started in the mid-latitude range (45° N, local time: 10:30 h) and ended in the high latitude range (70° N, local time: 15:00 h). 41 measurements were used for this investigation. Figure taken from Tellmann et al., (2013).

Fig. 4.7 shows results from measurements of the tropics in western Amazonis Planitia at a local time of 15.7 h during early spring of MY 28. The profile covers a pressure range of 5–720 Pa, corresponding to an altitude interval of 46 km. The temperature lapse rate is adiabatic and θ is nearly constant at pressures greater than 400 Pa, revealing the presence of a well-mixed convective boundary layer (CBL), as expected under these conditions. The depth of the CBL – 7.2 km in this example – can be accurately determined from the sharp transition to stable stratification at its upper boundary (the static stability S changes from < 1 K km^{-1} to > 4 K km^{-1} over a vertical range of $\approx$ 800 m). In addition, the overlying atmosphere is modulated by vertically propagating

gravity waves, which produce subtle but regular temperature oscillations with a dominant vertical wavelength of 3-4 km.

The accuracy of the radio occultation measurements varies strongly with the local pressure, as shown in Fig. 4.8, the estimated one-sigma uncertainties in the profile of Fig. 4.7. The uncertainty in number density σ_n is a consequence of noise inherent in the basic frequency measurements. This includes impulsive fluctuations, which arise from thermal noise, as well as gradual variations, such as those caused by irregularities in the terrestrial ionosphere or by sloshing of fuel on the spacecraft. The properties of the noise are first characterized by a statistical analysis of data from the baseline interval. The results are then propagated through the radio occultation retrieval algorithm. As an example, Fig. 4.8 shows the profile of σ_n derived from the measurements in Fig. 4.7. In this case σ_n decreases from approximately 3% at the top of the profile, where p is 5 Pa, to 0.03% at the base of the profile, where p is 720 Pa.

The retrievals of T and p are limited not only by the noise in the frequency measurements, but also by the uncertainty in T_b, which is the predominant error source at pressures less than about 30 Pa. Fig. 4.8 shows the net result when the 1-sigma uncertainty in T_b is set to 10 K. Both σ_T and σ_p decrease steadily with increasing pressure; their values in this example are approximately 7% at the top of the profile, 1% at 50 Pa, and 0.1% near the surface.

4.2.2. Global temperature structure

Radio occultation profiles are generally limited with regard to their spatial coverage. Nevertheless, significant conclusions about the global atmospheric structure can be drawn due to the extensive MaRS data set, extending over more than 4 Mars Years.

4.2.2.1. Variations with latitude. The orbit of Mars Express provides broad occultation coverage in latitude, as shown in Fig. 4.3. These observations provide an excellent database for the characterization of the latitudinal atmospheric temperature field. Fig. 4.9 shows a typical example for the northern hemispheric late autumn/early winter season (Ls = 253°–274°, MY 27 (2005), from Tellmann et al., 2013). The first measurements were recorded at lat: ~40° N (local time ~10:30 h), the last measurements at lat: ~75° N (local time: 15:00 h). As the measurements are distributed evenly in longitude, the temperature field in Fig. 4.9 is treated as a zonal average (see. Tellmann et al., (2013) for further details). The nearly isothermal mid-latitude region (~55° N) separates a deep temperature inversion in the equatorward region from the very cold near polar atmosphere. The high latitudinal region shows increasing temperatures in the upper atmosphere, correlated with adiabatic heating in the subsiding branch of the Hadley circulation, possibly in combination with contributions from breaking atmospheric waves (e.g. Barnes, 1990; Medvedev and Hartogh, 2007). These findings are in good agreement with results from the Thermal Emission Spectrometer (TES) on MGS (Smith et al., 2001a, 2001b) and the Mars Climate Sounder (MCS) on the Mars Reconnaissance Orbiter (McCleese et al., 2008, 2010).

Further insight into large scale atmospheric processes can be gained by applying the gradient wind equation (e.g. Holton, 2004) to the occultation measurements of pressure, density, and geopotential height. The zonal wind field is inferred by assuming that the centrifugal and Coriolis forces are balanced by the pressure gradient:

$$\frac{u^2 \tan\varphi}{r_M} + 2\Omega u \sin\varphi + \frac{1}{r_M \rho}\left(\frac{\partial p}{\partial \varphi}\right)_{z\,=\,const} = 0 \qquad (4.2.4)$$

where u is the zonal wind speed (positive eastward), ϕ is latitude, r_M is the planetary radius, Ω is the rotation rate of Mars, ρ is the atmospheric mass density, and the derivative is evaluated on a surface of constant geopotential height.

Fig. 4.10 shows the zonal wind field implied by the occultation measurements in Fig. 4.9. (See Tellmann et al. (2013) for a detailed discussion of the procedure used to derive these results.) A strong eastward winter polar jet (up to 170 m/s) can be found at latitudes around 65° N at the upper end of the investigation range (~ 15 Pa ≈ 30 km). These winter zonal jets are known to be especially pronounced around winter solstice (e.g. Banfield et al., 2003; Smith et al., 2001a, 2001b; McCleese et al., 2010). See Tellmann et al. (2013) for a more detailed discussion.

4.2.2.2. Longitudinal temperature structure. Some Mars Express occultation seasons provided an opportunity to study zonal

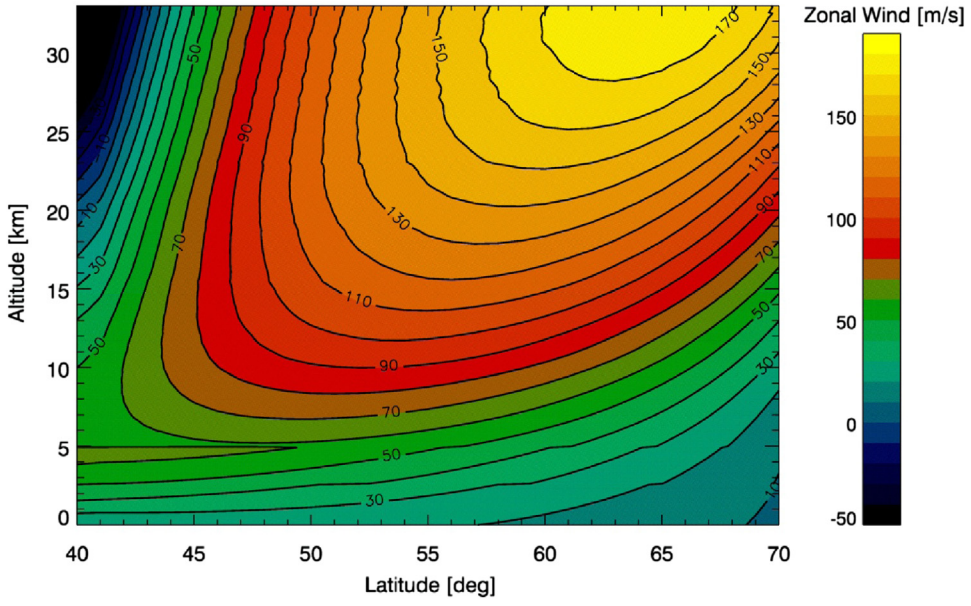

Fig. 4.10. Zonal gradient winds derived from the temperature measurements in Fig. 4.9. The pressure values are slightly corrected for seasonal CO_2 depletion. Figure taken from Tellmann etal., (2013).

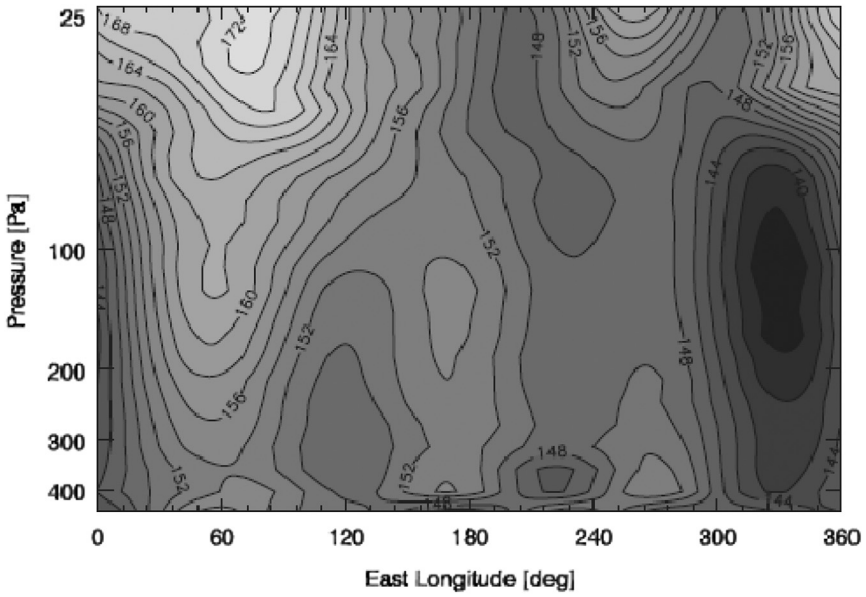

Fig. 4.11. Stationary component of the temperature field in the southern winter hemisphere (Ls = 61–110° °, MY 30, lat: 49–69° S) in the early afternoon (LT: ≈ 13.1–14.0 h). The contour interval is 2 K. (reproduced from Tellmann et al., 2013).

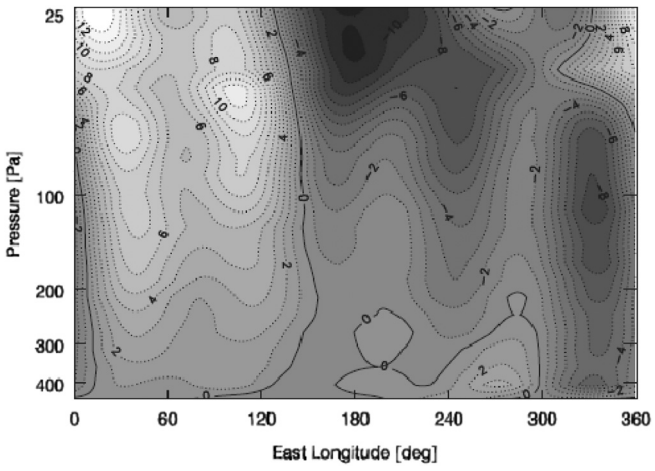

Fig. 4.12. Zonal temperature variations corresponding to the temperature field in Fig. 4.11. Zonal wave numbers $s = 1$–4 are included (see Eq. (4.2.6)). The contour interval is 1 K. The solid line denotes the zero difference level. (reproduced from Tellmann et al., 2013).

variations in atmospheric structure at nearly fixed latitude. A subset of observations from occultation season 11 (MY 30, 2011), for example, provided a good longitudinal coverage within the latitude range of 49–69° S around southern winter solstice (L_s = 61–110°) in the early afternoon (local time: ≈ 13.1–14.0 h).

The quasi-stationary component of the temperature field $\langle T\rangle$ at fixed latitude can be represented by a zonal mean value $\overline{T}(L_s)$, depending on the solar longitude, and a zonally varying term T', depending on the east longitude λ (see Hinson et al., 2001, 2003; Tellmann et al., 2013).

$$\langle T\rangle = \overline{T}(L_s) + T'(\lambda) \tag{4.2.5}$$

Fig. 4.11 shows the quasi-stationary component of the temperature $\langle T\rangle$ derived from a least-squares analysis of the longitudinal temperature structure as a function of pressure. Condensation and sublimation lead to gradual seasonal pressure variations in the the zonal mean value $\overline{T}(L_s)$. A second order polynomial can be used to model this effect (Tellmann et al., 2013).

The zonal variations T' can be expressed as a sum of zonal harmonics:

$$T' = \sum_{s=1}^{4} T_s \cos\left(s\lambda - \psi_s\right) \tag{4.2.6}$$

where T_s and ψ_s are the amplitude and phase, respectively, of the term at zonal wave number s. An equivalent approach can be used to approximate the geopotential altitude $\langle Z\rangle$ (4.2.5) and (4.2.6) were used to obtain least-squares solutions of the free parameters for the occultation measurements from season 11 at different pressure levels (see Tellmann et al. (2013) for further details). Fig. 4.11 shows the resulting representation of the quasi-stationary component of the temperature field. The most striking feature in Fig. 4.11 is a pronounced wave-1 structure with a relatively warm east hemisphere (lon: 0°–120° E) and a cold west hemisphere, with the coldest temperatures located at east longitudes of ~330° E (~144 K). This result is in general good agreement with findings from Hinson et al., (2003) and Banfield et al., (2003).

The stationary Rossby waves present in the Mars winter hemisphere are thought to be exited by the interaction of strong zonal winter jets with the pronounced topographical features on the surface (Hinson et al., 2003, Banfield et al., 2003, Wilson, 2002). The Planetary Fourier Spectrometer (PFS) on Mars Express also reported two distinct regional climates around the South pole with very cold temperatures below the CO_2 condensation temperature in the western hemisphere (lat: ~85° S; lon: ~330° E) and a much warmer eastern hemisphere at longitudes between 30°–210° E during the late autumn season of MY 27 [Giuranna et al., 2008]. These two distinct hemispherical climates are associated with dynamical forcing by the two large impact bassins, Hellas and Argyre, which are mainly responsible for the excitation of the planetary wave (Giuranna et al., 2008).

Fig. 4.12 shows the zonal variations in temperature, T', for the measurements from occultation season 11. The wave-1 structure dominates the zonal variations in the middle and upper investigation range (≥ 250 Pa), while the temperature field close to the surface is more chaotic with the highest (lowest) values at ~60° E (330° E), respectively (Tellmann et al., 2013). The temperature variations in Fig. 4.12 are associated with stationary Rossby waves, which appear seasonally in the baroclinic zone surrounding the winter pole (Banfield et al., 2003; Hinson et al., 2003). This type of "forced" atmospheric wave arises when eastward zonal winds

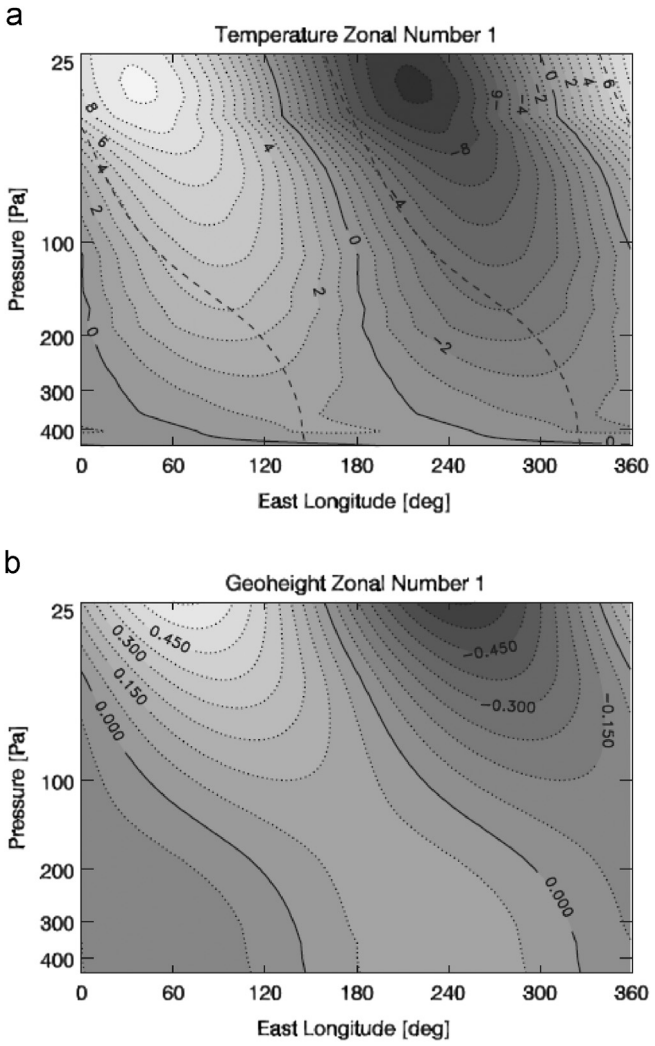

Fig. 4.13. Wave-1 temperature (a) and geopotential height (b), corresponding to the temperature field in Fig. 4.11 and Fig. 4.12. The contour intervals are (a) 1 K and (b) 0.075 km. The solid line indicates the zero difference level. The dashed line in Fig. 4.13a indicates the zero-difference level of the geopotential height from 4.13b. (reproduced from Tellmann et al., 2013).

encounter planetary-scale variations in surface topography (Gill, 1982). The eastward jet in the zonal wind field creates a duct that allows modes with small zonal wave numbers to propagate vertically. It is informative to examine the characteristics of the harmonic components of T'. We focus attention on the dominant wave-1 component of the structure in Fig. 4.12. Banfield et al. (2003) have shown that the wave-1 component is dominating around winter solstice, while the wave-2 component becomes increasingly important during mid and late winter.

Fig. 4.13 shows cross sections of the variations in both temperature and geopotential height at $s=1$. The *wave-1* amplitudes of temperature and geopotential height grow steadily with increasing altitude, reaching values of 10 K and 600 m at the upper boundary of the investigation range. The progressive westward phase shift of the wave-1 field is indicative for an effectively upward propagating group velocity and forcing on the ground (e.g. Andrews et al., 1987).

Rossby waves produce a meridional heat flux that depends on the relative zonal phase of the temperature and geopotential fields. The eddy heat flux is largest when T' and Z' are in quadrature, whereas there is no net heat flux when T' and Z' are in phase. For the case shown in Fig. 4.13 the relative phase shift between T' and Z' is ~60°–90°, indicating an effective poleward eddy heat flux (Tellmann et al., 2013).

4.2.3. Simultaneous observations by MEX and MGS

Radio occultation observations with MEX and MGS include brief periods of near-coincident observations at high northern latitudes in MY 27, first at $Ls=274°$ and again at $Ls=333–345°$, as shown in Fig. 4.5. We make use of these observations to validate the radio occultation measurements of temperature and geopotential height.

First consider the temperature measurements. As the result of a fortuitous alignment of MEX and MGS on 23 August 2005, the occultation paths of the two spacecraft probed the atmosphere at essentially the same time and location (see Hinson et al., 2008a). These observations occurred during the winter solstice (Ls=274° of MY 27) at a location adjacent the permanent north polar cap (70°E, 76°N). The observing geometries differ primarily in the distance between the spacecraft and the limb of Mars, 1800 km for MGS and 11,400 km for MEX. The offsets in time of observation (13 min), longitude (0.4°), latitude (0.1°), and local time (10 min) are negligible.

Fig. 4.14 compares the temperature profiles retrieved from this pair of measurements (Hinson et al., 2008a). The maximum difference is ~1 K, consistent with our estimate of the 1-sigma uncertainty σ_T throughout the pressure range of the profiles, 5–900 Pa. In particular, both profiles remain close to CO_2 saturation at pressures exceeding 200 Pa, and their mutual consistency supports the reliability of the result.

The comparison in Fig. 4.14 also illustrates the value of km-scale vertical resolution. The two profiles reveal striking similarities in their small-scale temperature fluctuations, probably associated with vertically propagating gravity waves. In this example the wave produces several local minima in temperature below the 200-Pa pressure level that are slightly colder than saturation, a condition which could initiate CO_2 condensation (cf., Tobie et al., 2003).

We use a different approach to validate the radio occultation measurements of geopotential height. Rather than focusing on individual profiles, we compare results derived from an extended sequence of observations in late winter of MY 27 and early spring of MY 28, when the coverage by the two spacecraft is highly complementary as shown in Fig. 4.5. The MEX observations range in latitude from 67°N to 6°S (Ls=327-43°), while the MGS observations provide dense sampling in longitude at 72°N to 61°N (Ls=319–355°). The overlapping coverage by the two spacecraft thus extends over latitudes 67-64°N and solar longitudes Ls=333–345°.

Fig. 4.15 shows more than 600 measurements of geopotential height at the 400-Pa pressure level, Z_{400}, extracted from these subsets of MEX and MGS observations. In response to the seasonal cycle of CO_2 condensation and sublimation, Z_{400} changes by a few hundred meters during the span of the observations considered here. This seasonal effect has been modeled using surface pressure measurements by Viking Lander 1 (e.g., Zurek et al., 1992) and removed from the data in Fig. 4.15.

The results in Fig. 4.15 are consistent for the above mentioned coverage overlaps in *Ls* and latitude, confirming the reliability of the measurements by the two spacecraft. In addition to validating the radio occultation observations of Z_{400}, Fig. 4.15 also characterizes the atmospheric structure and dynamics in the northern hemisphere during winter. The MEX measurements reveal a steep gradient in Z_{400} at the boundary of the polar vortex, near 60°N, where the eastward zonal wind speed implied by geostrophic balance is about 50 m s^{-1} (cf. Tellmann et al., 2013). These strong zonal winds are

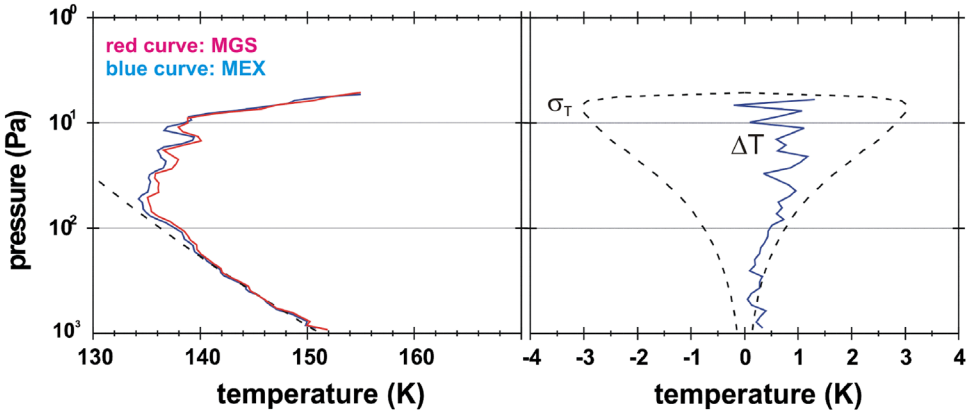

Fig. 4.14. Results obtained from nearly coincident measurements by MEX and MGS on 23 August 2005. In observations separated by 13 min, the two spacecraft sounded the atmosphere at essentially the same location near the winter pole (70°E, 76°N, Ls=274° of MY 27). Left panel: Temperature profiles from (blue) MEX and (gray) MGS agree to within 1 K and exhibit nearly identical small-scale structure. The dashed line is the saturation vapor pressure of CO_2. This figure is adapted from Hinson et al. (2008a). Right panel: A comparison of (blue) the difference in temperature ΔT between the MEX and MGS profiles and (dashed) the standard deviation of the measurements σ_T. This estimate of σ_T excludes the contribution from the uncertainty in T_b, which is the same for both profiles.

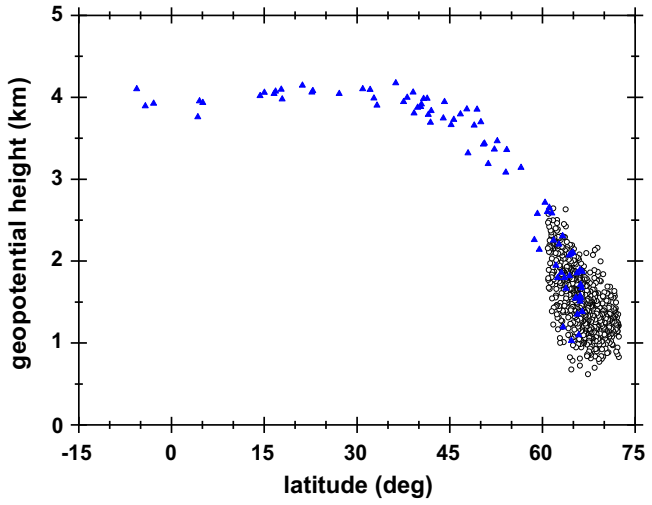

Fig. 4.15. Radio occultation measurements of Z_{400} by (blue) MEX and (gray) MGS from late winter of MY 27 and early spring of MY 28. A small correction has been applied to remove the seasonal trend associated with CO_2 condensation and sublimation. Within this set of observations, the measurement uncertainty is typically 20–30 m, barely discernible on the scale of this figure.

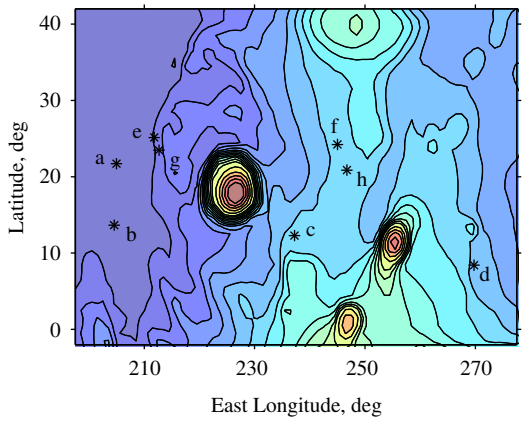

Fig. 4.16. Locations of selected radio occultation observations from midspring of MY 27 (a to d) and early spring of MY 28 (e to h). The map of topography is derived from measurements by the MGS Mars Orbiter Laser Altimeter (Smith et al., 2001a, 2001b), with a contour interval of 1 km at elevations below 8 km, increasing to 2 km at higher elevations on the flanks of the volcanoes. Table 4.2 lists the surface elevation at the location of each measurement.

Table 4.2
Properties of the CBL derived from MEX radio occultation measurements in the northern tropics.

Label	MY	Ls (°)	LT (h)	λ (°)	ϕ (°)	D (km)	z_s (km)	θ_{CBL} (K)
a	27	47.1	17.2	205.0	21.8	5.1	−3.9	218.6
b	27	51.2	17.2	204.6	13.7	4.2	−3.6	219.4
c	27	52.1	17.2	237.2	12.3	8.2	+2.4	244.6
d	27	54.3	17.1	269.8	8.4	9.5	+1.8	248.6
e	28	23.0	15.5	211.8	25.2	5.8	−3.0	221.7
f	28	23.9	15.6	245.0	24.2	7.4	+2.5	248.3
g	28	24.5	15.6	212.7	23.5	5.6	−2.8	223.0
h	28	26.8	15.7	246.8	20.9	8.6	+2.5	251.7

Notes: In the table headings, MY is Mars Year, LT is local true solar time, D is the depth of the CBL, z_s is the surface elevation, and θ_{CBL} is the average potential temperature in the mixed layer.

associated with very low pressure near the northern pole in late winter. Within the polar vortex at 70°N, Z_{400} is about 3 km lower than its value at midlatitudes.

The MEX observations in Fig. 4.15 provide broad latitude coverage while the more numerous MGS measurements are concentrated in latitude near the edge of the polar vortex. The value of Z_{400} within the MGS data at a given latitude varies by hundreds of meters in response to modulation imposed by eastward-traveling baroclinic waves (e.g., Hinson and Wang, 2010; Hinson et al., 2012). The sampling rates of these MGS observations in time and longitude are sufficient to avoid aliasing, so that the basic properties of the traveling waves can be determined through space-time analysis. The dominant mode within this subset of observations has a zonal wavenumber s=1, a period of ≈ 8 sols, and an amplitude of 280 m at the 400-Pa pressure level. It first appears shortly after $Ls=330°$ and persists until about $Ls=350°$, achieving its peak amplitude at $Ls=340–345°$.

4.2.4. The convective boundary layer

Many basic characteristics of the daytime convective boundary layer (CBL) remain poorly understood owing to its intricacy, the scarcity of in situ observations, and the difficulty of sounding this region from orbit. The MEX radio occultations have provided the first precise measurements of the depth of the CBL and its variations with location and season. This unique capability is a consequence of the excellent vertical resolution of the retrieved profiles along with their broad coverage in latitude and longitude, which includes sampling of the tropics at local times in the late afternoon.

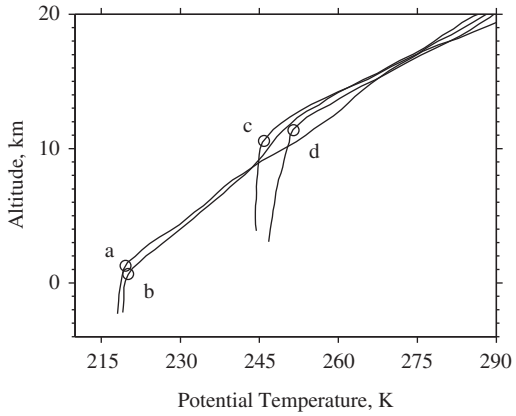

Fig. 4.17. Selected radio occultation profiles of potential temperature θ from midspring of MY 27 for the locations indicated in Fig. 4.16. Altitude is measured from the same reference as surface elevation. The bottom of each profile is roughly 1 km above the ground. Circles mark the top of the CBL, as determined from a static stability criterion. The depth of the CBL varies strongly with surface elevation, increasing from 4-5 km for the Amazonis profiles (a and b) to 8-10 km for the Tharsis profiles (c and d). This figure is adapted from Hinson et al. (2008b).

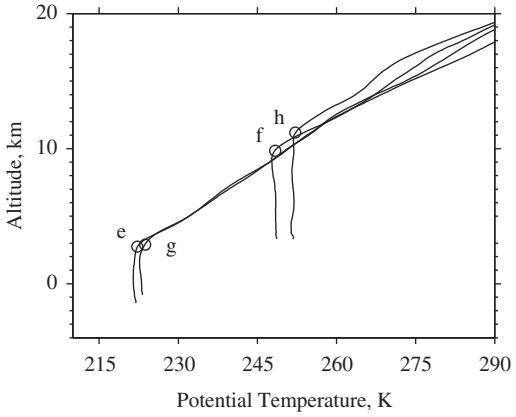

Fig. 4.18. Selected radio occultation profiles of potential temperature θ from early spring of MY 28. The measurement locations are shown in Fig. 4.16. As in Fig. 4.17, the Tharsis profiles (f and h) have a deeper CBL than the Amazonis profiles (e and g), and the potential temperature in the mixed layer is warmer by ~30 K at the higher elevation. See the caption to Fig. 4.17 for additional discussion. This figure is adapted from Tellmann et al. (2013).

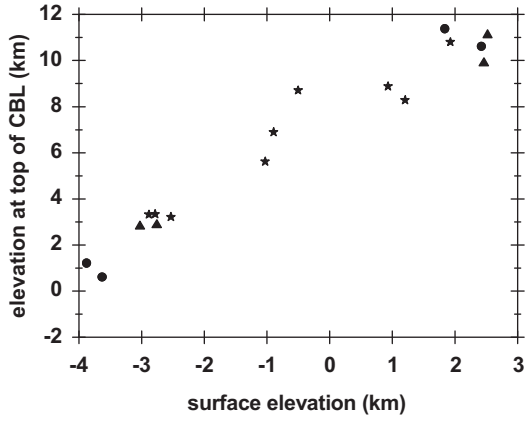

Fig. 4.19. Variation in the altitude at the top of the CBL (z_t) with surface elevation (z_s) as determined from the radio occultation measurements in Fig. 4.17 (circles) and Fig. 4.18 (triangles). The figure includes results derived from other radio occultation measurements in the northern tropics at longitudes of 190-340°E during midspring of MY 27 (Hinson et al., 2008b), as indicated by stars.

About 80% of the MEX radio occultation profiles obtained in the tropics in late afternoon reveal a well-mixed CBL with a distinct upper boundary (cf. Fig. 4.7). We have analyzed these profiles to determine properties such as the depth of the CBL, the potential temperature within the mixed layer, and their response to variations in surface conditions (Hinson et al., 2008b; Tellmann et al., 2013). Observations accumulated from several seasons consistently show that the depth of the CBL is strongly correlated with variations in surface elevation, or, equivalently, strongly anti-correlated with variations in surface pressure. In general, the CBL is 8–10 km deep where the surface elevation is high, as in the Tharsis region and Syrtis Major, and shallow (4–6 km) where the surface elevation is low, as in Amazonis, Utopia, and Isidis. Owing to this "pressure effect," the elevation at the top of the CBL varies with longitude by more than 10 km (at fixed local time), resulting in strong zonal modulation in the vertical mixing of dust, water vapor, heat, and momentum, as well as modulation in the spatial structure of the aphelion cloud belt. The depth of the CBL also depends on surface temperature, which varies (at fixed local time) with latitude relative to the sub-solar point and with surface properties (albedo and thermal inertia).

In reviewing the results to date, we compare and contrast observations from eastern Amazonis and the Tharsis region, at the locations shown in Fig. 4.16 and listed in Table 4.2. The first four profiles, labeled a-d, are from Ls = 47–54° of MY 27, while the other four profiles, labeled e-h, are from Ls = 23–27° of MY 28. The group of profiles from each year includes a pair from Amazonis and a pair from the Tharsis region. The surface elevation z_s ranges from a minimum of −3.9 km in Amazonis (location a) to a maximum of +2.5 km in the Tharsis region (locations f and h), but all eight locations are well separated from the nearest volcanoes, Olympus Mons and Ascraeus Mons.

Fig. 4.17 shows the MEX radio occultation profiles of potential temperature θ from midspring of MY 27. All observations were obtained at LT = 17.2 h, i.e., late afternoon. The surface elevation is ≈ 6 km higher for the Tharsis profiles (c and d) than for the Amazonis profiles (a and b), and the CBL is also ≈ 4 km deeper at the higher elevation. This results in a net change of roughly 10 km in the altitude at the top of the mixed layer z_t, increasing from ≈ 1 km to ≈ 11 km between the Amazonis and Tharsis profiles.

The potential temperature in the mixed layer θ_{CBL} is warmer by ≈ 30 K for the Tharsis profiles than for the Amazonis profiles. This is primarily a consequence of the decrease in surface pressure at the higher elevation (see 4.1.2). The change in the physical temperature T at the base of each profile is small in comparison (Hinson et al., 2008b).

Fig. 4.18 shows analogous results from the same regions in early spring of MY 28. The local time within this group of observations is 15.6 h. The Amazonis and Tharsis profiles closely

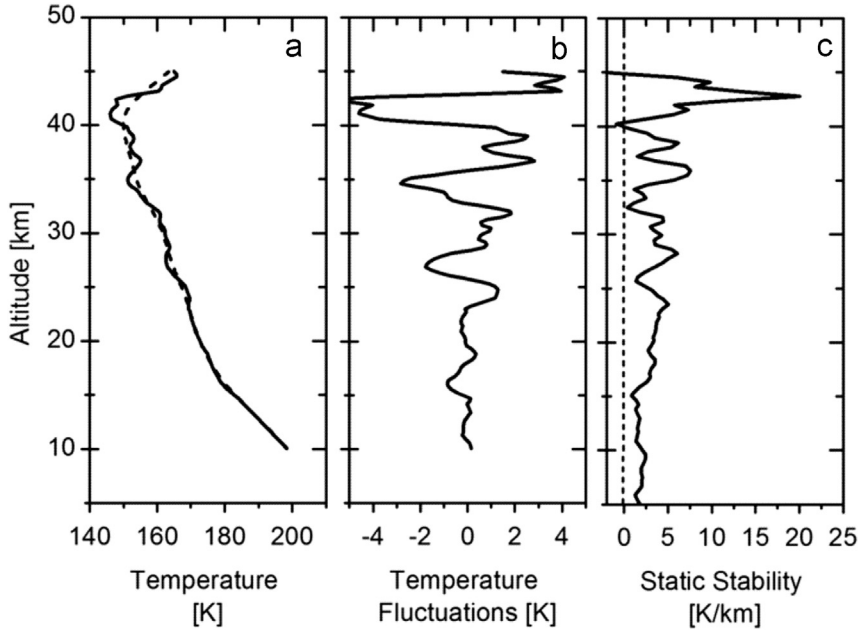

Fig. 4.20. (a) Typical MaRS temperature profile (solid line) and low-pass filtered temperature profile (dashed line) for 2004 DOY 202, at Ls = 63.0° in MY 27, with coordinates 5.1° S, 138.6° E, LT = 17.05. The low pass filter eliminates all temperature fluctuations with vertical wavelengths shorter than 10 km. (b) Difference between the two temperature profiles shown in (a). (c) Static stability of the profile. Negative values indicate regions of convective instability.

resemble their counterparts from the preceding year. As before, the CBL is distinctly deeper at the higher elevation, and z_t increases from ≈ 3 km in the Amazonis profiles to ≈ 11 km in the Tharsis profiles. The basic characteristics of the CBL are essentially the same in both years, as summarized in Table 4.2.

Fig. 4.18 also illustrates the high degree of consistency between measurements on different sols at nearly the same location. There was little change in the temperature structure in the 3-sol interval between the closely spaced observations in Amazonis (profiles e and g). In the 6-sol interval between the observations in the Tharsis region (profiles f and h), the potential temperature in the mixed layer increased by ≈ 3 K and the depth of the CBL increased by ≈ 1 km.

The plots of potential temperature in Figs. 4.17 and 4.18 are helpful for understanding the effect of surface elevation on z_t and the depth of the mixed layer D, as there is little variation in surface albedo or thermal inertia among these eight locations. Fig. 4.19 summarizes the results. The measurements from the two years of observations follow a well-defined linear trend, with D increasing by ≈ 4 km and z_t increasing by ≈ 10 km in response to a 6-km increase in elevation z_s.

These radio occultation observations provide important new constraints for validation and further development of quantitative geophysical models of Mars such as large-eddy simulations of the structure and dynamics of the mixed layer (Spiga et al., 2010) as well as the UK spectral version of the LMD Mars Global Circulation Model (MGCM) (Lewis et al., 2011; Hinson et al., 2011).

4.2.5. Gravity waves

Gravity waves play a significant role in the energy and momentum budgets of planetary atmospheres. The restoring force that enables wave propagation is the buoyancy force inherent to a stably stratified atmosphere. These waves are generated by a variety of mechanisms including penetrative convection, wind shear instability, and fluid motion over topographic obstacles such as volcanoes and craters (Fritts and Alexander, 2003).

With their exceptional vertical resolution, radio occultation measurements provide unique insight into gravity waves with vertical wavelengths smaller than one pressure scale height, about 10 km on Mars. This segment of the gravity-wave spectrum is not currently accessible with other remote sensing techniques.

Many of the MEX occultation profiles contain signs of gravity-wave activity, as reported previously by Tellmann et al. (2013). In particular, gravity waves impose distinctive modulation on the temperature profile, as illustrated in Fig. 4.20. We gain further insight by using a digital filter to separate the profile into two components: (1) the background structure through which the wave propagates, shown by the dashed line in Fig. 4.20a, and (2) the temperature variations associated with the wave, shown in Fig. 4.20b. The filter is designed to isolate gravity waves with vertical wavelengths smaller than 10 km.

The dominant vertical wavelength of the temperature variations in Fig. 4.20b is 3-4 km. The amplitude grows steadily with increasing altitude – an intrinsic feature of freely propagating gravity waves – increasing from less than 1 K to more than 4 K in a span of 35 km. At altitudes above 30 km the amplitude is sufficient to trigger convective instability, as indicated by negative values of the static stability in Fig. 4.20c.

Fig. 4.21 compares observations of gravity waves from disparate topographical regions. The wave amplitude is modest, generally less than 1 K, in the northern lowlands (panel a and b) In contrast, waves with larger amplitudes and longer vertical wavelengths appear over elevated terrain above the Tharsis ridge (panel c and d). (Tellmann et al., 2013). The observations in Fig. 4.21c and d may reflect the presence of lee waves, a type of gravity wave excited when horizontal winds encounter the giant shield volcanoes (Creasey et al., 2006; Briggs and Leovy, 1974). A second physical process may also contribute to the increase in gravity wave activity observed in regions of high surface elevation. As discussed in Section 4.2.4, the CBL achieves its maximum depth above elevated terrain. Moreover, numerical models show that updrafts grow stronger as the CBL becomes deeper (Spiga et al., 2010), possibly leading to more intense penetrative convection and stronger excitation of gravity waves in regions of high surface elevation. See Creasey et al. (2006) and Tellmann et al. (2013) for further discussion of the diurnal, seasonal, and topographical variations in gravity wave activity on Mars.

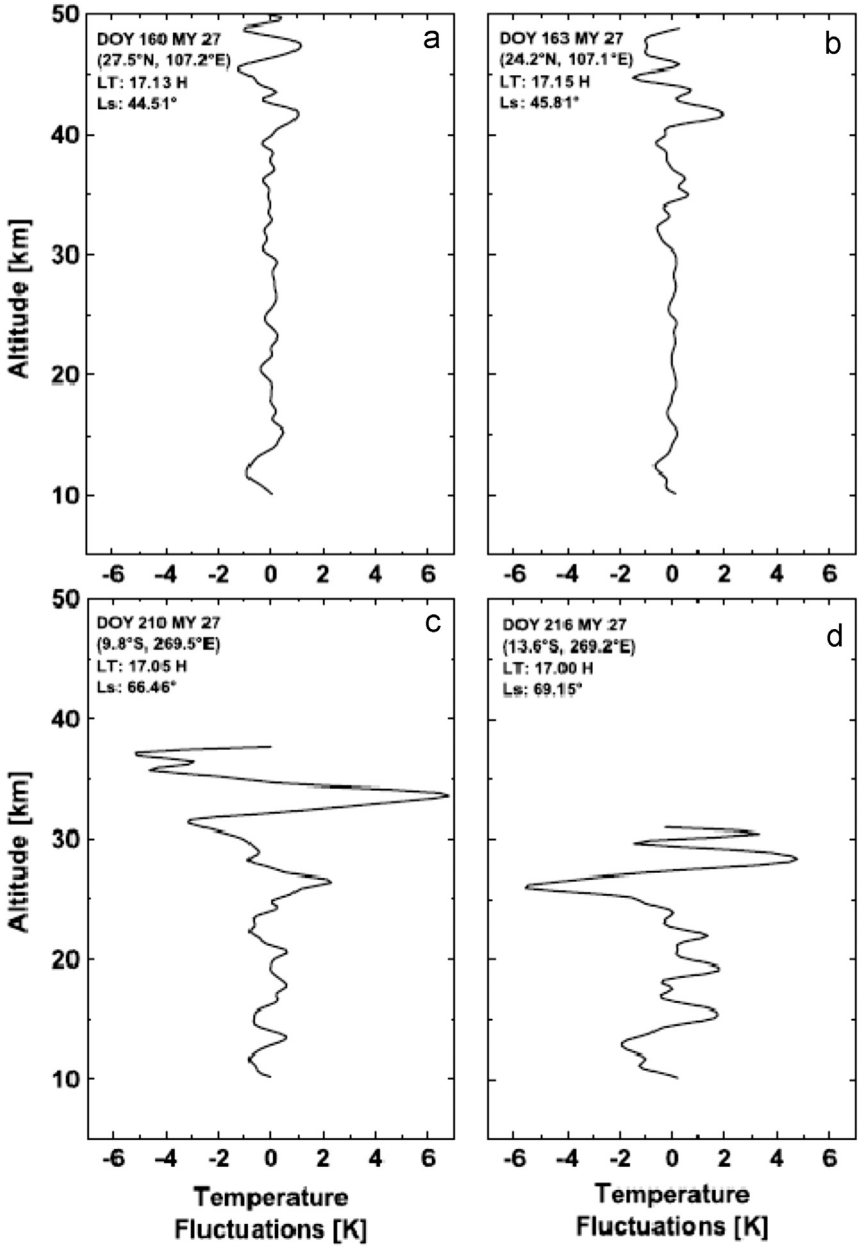

Fig. 4.21. Typical temperature fluctuation profiles in different topographical regions. (a) and (b) are located in the northern lowlands (c) and (d) are located on elevated terrain close to Valles Marineris. (Reproduced from Tellmann et al., (2013)).

4.3. Radio sounding of the ionosphere

4.3.1. Formation of the ionosphere

In situ observations of ion densities and ion/electron temperatures by the Viking landers, supported by many radio occultation measurements of electron density profiles from the Viking orbiters and earlier missions, showed that the vertical structure of the dayside Martian ionosphere contains both a photochemically-controlled region at 80–200 km altitude and a transport-controlled region above 200 km (Chen et al., 1978; Barth et al., 1992; Shinagawa, 2000; Fox, 2004). The dominant ion below 300 km is O_2^+ (Hanson et al., 1977; Chen et al., 1978; Fox, 2004). The upper boundary of the ionosphere is found at the altitude where electrons of Martian origin are separated from those of solar origin (e.g., Nagy et al., 2004; Brain, 2006). The interaction of the solar wind with the ionosphere controls this boundary and its typical altitude varies significantly with time and solar cycle (Mitchell et al., 2001; Brain, 2006; Duru et al., 2009).

4.3.2. Electron density profiles

The refractivity profile μ(z) in Fig. 4.2 changes sign from negative (as defined for propagation of radio waves through predominantly ionospheric plasma) to positive (propagation through a predominantly neutral atmosphere). Above an altitude of about 70 – 80 km, the electron density is directly proportional to the (negative) refractivity by

$$N_e(z) = -\mu(z)\frac{f_0^2}{40.31 \cdot 10^6 m^3 s^{-2}} \quad (4.3.1)$$

The refractivity profile (example in Fig. 4.2) thus reflects already the structure of the ionosphere.

4.3.3. Electron density profiles derived from single-frequency (X-band) or differential Doppler

The electron density profile in Fig. 4.22 (black dotted profile) was derived from X-band frequency residuals processed as described in the previous sections. Fig. 4.22, also displays an

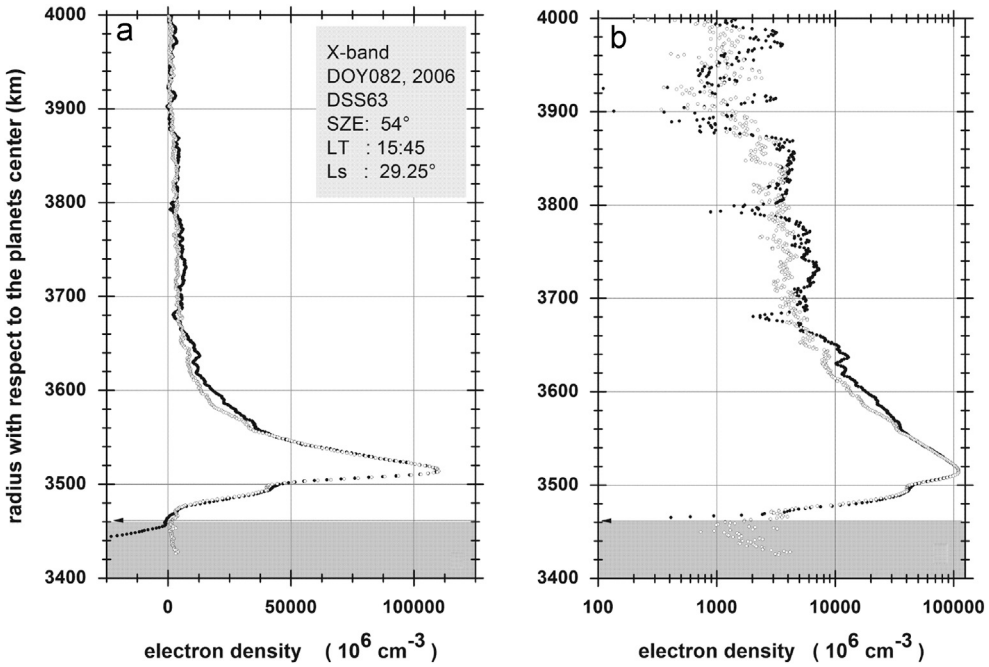

Fig. 4.22. Electron density profile from the Martian ionosphere computed from the refractivity profile in Fig. 4.1, observed on 2006 DOY 082 with linear (left) and semi-logarithmic (right) scales on the abscissa. The gray points are from differential Doppler data; the blue points from X.band data only. The dominant features are the two layers M1 and M2, the "bulge", the transport region and the ionopause.

electron density profile from the same occultation on 2006 DOY 082 (gray dotted profile), but derived from the differential Doppler (3.5). The resulting frequency residuals are similar to those derived from the single X-band (Fig. 3.1), but with the difference that the differential Doppler residuals no longer contain residual Doppler frequency shifts that are linear in frequency (e.g., unmodeled differences in radial velocity).

Although the two profiles in Fig. 4.22 appear similar with respect to the overall ionospheric structure, there are two distinct differences:

i) The electron density profile derived from the single X-band frequency in Fig. 4.22 appears more wavy in the topside and shows a weaker slope in the diffusion region than the profile computed from the differential Doppler. The absence of the wavy structures in the topside is easily explained: small-amplitude, short-period motion of the spacecraft body with a velocity component along the LOS leads to periodic perturbations in the Doppler shifts at both downlink frequencies X-band and S-band. These perturbing Doppler shifts are eliminated upon computing the differential Doppler but are still contained in the X-band frequency residuals. The perturbed single X-band frequency residuals are incorrectly translated into periodic fluctuations in electron density. In general, contributions by periodic or stochastic (vibrational) motion lead to a strongly perturbed electron density profile derived from the single X-band frequency residuals, while the electron density profile derived from the differential Doppler remains smooth (Fig. 4.22). Electron density profiles derived from single frequency may tempt the observer to misinterpret intriguing, but unrealistic, features or structures (e.g., such as wave-like structures in the upper ionosphere).

ii) The refractivity profile (example: Fig. 4.2) changes sign at 60–80 km altitude, at which point the propagation of the radio wave starts to be dominated by the neutral atmosphere. Note that the X-band electron density profile in Fig. 4.22 also changes sign. This altitude more or less defines the sensible base of the ionosphere by radio waves and the electron density profile derived from the differential Doppler in Fig. 4.22 becomes roughly zero below this altitude. The refractivity below about 80 km is dominated by the neutral atmosphere and should not be interpreted in terms of an electron density.

4.3.4. *Structure of the ionosphere*

The ionospheric electron density profile in Fig. 4.22, computed, from the refractivity profile in Fig. 4.2 using (4.3.1), illustrates a dominant two layer structure, a topside bulge of unknown origin typically located between 180 km to 220 km, a transport and diffusion region with varying plasma scale height, and a weak ionopause, which is often obscured by system noise.

The dominant feature of the ionospheric structure is the photochemically-controlled main layer, dubbed M2[2]. The peak ionospheric electron density is reached in the M2 layer, produced by solar EUV irradiance (Fox and Yeager, 2006; Withers, 2009). The M2 peak at the subsolar point occurs at an altitude of approximately 120 km. The peak density and altitude of the M2 layer vary with the solar zenith angle and the input of solar flux (see following sections). Only 10 – 20% of the peak density is formed by secondary ionization of photo-electrons (Peter et al., 2014).

A second layer with smaller density, dubbed M1, lies below the main layer by approximately 20 km (Fox, 2004; Pätzold et al., 2005; Mendillo et al., 2006; Withers, 2009). Highly variable with time, the M1 layer is produced by the absorption of solar soft X-ray irradiance. Since these photons are highly energetic, the associated photoelectrons are also highly energetic and produce additional ion-electron pairs via electron impact ionization as they thermalize.

[2] Rishbeth and Mendillo (2004) started to call the layers in the Martian ionosphere M1 and M2 for the lower layer and the main layer, respectively, in order to distinguish the notation from the Earth ionospheric layers. Some authors call the Martian ionospheric D, E and F layers because of their similar formation. We follow the more reasonable notation by Rishbeth and Mendillo (2004).

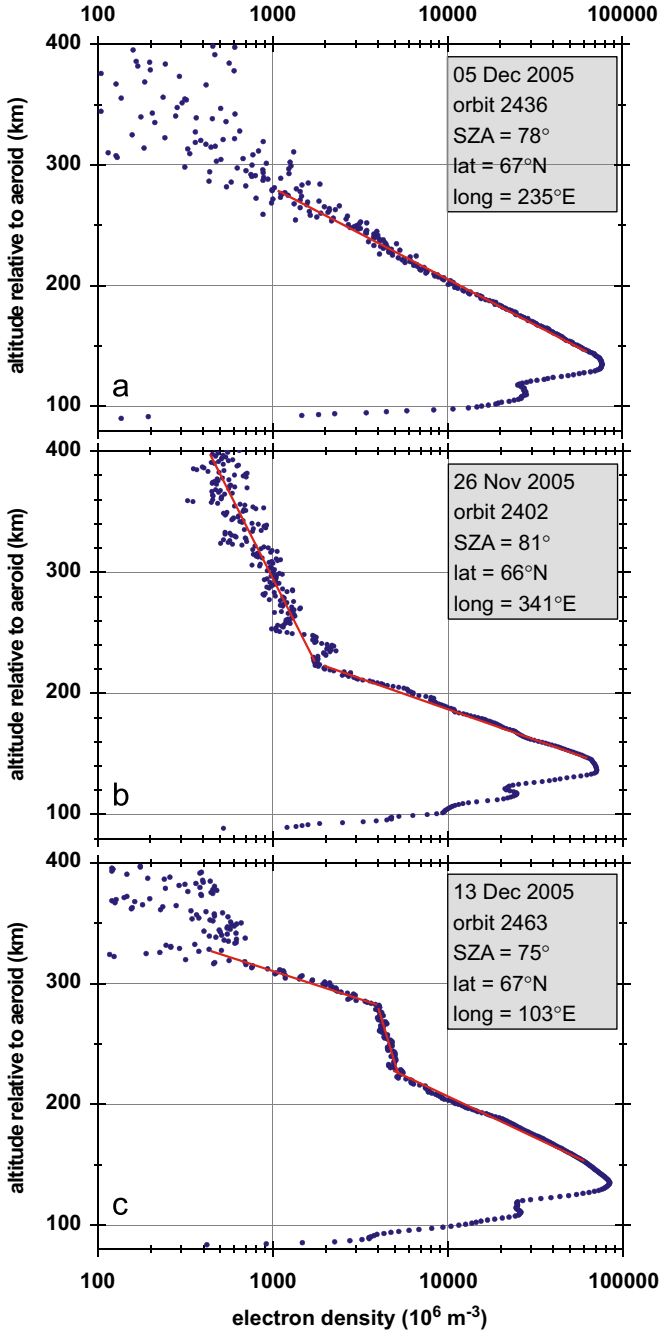

Fig. 4.23. Three electron density profiles illustrating different structures in the topside ionosphere. Latitude, longitude, solar zenith angle (SZA), orbit number, and UTC date are shown. All local times are 12:00 to 14:00 h. (a) The red solid line is an exponential fit to densities between 150 km and 275 km that has a scale height of 33 km. (b) The lower and upper red lines are exponential fits to densities at 150 – 220 km and 220 – 400 km, respectively, that have scale heights of 22 km and 120 km. (c) The lower, middle, and upper red solid lines are exponential fits to densities at 150 – 220 km, 220–280 km, and 280–315 km, respectively, that have scale heights of 28 km, 190 km, and 21 km (Withers et al., 2012a).

Above the M2 layer, in the transport-controlled topside of the ionosphere, electron densities decrease with increasing altitude, often falling off exponentially (Hanson et al., 1977; Zhang et al., 1990; Fox and Yeager, 2006; Duru et al., 2009; Mendillo et al., 2011). In the profile shown in Fig. 4.23a, the M1 layer is visible at 110 km, the M2 layer at 135 km has a classical Chapman-like shape (Withers, 2009), and the electron densitiy decreases exponentially above the M2 layer.

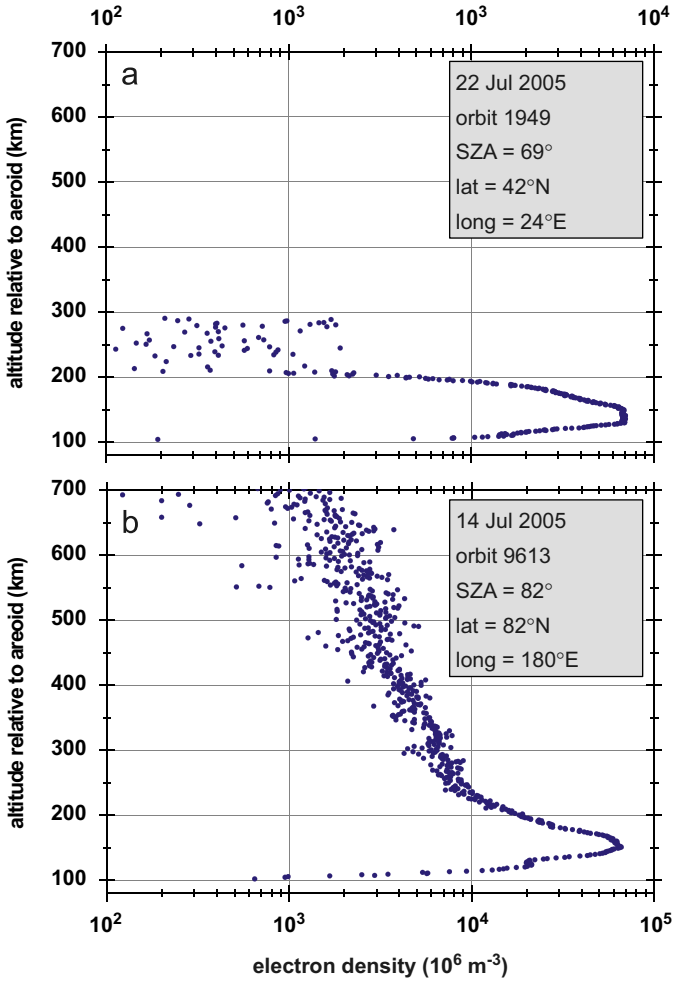

Fig. 4.24. Two electron density profiles that illustrate large variations in the vertical extent of the dayside ionosphere. Latitude, longitude, solar zenith angle, orbit number, and UTC date are shown. The local time is 11 hours in Panel A and 21 hours in Panel B (Withers et al., 2012a).

The "bulge" in the topside appears in most of the electron density profiles observed by MaRS, but has not been previously reported. Although the formation of the bulge is not yet understood, there are potential explanations. Simulations rule out photo-ionisation in the wavelength range 5 nm –95 nm (Peter et al., 2014).

The shape of the topside ionosphere is occasionally (10%) very simple – just an exponential decay in electron density with height z

$$N_e(z_0 > 180\ km) = N_0 e^{-\frac{(z-z_0)}{H_p}} \quad (4.3.2)$$

with $N_0 = N_e(z_0 = 180\ km)$ and typically characterized by a scale height on the order of $H_p \approx$ 20–30 km, that continues until the density drops below the MaRS detection threshold.

About 25% of the profiles, however, feature an exponential decay with a scale height $H_p \approx$ 20–30 km that transitions into exponential decay with a much larger scale height on the order of $H_p \approx$ 120–200 km, thereby drastically increasing the vertical extent of the ionosphere. This is illustrated in Fig. 4.24 (from Withers et al., 2012a). Such an abrupt transition in the morphology of the topside ionosphere suggests a radical change in the physical process responsible for the vertical plasma distribution, such as the onset of appreciable vertical transport. Alternatively, the physical process might remain unchanged, but a critical parameter within that process – such as the electron temperature – changes rapidly and disrupts the usual steady state.

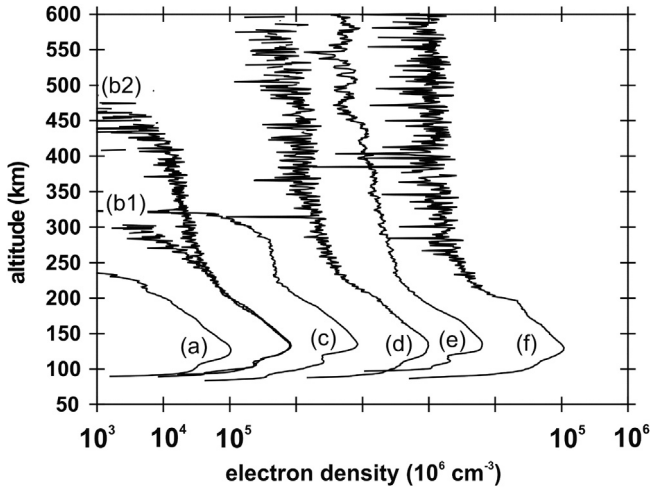

Fig. 4.25. Topside height profiles of the Martian dayside ionosphere with the following coordinates: (a) 2006 DOY 049, lon=74.5°, lat=38.6°, SZA=53.2°; (b) 2005 DOY 348, lon=332.0°, lat= 65.8°, SZA=74.8°; (c) 2005 DOY 347, lon=102.6°, lat=66.0°, SZA=75.3°; (d) 2006 DOY 028, lon=228.6°, lat=49.2°, SZA=57.5°; (e) 2005 DOY 331, lon=306.2°, lat= 66.6°, SZA=80.5°; (f) 2006 DOY 031, lon=230.2°, lat=47.7°, SZA=56.6° (Withers et al., 2012a).

The ionopause, the pressure balance boundary between the ionospheric plasma pressure and the kinetic pressure of the solar wind, is seldom fully resolved in the individual MaRS occultation profiles. The location of the ionopause in radio occultation profiles was first defined from Venus electron density profiles (Kliore and Luhmann, 1991). At Mars, Kliore (1992) adopted an electron density level of 500 el/cm^3, as the signature of the ionopause, regardless of the noise level. The electron density noise level for MaRS electron density profiles, however, depends on the Sun-Earth-Mars (SEM) elongation angle and on interplanetary coronal mass ejection (CME) or corotating interaction region(CIR) events. The lowest noise level of a few 100 el/cm^3 is encountered during Mars opposition. SEM angles larger than 90° often have a noise level $<$ 1000 el/cm^3. An ionopause as defined at Venus, with a strong density gradient merging into the noise level, could only be identified or resolved from the noise level at Mars for large SEM angles near opposition (Peter, 2008).

The altitude of the ionopause varies significantly (Fig. 4.25). In 25% of the profiles, electron densities attain values less than 10^9 m^{-3} below 250 km altitude, and in 1%, electron densities remain greater than 10^9 m^{-3} until 650 km altitude. The dayside ionosphere can have a thickness from the base to its ionopause as low as 100 km or as large as 600 km (Fig. 4.24). Temporal variations in solar wind conditions and spatial variations in the Martian magnetic environment strongly influence the vertical extent of the ionosphere.

4.3.5. *Perturbed electron density profiles*

The morphology of the main peak is remarkably variable and sometimes deviates from a smooth, rounded, Chapman-like shape. Some profiles show sharply pointed (5%), flat-topped (6%), or wavy (8%) shapes. Fig. 4.26 shows some examples and additional interesting deviations from the normal structure of the dayside ionosphere of Mars can be found in Withers et al. (2012a). Substantial gaps still remain in our understanding of the main layer of the Mars ionosphere. Sharp bumps (enhancements) and biteouts (reductions) in plasma density are observed above strongly magnetized regions of Mars at altitudes of 140–180 km, suggesting the influence of magnetic fields on either plasma transport or plasma production via precipitating particles.

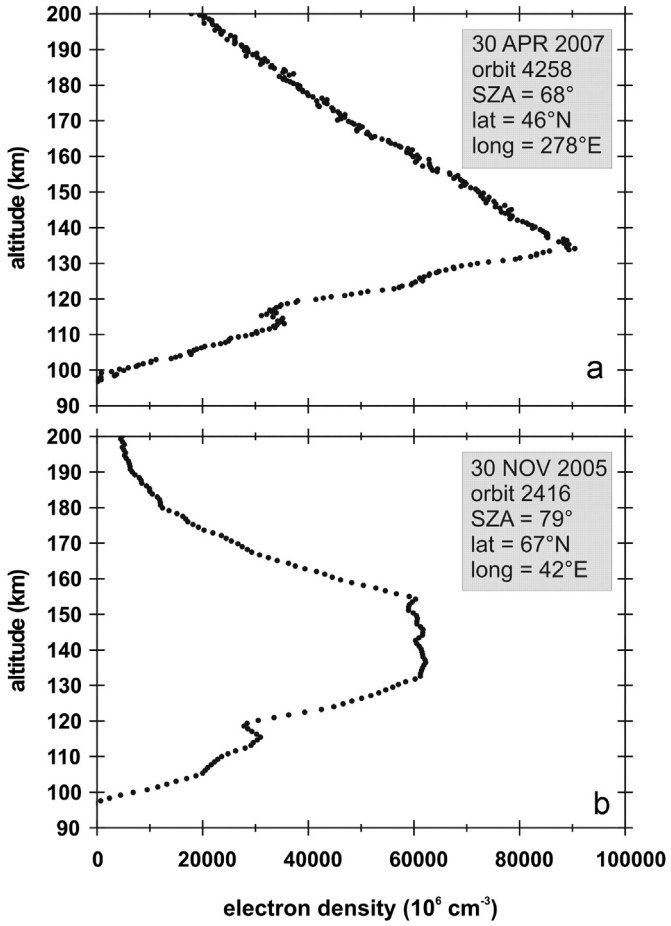

Fig. 4.26. Two electron density profiles illustrating variations in the shape of the main peak of the dayside ionosphere. Whereas the main peak is usually smoothly rounded, the profile in Panel A has a sharply-pointed main peak and the profile in Panel B has a flat-topped main peak. Latitude, longitude, solar zenith angle, orbit number, and UTC date are shown (Withers et al., 2012a).

4.3.6. *Peak density and peak altitude*

The MEX polar orbit enables good coverage of the geometrically accessible range of solar zenith angle (SZA) during the occultations. Fig. 4.27a shows the M2 peak density as a function of SZA from 50° to 130°. The large scatter of the peak density values is explained by the variable ionizing solar flux at the orbital position of Mars. The M2 peak values in Fig. 4.27a are coded according to the F10.7 radio flux index, a proxy for solar activity (Peter et al., 2014). Most of the peak values have been observed at times with low or moderate solar flux and are substantially lower than those observed during high solar activity, substantiating the hypothesis that the peak density is under solar control (Mendillo et al., 2003; Fox & Yeager, 2009; Peter et al., 2014) and indicating a generally warmer atmosphere at 130 km altitude at solar maximum than at solar minimum (Peter et al., 2014). The peak densities are usually compared with the Chapman relation

$$N_{e,\,\max}(SZE) = N_{e,\,\max}(SZE = 0) \cdot \cos^{\varepsilon}(SZE) \qquad (4.3.3)$$

where $N_{e,max}(SZA=0)$ is the peak electron density for $SZA=0$ and $\varepsilon=0.5$ describes ideal Chapman behavior. The fit to the moderate flux peak electron densities is $\varepsilon = 0.44 \pm 0.01$. The M2 peak altitude versus SZA is plotted in Fig. 4.27b. The general trend, an increase in altitude with SZA, is Chapman-like. The M2 peak is higher for high solar activity, indicating a generally warmer atmosphere at 130 km altitude than at solar minimum (Peter et al., 2014).

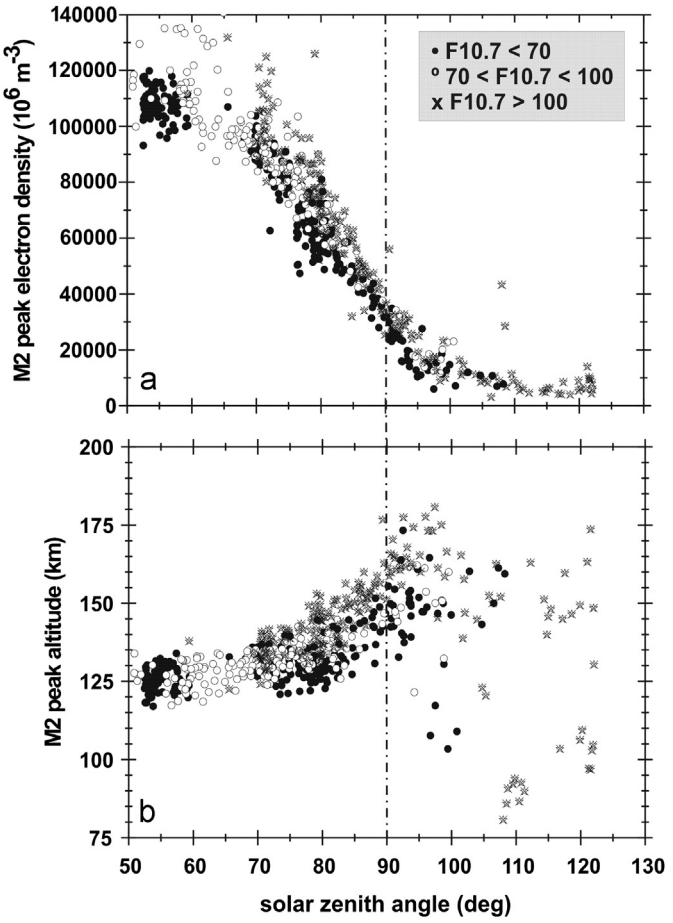

Fig. 4.27. Mars M2 dayside ionospheric peak density (panel a) and altitude (panel b) as a function of solar zenith angle SZA (Peter et al., 2014) distinguished by solar activity expressed by the proxi F10.7.

4.3.7. *Nightside ionosphere*

The normal structure of the nightside ionosphere has been poorly known, with only four electron density profiles from the fully-shadowed nightside (SZA > 105°) ionosphere published prior to the MEX arrival at Mars. Withers et al. (2012b) presented 32 electron density profiles from MaRS with solar zenith angles greater than 105° (Fig. 4.28). These profiles display a wide range of morphologies, altitudes of plasma layers, peak electron densities, and total electron contents. Some profiles are essentially devoid of plasma and have very low peak densities. In contrast, in other profiles at the same solar zenith angle of 121°, the peak density is an order of magnitude greater, exceeding 10^4 cm^{-3}. Such variability in peak density is not seen in the dayside ionosphere and such high densities so far from the terminator are challenging to explain. In other instances, the morphology, peak altitude, and peak density observed on the nightside are very consistent with simulations of ion production by electron precipitation.

These findings indicate that the ion production mechanisms operating on the nightside are much more variable than the photoionization that dominates the dayside. The dominant nightside production mechanisms are thought to be a combination of (i) electron precipitation, (ii) transport of photoionized plasma from the dayside, and (iii) occasional solar energetic particle events and meteoroid ablation events of sufficient energy to dominate the process. Plasma layers occur at altitudes from 80 km to 160 km, without any apparent dependence on solar zenith angle. Whereas electron precipitation produces layers at higher altitudes, solar energetic particle events and meteoroid ablation tend to produce low-altitude layers. Although numerical models are hard-pressed to reproduce the diverse phenomena present in Fig. 4.28, some aspects of the nightside ionosphere appear well-behaved. Total electron contents in the nightside ionosphere are roughly equal to 65 km x the corresponding peak electron densities (Fig. 4.29). This would be quite reasonable if the nightside ionosphere always had the same shape, but a glance at Fig. 4.28 shows that this is not the case. Finally, some profiles clearly possess two distinct plasma layers at 100 km and 160 km, an observation which necessitates separate production mechanisms operating simultaneously, but at different altitudes.

4.3.8. *Simultaneous observations with Mars Global Surveyor*

Despite the long operational lifetimes of both Mars Global Surveyor and Mars Express, the two spacecraft only acquired simultaneous radio occultation observations for a brief period in December 2004 during northern summer (Ls ≈ 128°). Mendillo et al. (2011) examined these two distinct sets of ionospheric observations for 10–14 December 2004 and reproduced them with a numerical model. The 40 profiles from Mars Global Surveyor were acquired at solar zenith angles of 78 – 79°, latitudes of 67 – 68°N, and local times of 4.8 – 4.9 hours, while the 5 profiles from Mars Express were acquired at solar zenith angles of 81 – 85°, latitudes of 36 – 49°S, and local times of 7.8 – 8.2 hours. These concurrent sets of ionospheric measurements, shown in Fig. 4.30, are subject to the same solar radiation, but come from very different regions of the planet. The neutral atmosphere near the summer polar region (MGS observations) is different from the neutral atmosphere at winter mid-latitudes (MEX observations). This fortuitous conjunction of MGS and MEX observations provided an opportunity to distinguish the effects on the ionosphere from solar irradiance and neutral atmospheric conditions (Mendillo et al. , 2011). Using identical neutral atmospheres, the simulations failed to reproduce both sets of observations. Moreover, the requirement to reproduce the M1 layer simultaneously in opposite hemispheres constrained the representation of electron impact ionization, a particularly important process at low altitudes. Incorporating these factors, the model successfully reproduced both sets of observations (Fig. 4.31).

4.3.9. *Meteor layers*

The sensible base of the Martian ionosphere is most often found at an altitude of 80–90 km, where the plasma density in the lower portion of the M1 layer abruptly drops into the noise level. The refractivity also usually changes sign at or slightly below this altitude.

There are instances, however, in which the electron density profile shows excess electron density below the base of the M1 layer (Pätzold et al., 2005). This additional electron density appears as layers, sporadically and locally with respect to Mars surface locations, that persist for at least 24 hours.

Layers of metallic ions (predominantly magnesium and iron) have been observed in the lower Earth ionosphere by in situ rocket soundings (Kopp, 1997). These layers are attributed to the influx of meteoroids into the Earth atmosphere. The meteoroids are heated to a point where their surface ablates, releasing magnesium and iron atoms into the atmosphere that are subsequently ionized.

Two effects are considered to be primarily responsible for the formation of the ionized layer at Mars:

i) Photoionization of the iron and magnesium atoms (Pesnell & Grebowsky, 2000)
ii) Charge exchange of the neutral metal atoms with ionospheric ions (Molina-Cuberos et al., 2003)

Current models of the formation of the ionized meteor layers show that both effects play an important role (Molina-Cuberos et al., 2003).

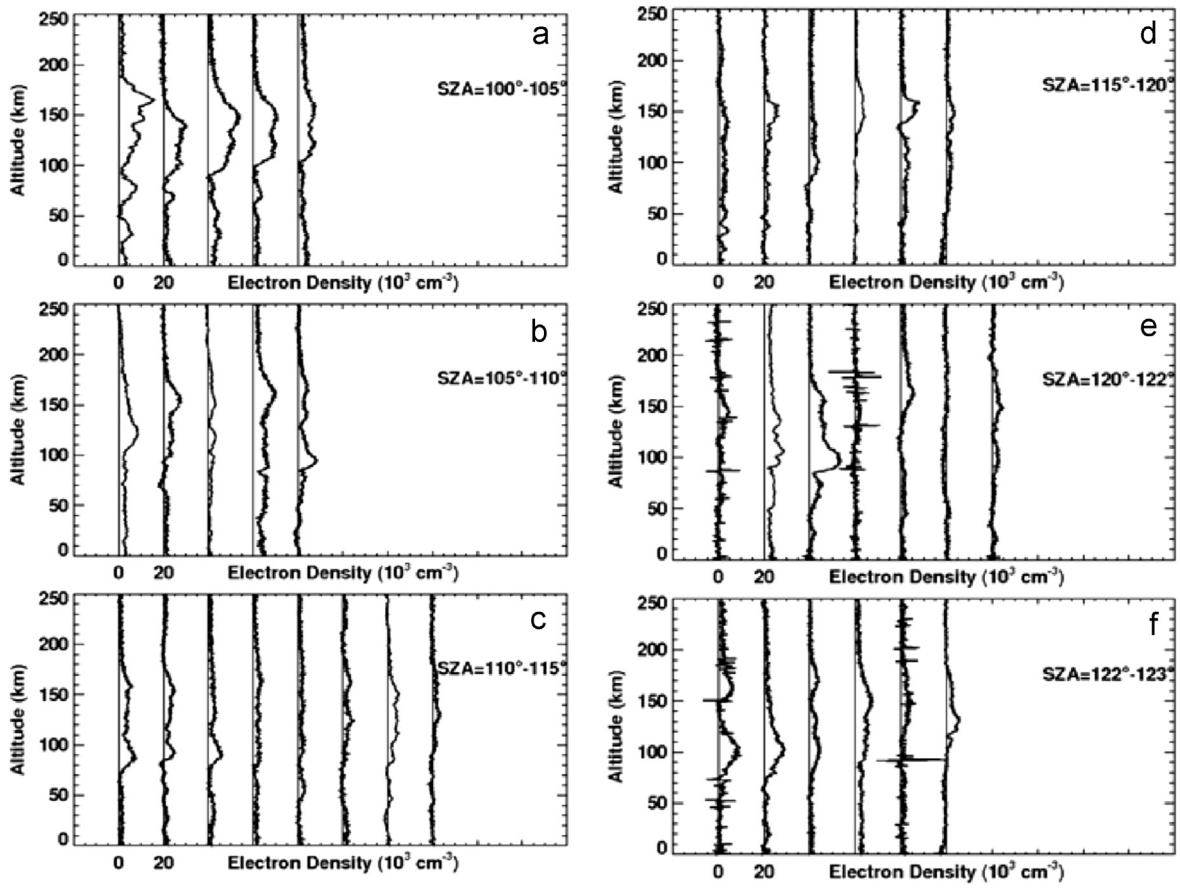

Fig. 4.28. A series of 37 nightside electron density profiles from 18 August to 1 October 2005, ordered according to solar zenith angle SZA The horizontal axis is linear. Each profile in a panel is offset from its neighbor by 2 x 10^4 cm^{-3}. The vertical lines indicate zero electron density for each profile (Withers et al., 2012b).

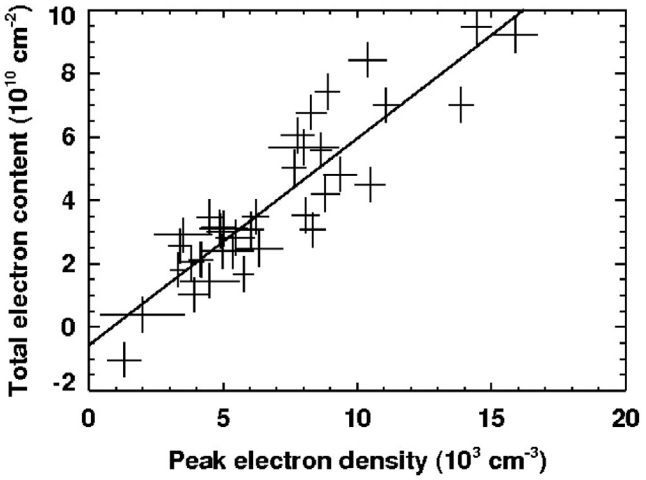

Fig. 4.29. Dependence of the nightside total electron content on the associated peak electron density. Lengths of the horizontal and vertical arms of the crosses indicate uncertainties in peak electron density and total electron content, respectively. The solid line is a best fit to the observations (Withers et al., 2012b).

Although Pätzold et al. (2005) reported on these layers for the first time and have found similar features and examples in the Venus ionosphere (Pätzold et al., 2009b), other examples have been found later in data from past missions (Withers et al., 2013).

4.3.10. *Modeling the ionosphere*

Peter et al. (2014) have developed a one-dimensional photochemical simulator for the lower ionosphere 'IonA' (**Ion**ization in **A**tmospheres) with four observation parameters: solar flux, SZA, Ls, and planetary location. IonA considers:

i) Photoionization of CO_2, N_2 and O by solar radiation occurs within the wavelength range 0.5–95 nm. Actual solar fluxes are provided by SOLAR2000 (Tobiska et al., 2000) for the day of the observation. Absorption and ionization cross sections for 0.5–5 nm are taken from Avakyan et al. (1998), and for 5–95 nm from Schunk & Nagy (2009).
ii) The background neutral atmosphere with temperature and number density profiles at ionospheric altitudes are provided by the Mars Climate Database Version 4.3 (MCD 4.3) (Lewis et al., 1999; Millour et al., 2011).
iii) Secondary ionization is computed with the W-value approach as described in Wedlund et al. (2011).

It is further assumed that

iv) The electron temperature T_e, which is poorly known at ionospheric altitudes, is set equal to the neutral atmospheric temperature T_n, (Hanson & Mantas, 1988; Witasse & Nagy, 2006).
v) Electron production and loss are in equilibrium
vi) Dissociative recombination of O_2^+, which is the overwhelmingly dominant ion in the ionospheric main peak (Schunk & Nagy, 2009), is the only loss process with the rate

$$\alpha_{O_2^+} = 2.4 \cdot 10^{-7} \left(\frac{300}{T_e}\right)^{0.7} \cdot 10^{-6} \frac{m^3}{s} \quad (4.3.4)$$

Comparing the observations with the model (Fig. 4.32), it was found that secondary ionization is responsible for most of the

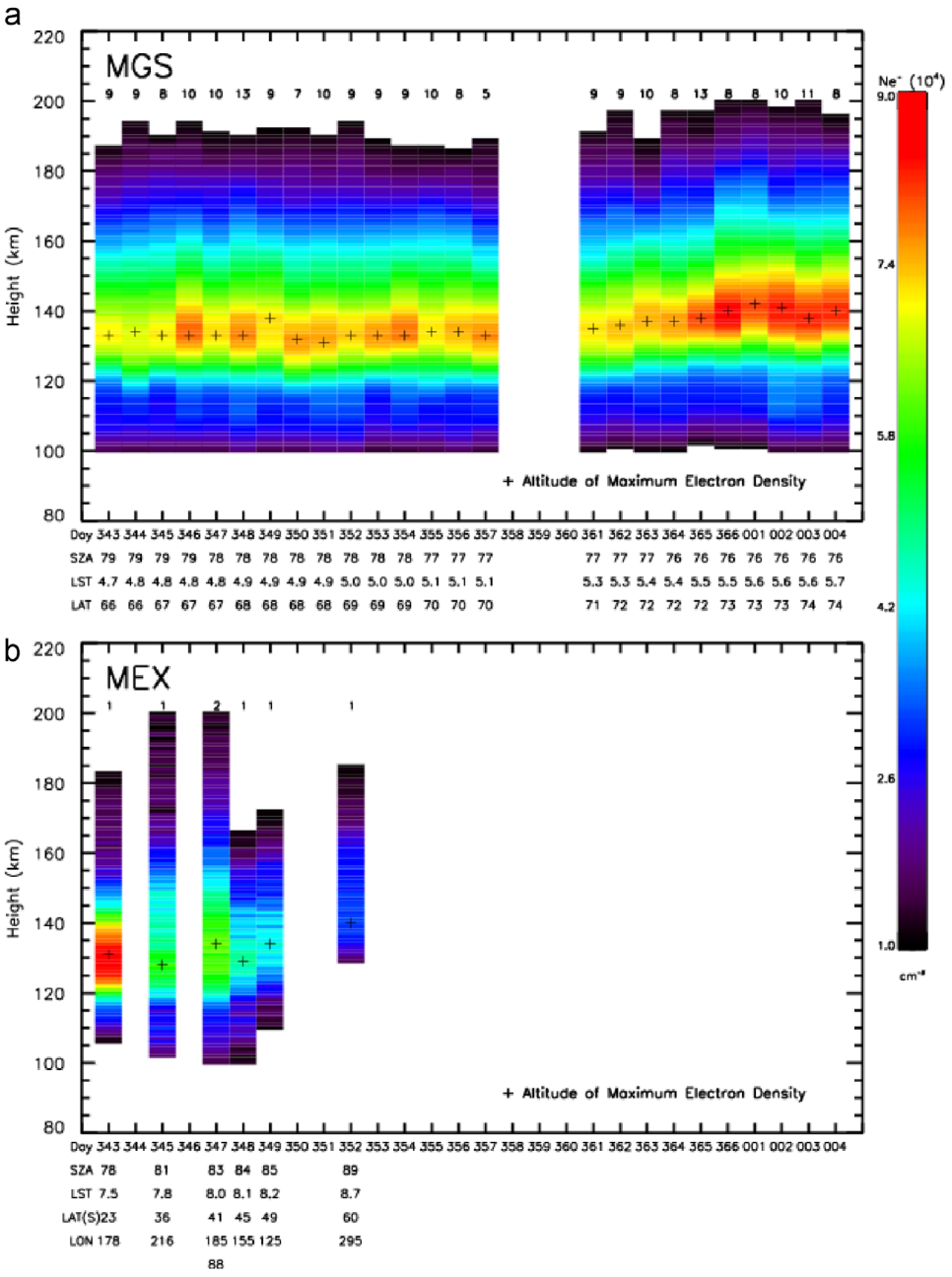

Fig. 4.30. Vertical profiles of electron density from 8 December 2004 (DOY 343) to 4 January 2005 (DOY 004) for MGS (Panel a) and MEX (Panel b). Each strip shows an average of all profiles from a given day, with the number of profiles per day shown above the strip. Day of year, solar zenith angle (degrees), local solar time (hours), and latitude (degrees) are indicated. For MEX, longitudes are also indicated. Day of year 347 is the only day with more than one MEX profile (Mendillo et al., 2011).

electron density in M1, while the M2 layer is primarily formed by photoionization.

The MCD v4.3 provides eight scenarios for the state of the Mars atmosphere, ranging from a cool/clear atmosphere at solar minimum activity with low dust content, up to a warm/dusty atmosphere at solar maximum activity. The peak electron density and peak altitude of the M2 layer for the cool/clear and warm/dusty MCD scenarios are shown in Fig. 4.33 in comparison with the observations.

The simulated peak density and altitude generally agree well with observations for a cool atmosphere at solar minimum (Fig. 4.33a,c). The background neutral atmosphere could be even slightly cooler than predicted by the MCD v4.3 scenario when comparing the peak width with the observations (see Peter et al., 2014). Some individual profiles may be better modeled with a warmer background atmosphere, but, on the average, the MEX mission encountered a cool atmosphere for the majority of the MaRS observations.

In contrast, using a warm background atmosphere at solar maximum, the combined simulated peak density and altitude do not provide an adequate representation of the observations. The higher temperature forces the atmosphere to expand and the maximum of ion/electron production by photoionization occurs at higher altitudes. As a result, the simulated peak altitudes disagree strongly with the observations (Fig. 4.33b,d). Peter et al. (2014) have further shown that the width of the M2 layer is much broader for a warm atmosphere, in disagreement with the observations. The broader layer also increases the vertical electron content although the M2 peak density is smaller. The conclusion is that the vertical electron content is dominantly defined by the M2

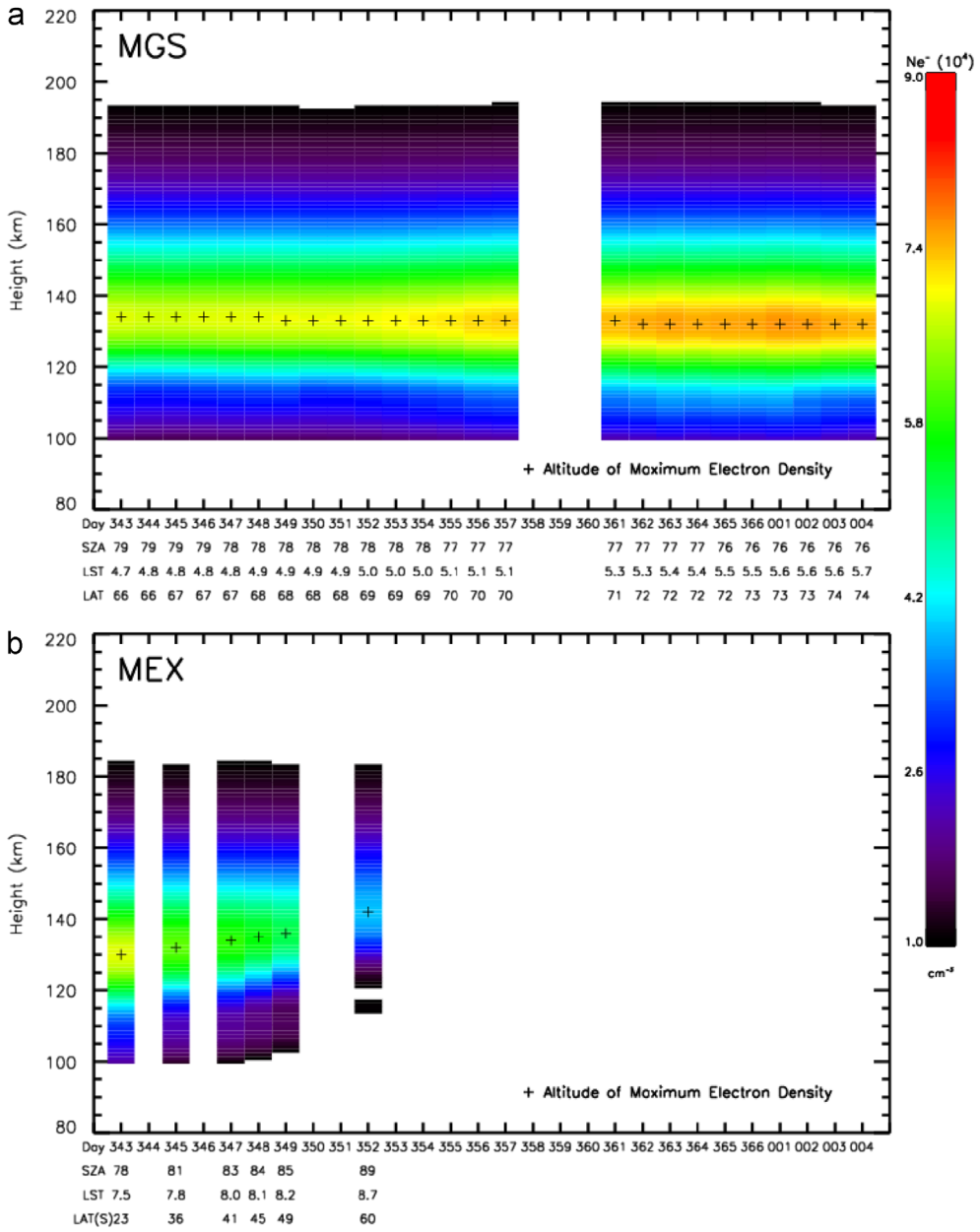

Fig. 4.31. Same as Fig. 4.30, but now showing simulated, not observed, electron densities (Mendillo et al., 2011).

layer and contributions from above and below the M2 layer are insignificant.

4.3.11. Comparison with MARSIS ionospheric soundings

The Mars Advanced Radar for Subsurface and Ionospheric Sounding (MARSIS) is the radar sounder on board of Mars Express. It operates in the subsurface mode to probe below the Martian surface and in the ionospheric mode to sound the topside ionosphere. The ionospheric mode uses frequencies between 0.1 MHz and 5.5 MHz (Picardi et al., 2004). MARSIS is not able, however, to sound the ionosphere below the M2 peak altitude. MARSIS soundings yield thousands of topside electron density profiles along a wide range of SZA.

Morgan et al. (2008) compared the topside profiles with MGS and MaRS full electron density profiles from radio occultation. They complemented the topside electron density distribution by a Chapman fit which, however, can only guesstimate the lower part of M2. The M1 layer could not be reveiled. The comparison of MARSIS electron density profiles with MaRS for altitudes above M1 is in good agreement taken the different times and locations of the observations.

Sanchez-Cano et al. (2013) developed an empirical model of the dayside ionosphere based on MARSIS topside ionospheric electron density profiles and compared them with full MaRS profiles. The agreement with some MaRs seem to be very good although it is not clear to us how the model generates the M1 layer based on photochemical equilibrium at such high precision when compared with MaRS. It is clear from the model by Peter et al. (2014) that the M1 layer is formed dominantely by secondary ionisation.

5. Bistatic radar

5.1. Principles, method, and coverage

In a conventional bistatic radar (BSR) experiment, the spacecraft high-gain antenna (HGA) illuminates the target surface with a right-circularly polarized (RCP) wave incident at the specular

(mirror-like) angle (Fig. 5.1). The reflected signal is captured by Earth-based receivers with RCP and left-circular polarization (LCP). Dielectric constant of the surface material may be derived from the ratio of RCP to LCP echo powers using the Fresnel reflection coefficients and knowledge of the specular angle, which varies during the course of an experiment because of spacecraft motion. Density of the surface material may then be derived after invoking models of physical processes (*e.g.*, Campbell and Ulrichs, 1969). Doppler dispersion of the echo (in either polarization) may be used to estimate rms slopes on the reflecting surface if the HGA illuminates a sufficiently wide swath. 'Non-conventional' experiments include those in which the spacecraft illuminates a single point on the surface ('spotlight' mode) and 'uplink' BSR in which an Earth-based transmitter provides illumination and reception is on the spacecraft. For more details on these and other BSR topics, see Simpson (1993).

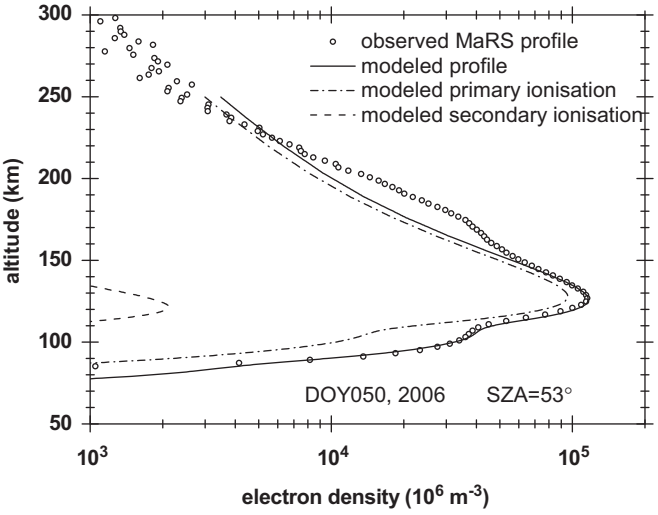

Fig. 4.32. Comparison of the observed (open circles) and modeled electron density (solid line) of 2006 DOY 50 with a zenith angle SZA = 53.0°, longitude = 206.0°, latitude = 37.8°. The modelled electron density profiles by IonA are shown by the solid line for the total profile, by the dash-dotted line for the primary ionization alone and by the dashed line for the secondary ionization. (Peter et al., 2014).

Mars Express executed 70 BSR experiments between 2004 and 2012 (Table A1 in Appendix A). Of the 70 experiments, 23 were conducted with the spacecraft high-gain antenna (HGA) attitude fixed in inertial space while Mars drifted through its radiation pattern (HGA=I in Table A1): during this 'drift scan', a small area on the surface was probed under conditions of specular reflection. The remaining 47 observations were 'conventional' — the HGA beam followed the moving specular point over intervals of 30–90 minutes (HGA=S). Maintaining the specular geometry typically yielded hundreds of independent observations along surface arcs of thousands of kilometers while 'inertial' pointing yielded only a handful of measurements (sometimes only one).

5.2. Results

Signals reflected from Mars' surface were received on the ground by NASA Deep Space Network (DSN) 70-m antennas. S-RCP, S-LCP, X-RCP, and X-LCP signals were recorded using DSN Radio Science Receivers (RSRs). The results of these observations have been reported in conference presentations and journal publications—*e.g.*, Simpson et al. (2011). It is important to note that the surface of Mars — on the horizontal and vertical scales to which centimeter-wavelength BSR is sensitive—is very heterogeneous; as the coverage of this type of observation is very sparse compared with mapping instruments (Fig. 5.2), practically every data point provides new information on the degree of roughness (where available) and density of Mars' surface. It is also important to note that the measurements apply to depths of a few tenths of the radio wavelength in the surface material — that is, the top centimeter at X-band and a few centimeters at S-band — and perhaps 100 wavelengths horizontally, albeit averaged over hundreds of km^2 by the HGA illumination. Surface permittivity ranges from less than 1.5 (very dusty, or low density soil) to over 6 (dry solid rock). The

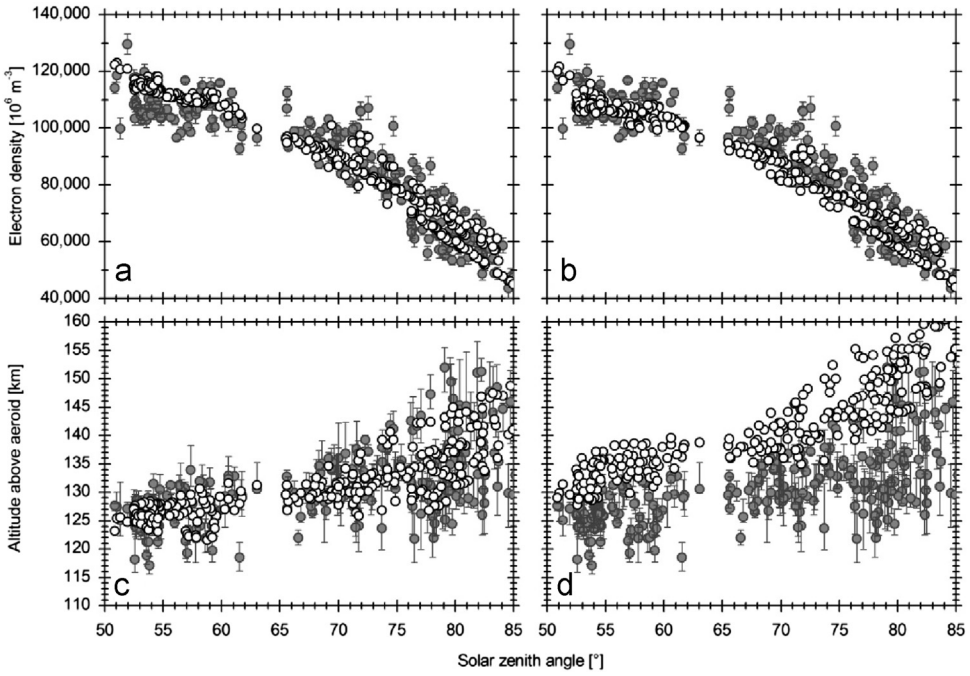

Fig. 4.33. Simulated M2 peak electron density (upper panels) and M2 peak altitude (lower panels) as open circles compared with the observations (gray circles with error bars) for a cool atmosphere at solar minimum taken from MCD v4.3 (a,c) and for a warm and dusty atmosphere at solar maximum (b,d) (Peter et al., 2014).

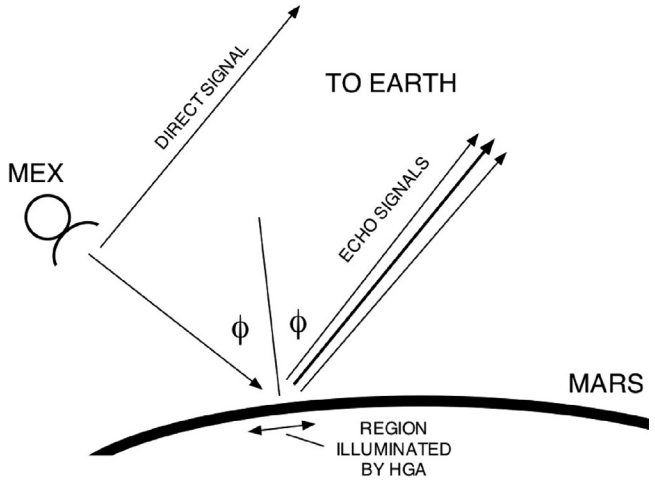

Fig. 5.1. 'Downlink' bistatic radar in which the spacecraft high-gain antenna illuminates parts of the target surface at specular angle ϕ and the echo is received on Earth. The finite HGA beamwidth yields many echoes from surface 'facets' properly oriented for mirror-like reflection surrounding the specular point for the mean spherical surface. Each facet reflects at a Doppler shift which depends on its position and velocity relative to the spacecraft.

HGA radiation pattern controls echo spectrum shape for surfaces with rms slopes larger than about 2°; only the roughness of smoother surfaces can be reliably measured using MEX BSR.

Early results, based on a Doppler sorting algorithm applied to data collected with inertial pointing, showed that gradations in dielectric constant could be detected on horizontal scales of tens of km (Simpson et al., 2006b). The same inertial pointing observations also confirmed that dielectric constants observed at the longer, 13 cm wavelength were greater than those observed at 3.6 cm, as would be expected from the deeper penetration of those waves to more compacted material.

There are exceptions to the expected variation with wavelength, however. These were first detected in northern plains, where the shorter wavelength yielded larger dielectric constants at single locations (Simpson et al., 2006a). or duricrust surface cap over a lower layer of less conso/or duricrust surface cap over a lower layer of less consolidated material at these sites. The most recent observations of specular reflections show long arcs in the *southern* hemisphere where the wavelength 'inversion' is also seen (Fig. 5.3). These observations are still being evaluated.

MEX BSR also provided a surprise by detecting extremely smooth areas near the martian poles. Power spectra of specular

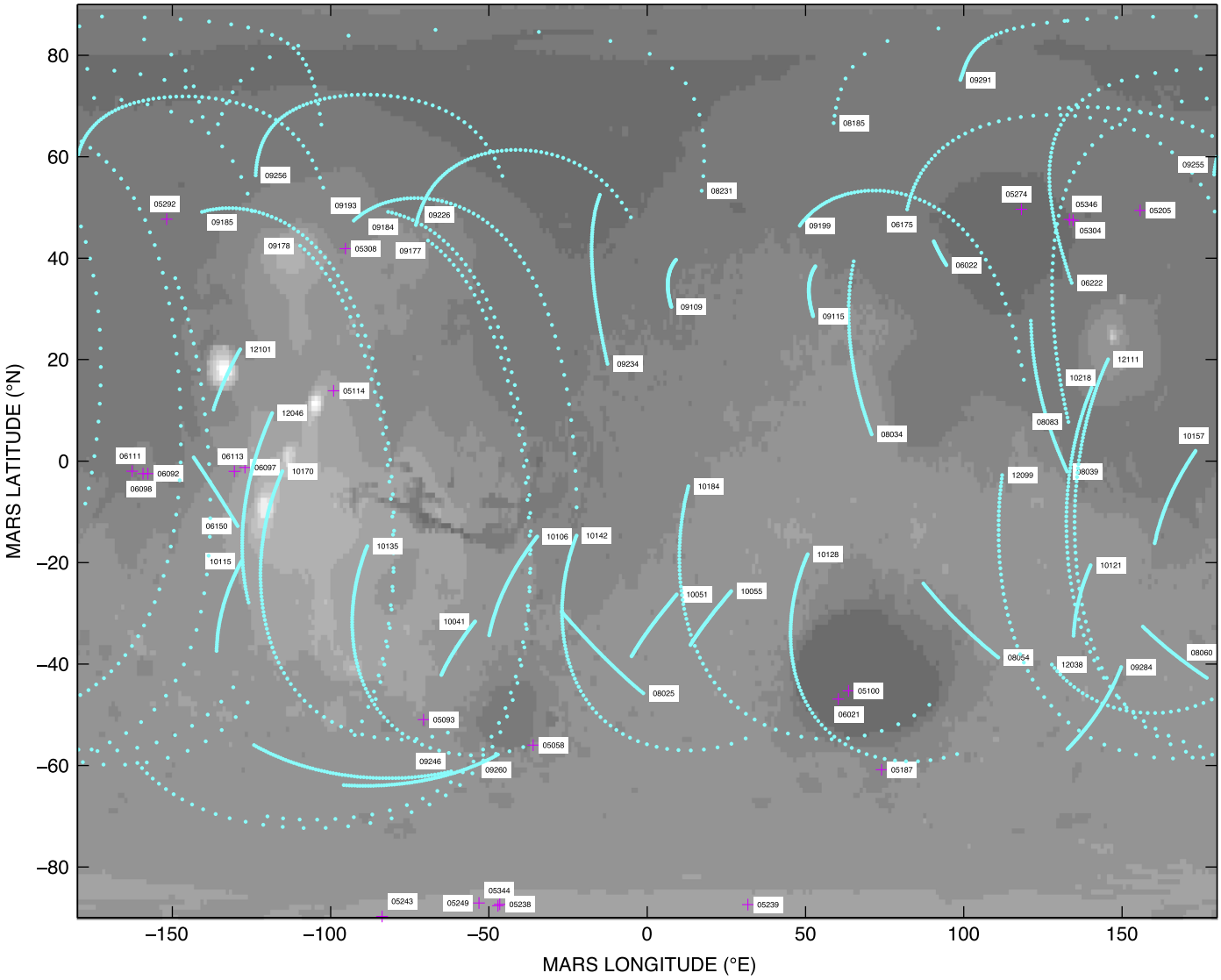

Fig. 5.2. Coverage of MEX BSR over 2005-2012. Red crosses denote inertial pointing targets on the surface; blue dots show specular point tracks at 60-second time resolution. Five-digit labels (YYDDD) give year and day-of-year of the experiment. Background is provided by an early low-resolution Mars Global Surveyor MOLA topographic map (Smith, 1999).

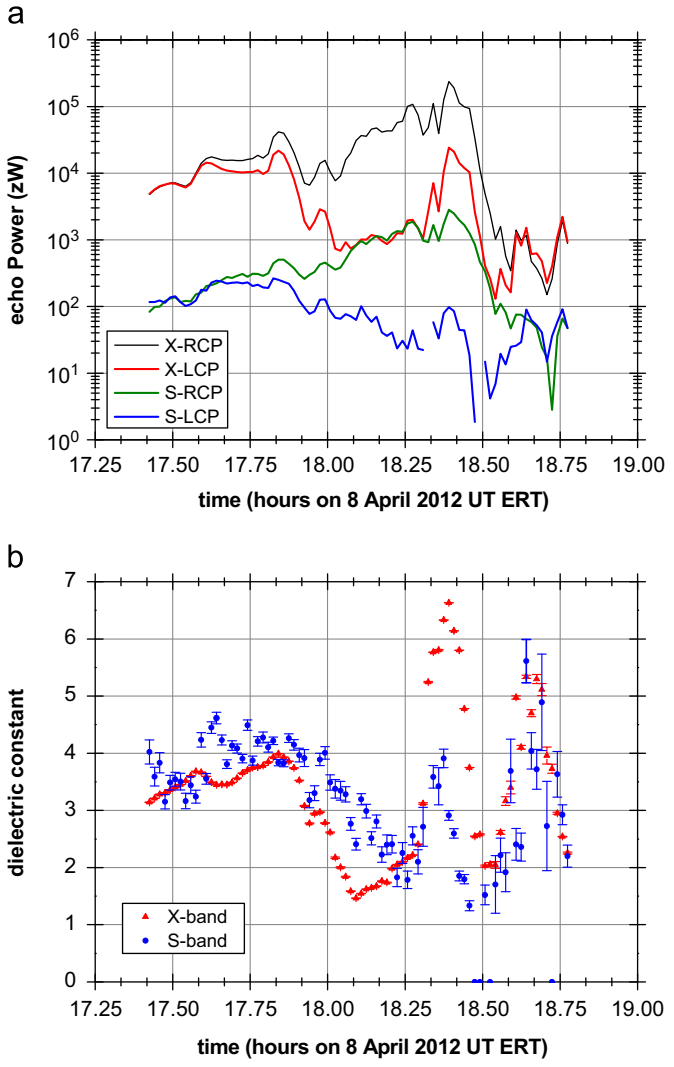

Fig. 5.3. Echo powers (panel a) and dielectric constant ε (panel b) estimates at 13 cm (S) and 3.6 cm (X) wavelengths from 8 April 2012 ('12099' in Fig. 5.2, starting just south of the equator at 112° E). Echo powers for RCP (SR and XR) and LCP (SL and XL) show many of the same features (*e.g.*, local peaks near 17.85 h and 18.4h); where they are approximately equal (near 17.6 h and 18.6 h), we infer a Brewster angle. Dielectric constant estimates become unreliable when either RCP or LCP power is less than 20 zW. Before 18.2 h $\varepsilon_s > \varepsilon_x$, as expected for nominal regolith, over 18.3-18.5 $\varepsilon_s < \varepsilon_x$ implying a one centimeter overlying lag gravel or duricrust layer, and after 18.5 h $\varepsilon_s \sim \varepsilon_x$, suggesting a regolith with uniform density over the top several centimeters.

surface echoes in polar regions are punctuated by narrow spikes indicating presence of isolated, very smooth areas. These extend over several hundreds of km^2 and have rms surface roughness on the order of 0.17° (Simpson et al., 2009). The inferred roughness is comparable to that of a quiet pond on a nearly windless day. This phenomenon is seen in both the northern and southern polar regions and is not yet understood.

An ongoing investigation involves characterization of the surface west of Tharsis at low southern latitudes (also known as Medusae Fossae and 'Stealth'). This region is essentially invisible in Earth-based radar images of Mars (Muhleman et al., 1991) and appears to MARSIS and SHARAD — the orbiting MHz sounding radars on Mars Express and Mars Reconnaissance Orbiter, respectively — to be blanketed with hundreds of meters of low-density ash or an equivalent material (Watters et al., 2007; Carter et al., 2009). MEX BSR has detected obliquely reflected echoes, although these are extremely weak. An early conclusion—*i.e.*, that 'Stealth' is very rough on scales comparable to the radar wavelengths but not on smaller scales (Simpson et al., 2006c)—is subject to new results from pending analysis of observations collected in 2012, such as those shown in Fig. 5.3.

Fig. 5.3a shows echo power as a function of time from an experiment in which the ground track sampled a wide range of (mostly) southern hemisphere terrains. The track began just south of the equator at 112° E longitude ('12099' in Fig. 5.2), reached 58° S just before crossing ±180° longitude, and ended at (35.1° N, 148.6° E) after crossing Stealth. Incidence angle was 60.4° at the beginning, peaked at 83.5° (18.32 h), and ended at 55.9°. Slant range to the specular point was minimum (1080 km) at 22°S, where the HGA footprint was both smallest and moving most quickly.

Fig. 5.3b shows the dielectric constant at both S- and X-bands, derived from the echo powers in Fig. 5.3a and the Fresnel reflection coefficients. Before 18.2 h, dielectric constant is larger at the longer wavelength, consistent with its deeper penetration to more consolidated material. Both dielectric constants trend slowly upward to about $\varepsilon = 4$ at 25° S latitude, then begin to decrease as the specular point moves farther south. As the ground track moves northward again, the echo powers reach their maximum values and dielectric constant at X-Band overtakes the value at S-band, reaching $\varepsilon_x > 6$ over 30–40° S.

Over Stealth (18.52 ± 0.02 h), the S-LCP echoes become too weak for reliable recovery of S-band dielectric constant; the X-band values are $\varepsilon_x \sim 2.05 \pm 0.05$. As the specular point moves to northern latitudes, dielectric constant rises to $\varepsilon \sim 5$, then finally drops below 3 at the end; over this region the S- and X-band behaviors are similar.

5.3. Interpretations

Although bistatic radar studies of Mars have been conducted for over 40 years, emphasis in the past has been on inference of centimeter-to-meter scale surface roughness, a quantity which is difficult to extract when the echo spectral shape is controlled by the HGA illumination, as is the case for MEX. Instead, the emphasis in MEX BSR has been on dual-polarization echo power and its interpretation in terms of Fresnel reflectivity and surface dielectric constant (measured simultaneously at two wavelengths). Near-equatorial Earth-based radar studies of Mars from the 1970s are available, but they have their own limitations. As a result, there are few existing data sets suitable for comparison. Internal comparisons of MEX BSR data, where ground tracks cross, show dielectric constant agreements to about 20%; but an effort is underway to improve the calibrations and reduce the crossover differentials. In polar regions, where very smooth surfaces have been detected using BSR, systematic comparisons with other data, such as from vertical sounding at MHz frequencies (MARSIS and SHARAD) and imaging, is planned; but no correlations have been identified to date.

6. Gravity observations

6.1. Principles, method and coverage

The eccentric orbit of Mars Express allowed several distinct gravity experiments:

i) Targeted gravity observations of the asymmetric gravity field obtained along the trajectory over interesting topographic features (volcanoes, grabens). These opportunities occur during pericenter passes (altitudes 100 km < h < 250 km) and are used to determine the local crustal structure (Beuthe et al., 2006, 2012)

ii) Global gravity observations obtained from spacecraft tracking for typically ±1.5 hours about the apocenter position of its orbit. These data are used for an improvement of the Mars ephemeris, the reconstruction of the MEX orbit (Rosenblatt et al., 2008; Fienga et al., 2009) and an attempt to extract the temporal behavior of the low degree and order gravity field coefficients.

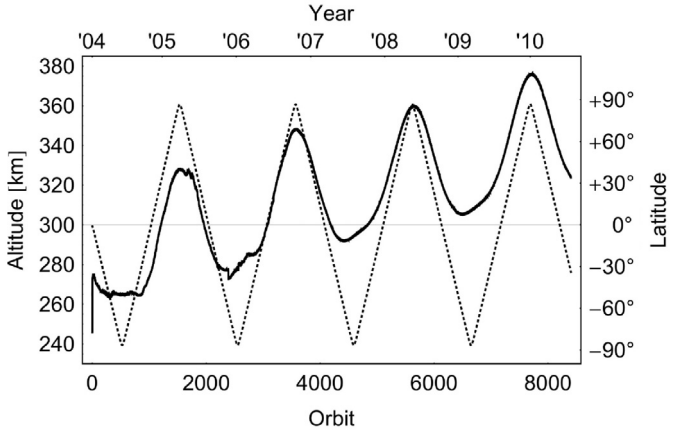

Fig. 6.1. Altitude (solid curve) and latitude (dotted curve) of the pericenter of Mars Express in terms of the orbit number and date (beginning of each year) (Beuthe et al., 2012).

iii) Phobos close flyby with the objective to improve the knowledge of mass, density and gravity field of Phobos. Several close flybys were performed (Witasse et al., 2014): at 470 km in 2006; at 275 km in 2008; at 72 km in 2010 (Andert et al., 2010; Pätzold et al., 2014a).

6.2. Target gravity

When Mars Express began its observations from orbit, its 270 km pericenter altitude was 100 km lower than previous Martian orbiters during their mapping phases (Mars Global Surveyor and Mars Odyssey did temporarily reach lower altitudes during transition phases). The low pericenter altitude of Mars Express implied a greater sensitivity to short-wavelength gravity anomalies because the effect of gravity anomalies on the probe decreases as a power law with altitude and anomaly wavenumber (Jekeli, 2007). The very eccentric orbit however limited high-quality gravity observations to a small window about pericenter, thus leading to the concept of target gravity experiments. In essence, target gravity experiments consist in measuring short wavelength velocity perturbations when the spacecraft is above a target of geophysical interest at the pericenter of its orbit. The velocity perturbation of the spacecraft is measured by means of radio signal Doppler shifts along the line-of-sight between the spacecraft and the Earth. Short wavelengths are defined here as smaller than the 426 km wavelength associated with harmonic degree $l=50$, which is also the maximum degree of the field (or wavelength cutoff) used in the orbit reconstruction. The

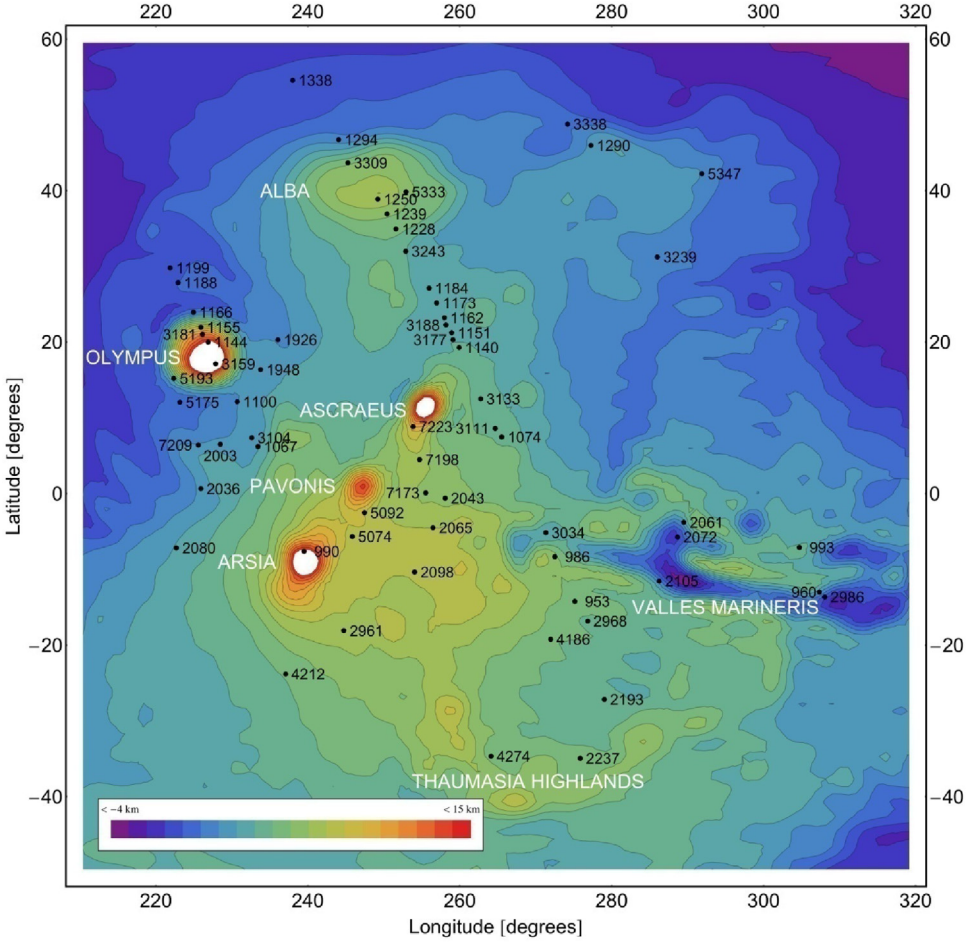

Fig. 6.2. Pericenters of gravity passes (designated by orbit numbers) observed with MEX-MaRS in the Tharsis province, superimposed on the topography (Beuthe et al., 2012).

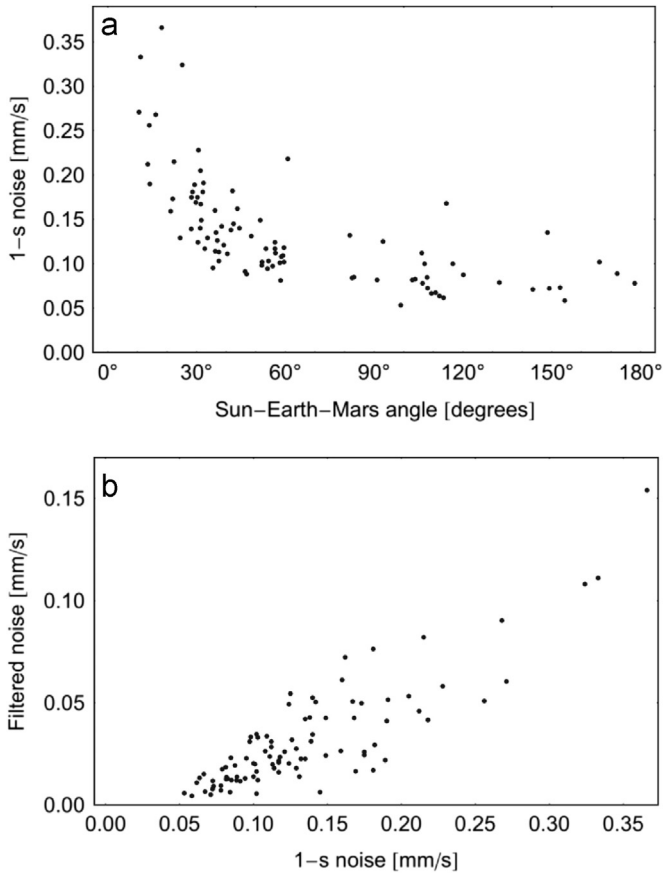

Fig. 6.3. (a). Velocity residual noise (1-s sampling time) versus Sun-Earth- Mars angle. (b) Filtered velocity residual noise (frequency cutoff: 1/70 Hz) versus noise at 1-s sampling time (Beuthe et al., 2012).

comparison of Mars Express data taken in 2004-2005 with the best global gravity field available in 2005 demonstrated a good agreement up to a wavelength of 290 km, i.e. harmonic degree l=73 (Beuthe et al, 2006).

Anomalies of short wavelength are mainly due to variations in the density of the crust. Thus target gravity experiments mainly provide constraints on the density of the crust in the target area. In practice, each target must be observed several times and data must be combined in order to decrease the noise to an acceptable level. Repeated observations are possible over a limited time frame because of the near-resonant orbit of Mars Express. For example, the Mars Express spacecraft was doing approximately 11 revolutions in 3 Martian days from 2004 to 2007, meaning that neighboring pericenter passes were performed every 11 orbits with a shift of about one degree of longitude (at the equator) and two degrees of latitude (the latter shift is due to the gravity effect of Mars' oblateness). All in all, it was possible to make a cluster of observations at a given target close to the equator roughly every 1000 orbits. Unfortunately, the sensitivity to gravity anomalies decreased significantly during the mission because of the increasing pericenter altitude (see Fig. 6.1), leading to a 50% decrease of the short-wavelength gravity perturbation at pericenter. Another constraint on the planning of gravity experiments is the timing of solar conjunctions, which cause a degradation of the Doppler signal (see below). Fig. 6.2 shows a map of target gravity passes in the Tharsis Province.

Observed X-band Doppler shifts are measured at one sample per second in coherent two-way mode. They are reduced to Doppler residuals (and then transformed into line-of-sight velocity residuals) by subtracting the Doppler shift associated with the reconstructed orbit of Mars Express provided by the European Space Operation Center (ESOC). Since ESOC reconstructs the orbit with respect to the global gravity field JGM85F02 up to degree and order 50, velocity residuals do not include contributions due to gravity harmonics of higher degree (differences between the field JGM85F02 and the most recent global gravity field are insignificant below degree 50). Characteristics and examples of gravity data are described in Beuthe et al. (2006), Pätzold et al. (2009a) and Beuthe et al. (2012).

The noise level varies significantly between gravity passes. The mean velocity noise of a profile is defined as the average of the velocity noise over the high altitude part of the profile (above 600 km, where short-wavelength gravity anomalies have a negligible effect). The mean velocity noise for the original 1-s sampling varies between 0.05 and 0.37 mm/s with an average of 0.13 mm/s (see Fig. 6.3a) depending on the SME angle. The average noise for Mars Express velocity residuals is 0.051 mm/s at a 10-s sampling time, which compares well with the average data noise of 0.053, 0.056 and 0.040 mm/s for Mars Reconnaissance Orbiter, Mars Global Surveyor and Mars Odyssey, respectively (Konopliv et al., 2011). Fig. 6.3a shows that the noise increases significantly above the average for Sun-Earth-Mars angles less than 30° because of perturbations due to the solar corona and the inner solar wind. For this reason, only a few target gravity experiments occurred close to a solar conjunction (SME < 10°). The contribution of solar plasma to the total noise is discussed by Pätzold et al. (2009a) for three apocenter gravity experiments.

At a 1-s sampling time, the signal due to short-wavelength gravity anomalies is drowned by the noise. Since gravity experiments are not sensitive to wavelengths shorter than the pericenter altitude (say 280 km), nothing is lost by excluding shorter wavelengths. The signal is thus filtered with a cutoff frequency equal to 1/70 Hz. This choice of cutoff can be understood by noting that Mars Express covers approximately 280 km on the ground in 70 s at pericenter. As the noise of the Mars Express velocity residuals scales approximately as $\Delta t^{-0.4}$ (Δt being the sampling time), the noise is typically reduced by a factor $(70/2)^{-0.4} \approx 4$, though the reduction factor varies between profiles (see Fig. 6.3b). Filtered velocity residuals are differentiated into acceleration residuals which can be compared to predicted accelerations from geophysical models. The pericenter pass consists of acceleration residuals uniformly resampled along a 4096 km groundtrack centered on the pericenter, with a maximum altitude between 500 and 600 km.

Gravity data are fitted with an admittance approach, which consists in analyzing the linear transfer function between gravity and topography in the Fourier domain. The advantages of this method are the elimination of the uncorrelated noise and the treatment of the different wavelengths on an equal footing. The (observed) coherence and (observed) gain factor between the observed acceleration and the corresponding acceleration predicted by the surface topography are defined. The observed coherence should be close to unity otherwise the admittance approach does not yield meaningful results. The (predicted) coherence and (predicted) gain factor for the acceleration predicted for each geophysical model are defined similarly. All these quantities are computed with the 1D multi-taper method using seven tapers (see Fig. 6.4; more details are given in Beuthe et al., 2012). The geophysical model describes the topography as a top load of given density deflecting a thin lithosphere of given elasticity. Additional support may be present in the form of bottom loading (more details in Beuthe et al., 2012). The elasticity of the lithosphere, however, has little influence on the short-wavelength gravity perturbations considered here.

Target gravity experiments were performed in sufficient numbers for geophysical analysis at three targets in the Tharsis

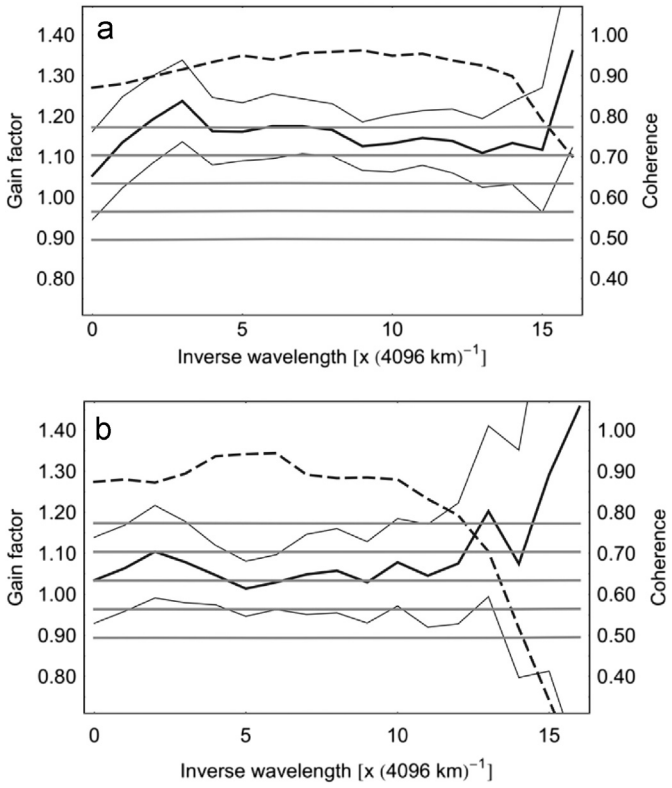

Fig. 6.4. Spectral analysis of the acceleration residual ($l > 50$) for the pericenter passes of (a) orbit 1144 above Olympus Mons and (b) orbit 7173 above Ascraeus Mons: observed gain factor (thick curve), 1-sigma errors (thin curves), coherence (dashed curve). The predicted gain factor (horizontal gray lines) varies with the density in the range 2.6-3.4 g/cm3 (bottom to top) with an increment of 0.2 g/cm3. The elastic thickness is set at 80 km and there is no bottom loading.

Province: Olympus Mons (17 passes), Ascraeus Mons (15 passes) and Valles Marineris (8 passes). The surface density in each target area was estimated as follows. First the best-fitting load density was determined for each pericenter pass by adjusting the predicted gain factor to the observed gain factor. Next the load density in the target area was estimated by averaging the best-fitting load densities of the different passes, with an uncertainty given by the square root of the weighted variance. In absence of bottom loading, the load density is highest at Olympus Mons (3 g/cm^3), a bit lower at Ascraeus Mons (2.9 g/cm^3) and lowest at Valles Marineris (2.6 g/cm^3). The presence of bottom loading shifts the density estimates to slightly higher values at Olympus Mons and Ascraeus Mons (3.1 g/cm^3) and to significantly higher values at Valles Marineris (2.9 g/cm^3). The rather high estimates of the volcanic density, compatible with those obtained from accelerations predicted with the global gravity field based on Mars Reconnaissance Orbiter data, suggest that the lava is of basaltic type (Beuthe et al., 2012). The conclusion that Tharsis volcanic shields are mainly built with high density lava also agrees with the high density of Martian meteorites which are thought to originate in the Tharsis Province.

Besides estimating the load density, the dependence of the average gain factor on the wavelength cutoff was analyzed. The gain factor at Ascraeus Mons is higher when the cutoff wavenumber is smaller (harmonic degree $l=30$ instead of $l=50$). This effect can be attributed to a variation of the load density with the scale of analysis: a small structure (400 km wavelength) of lower density is enclosed within a larger structure of high density. Given the conical shape of the volcano, the most obvious interpretation of these results is that the top of Ascraeus Mons was formed with andesitic lava of lower density whereas the lower part of the shield is made of basaltic lava of higher density. This hypothesis is also supported by 2D localized admittance modeling of the global gravity field at Ascraeus Mons. The other large volcanoes (Olympus, Pavonis and Arsia), however, do not exhibit a top of lower density (Beuthe et al., 2012). Ascraeus Mons thus seems to have had another construction history, maybe due to a later date of formation in comparison with the other Tharsis Montes.

At Valles Marineris, the influence of the wavelength cutoff on the gain factor can be attributed to bottom loading, for example in the form of intruding mafic dikes radiating from the center of Tharsis. Subsurface magmatic intrusions are likely as dikes have already been identified within the canyon walls. Bottom loading also favors a higher value for the surface load density at Valles Marineris (2.9 g/cm^3 instead of 2.6 g/cm^3), which is more in line with neighboring rocks of basaltic composition. Flood basalts are indeed strong candidates to explain the origin of the layering seen in the cliffs of Valles Marineris.

6.3. *Global gravity: precise reconstruction of Mars Express trajectory*

The MEX orbit is very eccentric with a low-altitude pericenter, allowing to obtain information on the Mars static gravity field at small spatial scales over targets of geophysical interest (Beuthe et al., 2006, 2012, see also previous section). Knowing the orbit to high precision can also give constraints on the temporal variations of the gravity field at longer scales, for example due to the atmospheric CO_2 seasonal cycle and the solid-tides raised by the Sun inside Mars (e.g. Rosenblatt and Dehant, 2010). Moreover, measuring precisely the secular drift of the orbit constrains the mass of the Martian moons. The fine signature of these gravity signals on the spacecraft trajectory depends on the semi-major axis, the inclination and the eccentricity of its orbit (e.g. Kaula, 1966). The Mars variable gravity is at the limit of detection from the Mars Global Surveyor (MGS) and Mars Odyssey (ODY) orbits (Konopliv et al., 2006; Marty et al., 2009). The semi-major axis of the MEX elliptical orbit is about three times larger than the semi-major axis of the nearly circular MGS/ODY orbits. The variable gravity signal on the MEX orbit is thus weaker than on the MGS/ODY orbits, so that the MEX orbit must be known to higher precision than the MGS/ODY orbits in order to detect it. The precision on the MEX orbit is thus required to be better than a few meters, which is the current precision on the MGS/ODY orbits. On the other hand, the larger semi-major axis of the MEX orbit has the advantage of making it more sensitive than MGS/ODY to the gravitational attraction of the Martian moons, which generate a small secular drift of the orbit even at distances much larger than those occurring during flyby events. Finally, accurate spacecraft positioning can also improve the determination of the Martian moon ephemerides computed from images taken by the onboard camera (Thuillot et al., 2012).

The MEX navigation orbit computed by the Flight Dynamics (FD) team of the European Space Operation Center (ESOC) is not sufficiently precise to extract the small orbital perturbations (either periodic or secular) of the MEX trajectory. Significant efforts have thus been taken to improve the precision of the MEX navigation. A precise orbit determination of the MEX spacecraft has been performed using dedicated orbitography software named GINS (Géodésie par Intégrations Numériques Simultanées) developed by the French Space Agency CNES (GRGS team, 2012; Marty et al., 2009) and further adapted for planetary geodesy applications at the Royal Observatory of Belgium (ROB). This software has been successfully used to compute data-arcs of MGS and ODY orbits with a precision at the 1-meter level (Marty et al., 2009), which is comparable with the precision obtained with the JPL/NASA orbitography software (DPODP, Moyer, 1971; Konopliv et al., 2006) or the NASA/GSFC orbitography software (GEODYN/SOLVE, Pavlis et al., 2001, 2006; Lemoine et al., 2001). The first step of the

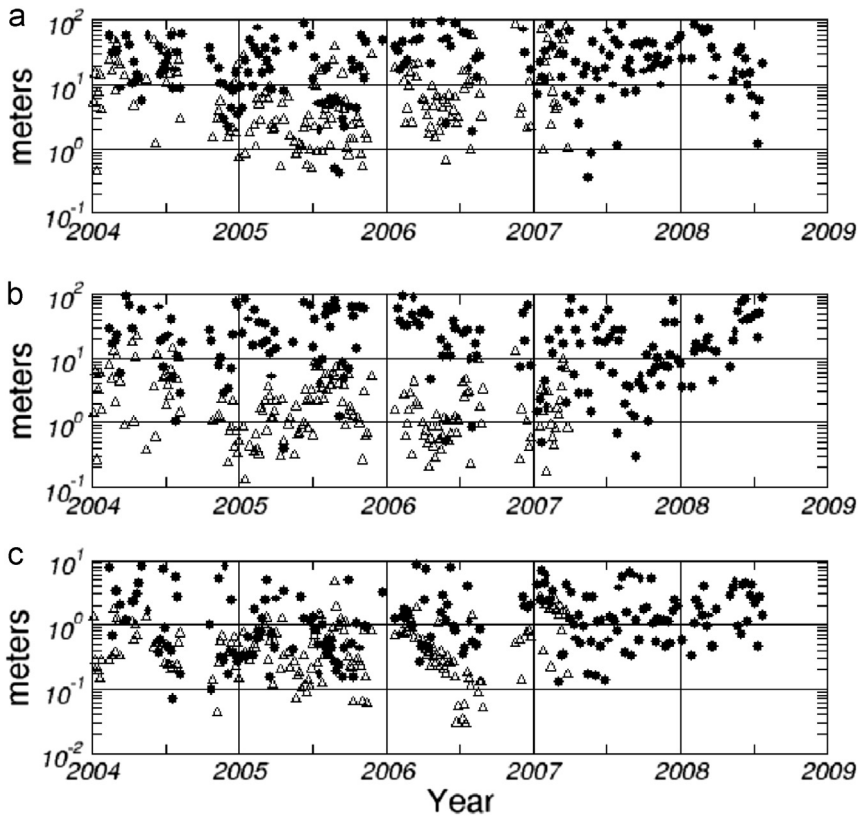

Fig. 6.5. RMS values of the overlap differences correspond to the rms of the position differences between successive data-arcs over overlap duration of 21 hours for MEX (solid circles) and 2 hours ODY (open triangles), respectively. (a) Along-track direction, (b) normal to the orbit plane, and (c) radial direction.

MEX precise orbit reconstruction process consists of modeling all the forces acting on the spacecraft. A first type of forces are gravitational forces due to Mars (both static and variable gravity), the Martian moons, and the other planets. A second type of forces are non-gravitational forces due to external or internal factors: atmospheric drag, solar pressure and albedo radiation exert forces on the faces of the spacecraft (bus, solar panels and High Gain Antenna HGA), while attitude maneuvers (Wheel-Off-Loading, WoL) generate residual accelerations (for more details about the MEX force model, see Rosenblatt et al., 2008). The second step of the orbit reconstruction process consists of generating theoretical tracking data on the basis of this force model in order to fit it to tracking data collected at deep space tracking stations on Earth (DSN or ESTRACK, Holmes et al., 2008). Tracking data are line-of-sight Doppler and range, or round-trip light time, measured at X-band (see Moyer, 2000).Tracking sessions explicitly scheduled for the radio-science experiment (primarily at pericenter and apocenter passes) were used for the precise orbit computation, as well as tracking data collected for the purpose of radio navigation. The fit uses the well-established least-squares filter and allows us to adjust parameters related to the force model and to the tracking measurements themselves (see Konopliv et al., 2006; Rosenblatt et al., 2008; Marty et al., 2009). The fit is performed on successive data arcs of a few days in length (typically 4 days for MGS and ODY and 6 days for MEX), requiring adjustment of the state vector at the beginning of each data arc. The other parameters adjusted for each data arc are the residual acceleration generated at each WoL maneuver in the data arc and two scale factors quantifying the effect of external non-gravitational forces (drag and solar radiation pressure). These scale factors are adjusted in order to compensate for the inaccurate modeling of these forces. In particular, uncertainties are associated with the atmospheric density at pericenter passes, the orientation of the faces of the spacecraft, and the a priori knowledge of residual acceleration at each attitude maneuver (e.g. Rosenblatt et al., 2008).

Table 6.1
Phobos and Deimos (GM) solutions.

	***GM* solutions (10^{-4} km^3/s^2)**	
	Secular (10-σ formal error)	**Flyby (1-σ formal error)**
Phobos		7.127 (0.021), *MEX 2008*[c]
	7.11 (0.02), *MEX*[a]	7.11 (0.03), *MEX 2008*[d]
	7.11 (0.056), *MGS,ODY,MRO*[b]	7.092 (0.004), *Viking-1, Phobos-2*[e]
		7.084 (0.007), MEX 2010[f]
Deimos	1.0 (0.6), *MEX*[a]	
	0.99 (0.15), *MGS,ODY,MRO*[b]	1.01 (0.03), *Viking-2*[e]

[a] Rosenblatt et al., 2008.
[b] A. Konopliv, pers. comm., August 2013.
[c] Andert et al. (2010); UniBw solution.
[d] Andert et al. (2010); ROB solution.
[e] Jacobson (2010).
[f] Pätzold et al. (2014).

The adjusted force model and initial state vector provide the reconstructed orbit for each data arc, and the precision of this orbit is estimated by performing orbit overlap differences between successive data arcs. Fig. 6.5 displays the overlap differences for MEX and ODY (see Marty et al., 2009). The MEX overlap differences are 20–25 m, on average, which is an improvement by about a factor of two with respect to the navigation orbit (Rosenblatt et al., 2008), but is 10 times worse than the ODY or MGS overlap differences. This is due to the incomplete tracking coverage of MEX. In particular, only about one third of the pericenter passes within a data arc are tracked from Earth, and the WoL events are never tracked. The tracking gaps at MEX pericenter are due to the fact that the HGA is fixed to the spacecraft bus and cannot be

oriented toward Earth when other instruments observe Mars. The lack of tracking around WoL events is due to the required attitude of the spacecraft during the maneuver (Pulido-Cobo and Schoenmaekers, 2004). As a consequence, residual accelerations from atmospheric drag and WoL events are not well resolved and the quality of the reconstructed orbit is degraded. ODY and MGS undergo a smaller drag since their orbital altitude at pericenter is higher than for MEX. Furthermore, in contrast to MEX, the ODY and MGS orbits are nearly circular so that the drag is sensed all along the orbit, and not just around the pericenter. ODY and MGS also have the advantage of a steerable HGA, thereby allowing continuous tracking. For these reasons the orbits of ODY and MGS are better resolved than for MEX.

The average precision of 20–25 m on the reconstructed MEX orbit is far from the required 1-meter level. It was thus impossible to extract the small signals due to either the seasonal variations of the lowest degree harmonics of the gravity field or the solid tides. Nevertheless, the improvement of the MEX reconstructed orbit has allowed us to improve the ephemeris of Phobos. Indeed, the accuracy of the position of Phobos derived from images taken by the onboard cameras has been improved by about 25 meters, corresponding to the improvement of the MEX orbit by a factor of about two with respect to the navigation orbit (Rosenblatt et al., 2008). The precision of the reconstructed MEX orbit was also sufficient to reveal the small secular drift due to the mass of Phobos. A new estimate of the Phobos mass (called the secular solution) based on the MEX precise orbit reconstruction was obtained by stacking together data arcs over about three years of tracking data (see Table 6.1 and Rosenblatt et al., 2008). The accuracy of this solution has also benefited from the improvement of the Phobos ephemeris (Lainey et al., 2007). This secular solution is consistent with estimates obtained from close flybys of Phobos (called flyby solutions) performed by MEX (see next Section on Phobos, Andert et al., 2010; Pätzold et al., 2014b) as well as those obtained from re-processing of the former Viking-1 and Phobos-2 flybys (Jacobson, 2010) (see also Table 6.1). The MEX secular solution for Deimos' mass is not as accurate as the one for Phobos because of the smaller signal generated on the MEX orbit due to the more distant orbit of Deimos. However, the value agrees to within the error bars of the recent Deimos' mass solution obtained by re-processing the single Viking-2 flyby (see Table 6.1 and Jacobson, 2010). The precise reconstructed MEX orbits computed at ROB are available as SPICE kernels at both the ESA (ftp://ssols01.esac.esa.int/pub/data/SPICE/MEX/kernels/spk) and NAIF (http://dx.doi.org/http://naif.jpl.nasa.gov/pub/naif/MEX/kernels/spk) websites. These kernels will be regularly updated until the end of the mission.

6.4. Phobos close flybys

Both Mars moons, Phobos and Deimos, were discovered and named by Asaph Hall (Hall, 1878) at the United States Naval Observatory in 1877 as a result of a systematic search during Mars opposition. There have been many speculations on the origin, nature, formation and evolution of the Mars moons: asteroid capture by Mars (Burns, 1992), simultaneous formation with Mars, formation in orbit from a debris disk of a previously larger body destroyed by gravitational gradient forces near Mars (Singer, 2007) and re-accretion of impact debris blasted into Mars orbit (Craddock, 2011) are prominent among these. Rosenblatt (2011) gives an overview of these formation scenarios.

Important for the understanding and investigation of formation scenarios, origin, nature and internal structure is knowledge of the bulk parameters mass, density, gravity field, shape and porosity, all of which constrain any model of Phobos. These bulk parameters are also important for the navigation of a spacecraft near Phobos, particularly for an eventual landing, and must be known to a certain precision. The gravity field can be derived from close spacecraft encounters, but also from distant encounters by observing secular perturbations to the spacecraft orbit over long time periods.

The velocity of a spacecraft flying by a body of sufficient mass at a sufficiently close distance is changed rapidly during this encounter, primarily due to the gravitational attraction of the body. All other perturbing forces acting on the spacecraft are of second order during the flyby. The precise analysis of a flyby requires a very complex dynamic force model to account for all gravitational and non-gravitational forces acting on the spacecraft. The interaction of the attracting force of the perturbing body during a flyby is of short duration for small bodies, inducing a change in velocity shortly before and after the closest approach. Early values for the gravitational parameter GM_{Ph} (gravitational constant G times the Phobos mass M_{Ph}) are based on radio tracking of a few close flybys of the Viking spacecraft in 1977 (Christensen et al., 1977; Tolson et al., 1977, 1978; Williams et al., 1988), and from the Phobos 2 spacecraft in 1989 (Kolyuka et al., 1990), with relative errors of about 10% and 2%, respectively.

Another approach for the determination of the Phobos mass is to use "distant encounters". The first attempts to extract the mass of Phobos and Deimos using this technique were reported by Smith et al. (1995). Similar to the close encounter technique, secular perturbations to the orbital elements of the spacecraft orbit are analyzed using a complex dynamical force model. Due to the large distance from Phobos to the spacecraft, orbit changes caused by the gravitational attraction of Phobos are very small for short observation times. Therefore, spacecraft tracking data over a long period of time are needed (see also Section 6.3).

The eccentric orbit of MEX provided the first opportunity in twenty years to perform close flybys at Phobos for studies of its gravity field. Several MEX flybys were performed at Phobos since the Mars orbit insertion in late 2003, three of which have been used by the MaRS team to carry out gravity field measurements. Pätzold et al. (2014b) provide an overview on estimates of the bulk parameters of Phobos from other missions, including the results from the three MaRS flybys.

6.4.1. The flybys

The apoapsis of the elliptical MEX orbit established in December 2003, intersects the orbit of Phobos and occasionally results in close encounters. The attracting gravitational force of Phobos perturbs the velocity of the MEX spacecraft during sufficiently close flybys, producing an observed Doppler shift of the received radio tracking frequency. The magnitude and sign of the frequency shift depends on the flyby distance, the direction and magnitude of the change in flyby velocity and its projection onto the LOS to Earth (Anderson, 1971; Pätzold et al., 2001). Pätzold et al., 2009a estimated that flyby distances well within 500 km to Phobos were needed to achieve meaningfully improved mass determinations compared to past missions. MaRS obtained good data from close flybys in 2006 at a distance of 459 km, in 2008 at 275 km (Andert et al., 2010) and again in 2010 at 77 km (Pätzold et al., 2014a).

The first real MEX opportunity for a sensitive mass determination of Phobos occurred on 23 March 2006 at a distance of 459 km (Andert et al., 2010). The flyby was fully visible from the 70-m NASA DSN ground station antenna near Madrid, Spain, and the flyby geometry was nearly optimal with the angle between the flyby trajectory and the direction to Earth changing from 96° to 105° during the flyby. An angle of 90° produces the strongest Doppler shift and can be considered optimal. Unfortunately, the recording started only 15 minutes before closest approach and the estimate of the initial orbital parameters, and therefore the pre-encounter frequency residual bias, was not sufficiently precise. The

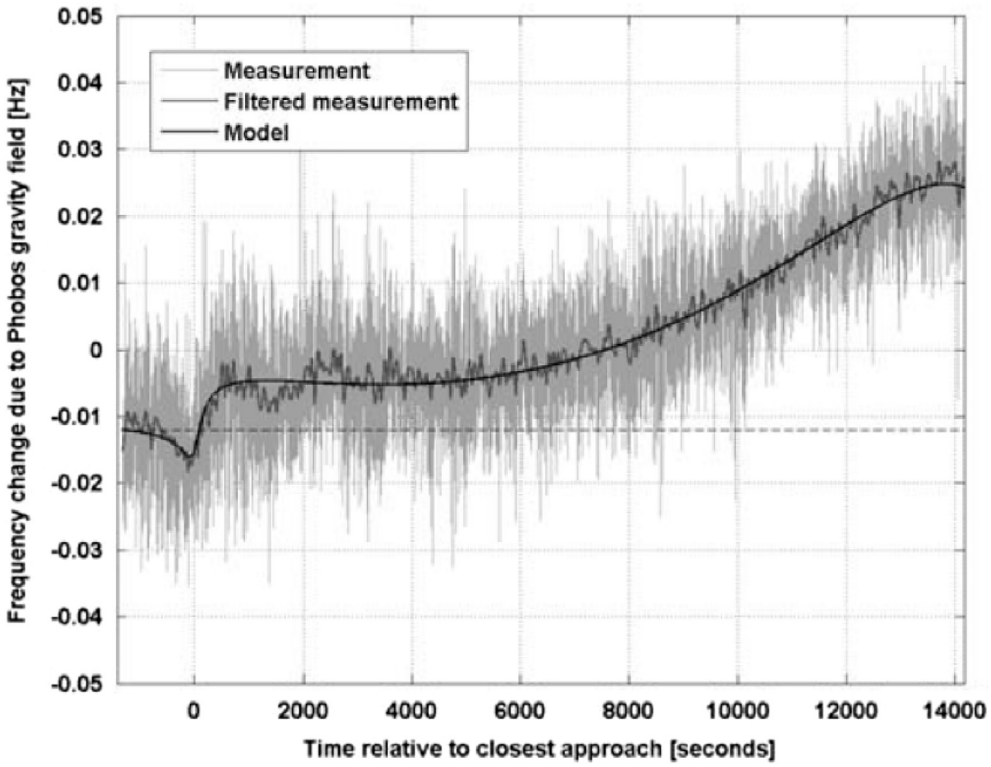

Fig. 6.6. MEX radio carrier frequency residual (received frequency, observed minus predicted) at 8.4 GHz due to the change in spacecraft velocity caused by gravitational attraction of Phobos. The measurements were recorded at the NASA Madrid tracking station on 23 March 2006. The 'Filtered measurement' is a running mean of 40 points; the 'Model' corresponds to GM for the least-squares solution. The dashed line shows an initial constant bias of $-$ 12.01 $\pm$ 0.04 MHz at the beginning of the measurement caused by small velocity contributions not included in the frequency prediction. Figure taken from Andert et al., (2010).

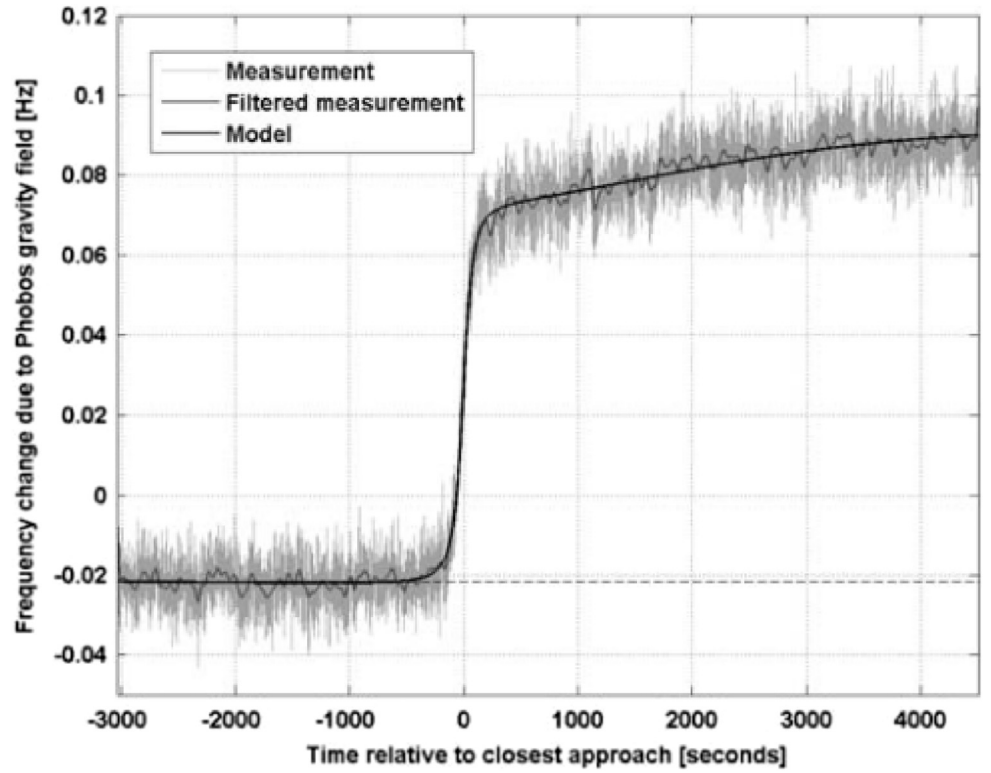

Fig. 6.7. Same as Fig. 6.6 for the measurements recorded at the NASA Madrid tracking station on 17 July 2008. The 'Filtered measurement' is a running mean of 40 points; the 'Model' corresponds to GM for least squares solution. The dashed line shows an initial constant bias of $-$ 21.03 $\pm$ 0.07 MHz at the beginning of the measurement caused by small velocity contributions not included in the frequency prediction. Figure taken from Andert et al. (2010).

fit considered the initial state vector, a scale factor for the solar radiation pressure, the bias f_0 of the X-band frequency residuals and finally the GM_{Ph}. The uncertainty of the pre-encounter bias f_0 = (−12.01 ± 0.04) MHz contributed significantly to the uncertainty of the GM_{Ph} solution. A change in the amplitude of the frequency residuals by 0.1 MHz would change the GM_{Ph} solution by 0.1 10^{-4} km^3s^{-2}. The pre-encounter bias is the result of small Doppler contributions that were not included in the predicted received frequency (Fig. 6.6).

The second MEX opportunity for a Phobos mass determination occurred on 17 July 2008 at a distance of 275 km with an optimal geometry (Andert et al., 2010). Fig. 6.7 shows the frequency residuals at X-band within approximately ±1 hour about closest approach. Again, it is assumed that the changes in residual frequency are solely attributed to Phobos after correcting for the contributions from the Earth troposphere and ionosphere. The flyby was fully observed at the 70-m DSN ground station near Madrid, Spain. The solid line in Figure. 1 is a least-squares fit to the residual frequency and solves for the pre-encounter velocity vector, the scaling factor for the solar radiation pressure, pre-encounter bias f_0 and finally the GM_{Ph}.

Analysis methods for the MEX 2008 close flyby were developed and applied by two independent groups of the MaRS Team: (a) Institute of Space Technology, University of the German Armed Forces in Munich (UniBw), Germany, and (b) the Royal Observatory of Belgium (ROB) in Brussels, Belgium. The approach at UniBw resulted in a least-squares solution for the mass of Phobos based on the use of two-way Doppler tracking observations from a time interval centered near the closest approach of MEX to Phobos. A predicted received frequency was computed from the spacecraft orbit before the flyby, taking into account gravitational and non-gravitational perturbing forces acting on the spacecraft, but excluding the mass of Phobos. This predicted baseline frequency was also corrected for contributions from the radio signal propagation through the Earth's atmosphere. The resulting frequency residuals represent the change in the spacecraft velocity along the spacecraft-to-Earth line-of-sight caused by Phobos (Fig. 6.6). Solutions for Phobos GM_{Ph} from the Brussels group at ROB were obtained using the software package "Géodésie par Intégration Numérique Simultanée (GINS)" developed at the Centre National d'Etudes Spatiales (CNES) and adapted for use in planetary geodesy applications at ROB. The data reduction and analysis software and their application to the MEX observations were carried out independently by each group and produced results that were in mutually very good agreement. The ROB group (Rosenblatt et al., 2008) also determined GM_{Ph} from the secular perturbation of the MEX orbit based on precise determination of the MEX orbit over successive 7 day data arcs and this solution was also in very good agreement with the UniBw and ROB solutions from the close 2008 flyby.

The GM_{Ph} values from the MEX 2008 flyby (Andert et al., 2010) are as precise as the value by Berthias (1990) from the reanalyzed Phobos-2 tracking data although the MEX distance was larger. The accuracy of 0.3 – 0.4% is attributed to the use of a higher radio carrier frequency (X-band), the most recent Mars gravity field (Konopliv et al., 2006), and the most recent ephemerides of the planets (Folkner et al., 2008) and Phobos (Jacobson, 2008). A reanalysis using the updated Phobos ephemeris from Jacobson (2010) slightly changed the value of GM_{Ph}.

The third MEX close flyby on 3 March 2010 was the closest approach to Phobos of any spacecraft. Initially, a closest approach of 62 km was planned in order to resolve the contribution from the second degree harmonic C_{20} of the Phobos gravity field. An overperformance of the trajectory maneuver some days before the flyby, however, resulted in a final closest approach distance of 77 km. The larger distance substantially reduced the C_{20} contribution to the change in spacecraft velocity. Although the flyby geometry was considered optimal, the fit to the X-band frequency residuals (Fig. 6.7),could not resolve C_{20} at sufficient accuracy (Pätzold et al., 2012). Pätzold et al., 2014a reported the result as

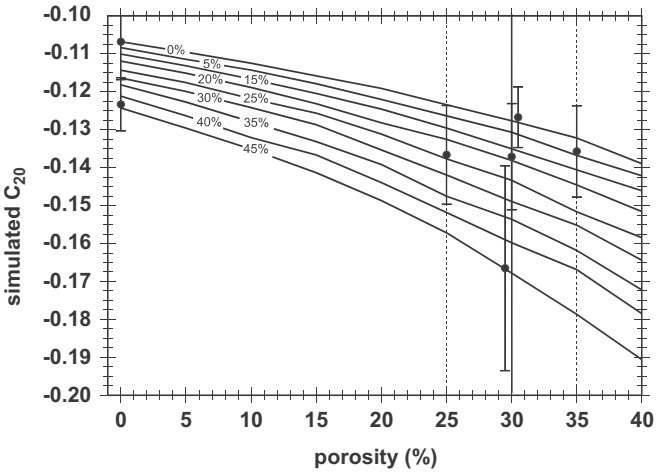

Fig. 6.8. Simulated C_{20} as a function of porosity and water ice content (labeled for each solid line). The simulation returns the homogeneous C_{20} value for zero porosity and zero water ice content. The simulated C_{20} decreases with increasing porosity and water ice content, as expected for a loosely aggregated inhomogeneous body. The argument of reasonable "rock" density, however, restricts the water ice content to below 20%.

$$GM_{Ph} = (7.072 \pm 0.039) \cdot 10^{-4}\ km^3s^{-2} \quad (3\sigma)$$
$$C_{20} = (-0.1145 \pm 0.147) \quad (3\sigma)$$

The result suggests a potentially inhomogeneous interior for Phobos, but the error is too large to justify a solid statement. The error bar includes the C_{20} value for an homogeneous interior. Surprisingly, the error for GM_{Ph} is comparable to the error from the MEX 2008 flyby, although the closest approach distance was four times closer. This is another indication that the GM_{Ph} and the C_{20} fit parameters are highly correlated for this flyby geometry. A test solving for the GM_{Ph} only, therefore assigning the C_{20} contribution to the point mass, yields a slightly higher mass at two times better precision. The 2010 Phobos flyby thus provided the first estimate of the gravity coefficient C_{20}, albeit with a very high uncertainty.

6.4.2. The internal structure

Andert et al. (2010) concluded from the results of the 2008 flyby that Phobos is most probably porous. The bulk density of Phobos computed from the optically derived volume (Willner et al., 2010) and the 2008 mass value is ρ_{bulk} = (1876 ± 20) kg m^{-3}, which is significantly less than any anticipated material density, suggesting a porosity of (30 ± 5)% (Andert et al., 2010). The mass value from the 2010 flyby yields a bulk density of ρ_{bulk} = (1862 ± 20) kg m^{-3} using the volume from (Willner et al., 2010). These values for the bulk densities agree within the error, but do not improve the accuracy because the volume uncertainty dominates the error for the bulk density.

What values of C_{20} and C_{22} are expected for a porous body? The internal mass distribution of Phobos is modeled as a composite of solid elements in spherical coordinates. The body is subdivided in longitude and latitude by elements of 1° × 1° in size. The radius is divided into 50 concentric zones with sizes between 180 and 260 m, depending on the dimensions of the major axes. The resolution in longitude, latitude and radius ensures a high accuracy for the representation of the shape of Phobos. The use of spherical coordinates prevents biased solutions for C_{20} and C_{22}

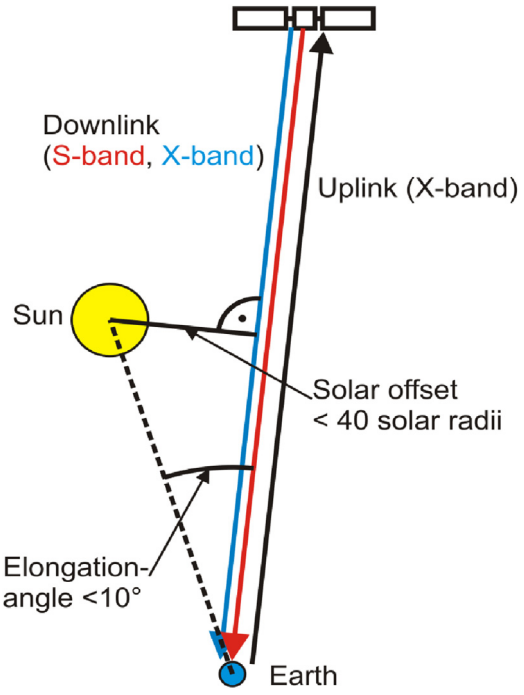

Fig. 7.1. Superior solar conjunction geometry. Radio signals are transmitted between the Earth and Mars Express in two-way-mode.

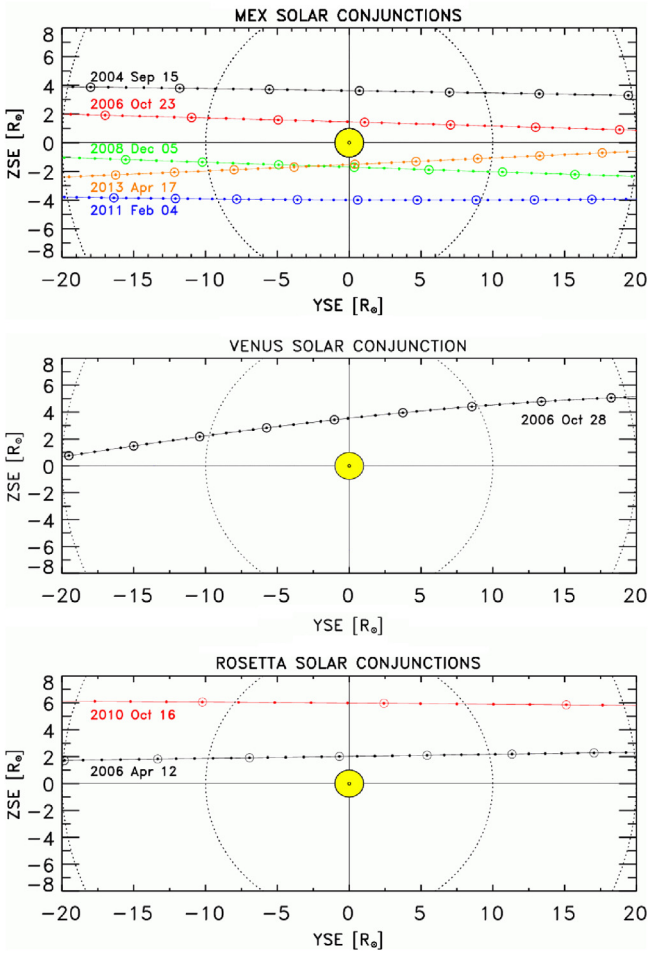

Fig. 7.2. All solar conjunctions of Mars Express (top panel), Venus Express (middle panel) and Rosetta (bottom panel) from 2004 to 2013 used for coronal radio sounding. The position of the MEX/VEX/Rosetta spacecraft is plotted as seen from Earth projected onto the plane of sky relative to the Sun within ± 20 $R_\odot$. The dots along the track mark the position at 00:00 UT each day. The exact date of conjunction is given for each trajectory.

caused by incorrect shape modeling. Each of these volume elements is assigned a certain density, thereby defining the mass of this element. All elements arranged to fit the shape of Phobos and filling its entire volume are constrained by the observed mass, volume, and derived bulk density (Fig. 6.8). Assuming a homogeneous Phobos interior, and assigning the same density of 1862 kg m^{-3} to all elements, the model yields the observed mass and a theoretical value for the oblateness, $C_{20,shape}$ (Pätzold et al., 2014)

6.4.3. The origin

The porosity, defined as the ratio of the bulk density to the grain density of an object, represents the percentage of the volume occupied by voids. The porosity of Phobos is computed from its mass, its bulk density and the known grain densities of the hydrous chondrites of the CM group and the Tagish Lake meteorite samples. The result of $30 \pm 5\%$ suggests that the interior of Phobos contains large voids. Similar large porosities and low bulk densities have been found in C-type asteroids such as the asteroid Mathilde (Yeomans et al., 1997) and Jupiter's small inner moon Amalthea (Anderson et al., 2005). If a similar formation process is responsible for these porous bodies, however, is totally unclear.

The interior structure of Phobos could well be the result of its complete shattering and subsequent reassembly, as is thought to have occurred in the history of many asteroids subjected to violent collisions (Richardson et al., 2002). The existence of the Stickney crater on Phobos would support the conclusion that Phobos contains large voids throughout its interior.

The origin of Phobos can be discussed in terms of its orbital history. Several scenarios ranging from possible to speculative have been proposed. The surface of Phobos shows some spectral similarities to those of various asteroid types. Based on these similarities it was suggested that Phobos is a former asteroid, formed in the outer asteroid belt and later captured by Mars (Burns, 1992). This scenario, however, does not explain how to account for the energy loss required to change the incoming hyperbolic orbit into an elliptical orbit bound to Mars (Burns, 1992; Peale, 2007). Models of orbit evolution based on tidal interactions between Mars and Phobos cannot account for the current near-circular and near-equatorial orbit (Mignard, 1981). Scenarios of evolution to the current circular orbit require an additional drag by e.g., the primitive planetary nebulae or the Martian atmosphere (Sasaki, 1990). An alternative is that Phobos formed in an orbit around Mars. Phobos and Deimos could be remnants of an early, larger body that was broken into parts by gravitational gradient forces during Mars capture (Singer, 2007). Another scenario is that Phobos could have formed by the re-accretion of impact debris lifted into Mars orbit (Craddock, 2011). If Phobos were a remnant of a larger moon, it is not expected to be as porous as is reported here. If Phobos were formed from the re-accretion of impact debris lifted into Mars orbit, the initial disk would be composed of a mixture of Martian crust and impactor material. The spectral properties of the Phobos surface and the Martian crust, however, do not match very well.

This inconsistency is resolved by a collision between a body already orbiting Mars but formed from the debris disk remaining after formation of Mars and a second body originating from the asteroid belt (Peale, 2007). This scenario is consistent with the high porosity of Phobos and its spectral properties.

Andert et al. (2010) already concluded on the basis of the high porosity that Phobos is not a captured asteroid but re-accreted in orbit about Mars from an existing material disk. Giuranna et al.

Table 7.1
Solar conjunctions of ESA spacecraft, 2004–2013.

S/C	Conjunction number	Conjunction Date [DOY]	Superior Conjunction Interval [DOYs]	Minimum offset (solar radii) [elongation (deg)]	Geocentric range (AU)	Duration (days)	Tracking passes	
							Doppler	ranging
MEX	C1	15 SEP 2004 [259]	15 AUG - 18 OCT [228–292]	3.7 N [1.0°]	2.66	64	36	9
ROS	C1	12 APR 2006 [102]	14 MAR - 19 MAY [073–139]	2.1 N [0.6°]	2.58	66	36	22
MEX	C2	23 OCT 2006 [296]	21 SEP - 26 NOV [264–330]	1.5 N [0.4°]	2.59	66	28	0
VEX	C1	28 OCT 2006 [301]	18 SEP - 10 DEC [261–344]	3.6 N [0.9°]	1.72	83	19	0
MEX	C3	05 DEC 2008 [340]	31 OCT - 14 JAN [305–014]	1.8 S [0.5°]	2.48	76	94	7
ROS	C3	16 OCT 2010 [289]	01 OCT - 31 OCT [274–304]	6.0 N [1.6°]	4.36	30	32	5
MEX	C4	04 FEB 2011 [035]	22 DEC - 27 MAR [356–086]	4.0 S [1.1°]	2.37	96	59	26
MEX	C5	17 APR 2013 [107]	01 MAR - 02 JUN [060–153]	1.5 S [0.4°]	2.37	93	TBD	TBD

MEX = Mars Express; VEX = Venus Express; ROS = Rosetta.

(2011) came to the same conclusion on the basis of spectra from the Planetary Fourier Spectrometer (PFS) onboard MEX. The origin of this material disk is unknown. Rosenblatt (2011) discusses three possible origins:

- An asteroid (Singer, 2007) that passed sufficiently close to Mars to be destroyed by gravitational or tidal gradients or by a collision with another object already in orbit about Mars. The origin of the intruding object is unknown. Rosenblatt (2011) argues in this case for an asteroid from the main belt in order to explain possible water ice content within the re-accreted Phobos.
- A major impact on Mars which lifted material into the Mars orbit (Craddock, 2011). The material of the disk would mostly contain the material from the impactor (Rosenblatt, 2011), which would explain that the spectral properties of Phobos and the Mars surface do not match well (Giuranna et al., 2011). It would also explain the low or zero water ice content from the simulations because the water ice within the impactor would have evaporated and disappeared.
- Formation from a remnant debris disk from the formation of Mars. This implies that the composition of Phobos must resemble the early material that formed Mars, thereby accounting for a certain amount of water ice content. Whatever the source of the material disk is, the (new) Phobos must have re-accreted from the material within this debris disk around Mars. As to the internal structure, large pieces from the material disk were the first to be accreted, leaving space between them that could not be filled by smaller pieces attracted by the newly formed and growing body. This would explain the high porosity as one reason for the low bulk density.

7. Solar conjunctions: radio sounding of the Solar Corona

7.1. Introduction

The planet Mars undergoes superior solar conjunction roughly every 26 months, passing behind the Sun (as seen from the Earth) at small elongation angles relative to the solar disk. For planning purposes (Pätzold, et al., 2004), MaRS defines the phase of superior solar conjunction as $\pm 10°$ solar elongation angle, corresponding to approximately ± 40 solar radii ($R_\odot$) heliocentric distance of the proximate point along the radio ray path from spacecraft to Earth, sometimes called the "solar offset" (see Fig. 7.1). As the MEX radio signals propagate through the dense hot solar plasma, the carrier frequency undergoes a phase advance and modulated codes (ranging) are subject to a propagation delay.

Radio sounding the solar corona using radio communication links with interplanetary spacecraft at times of solar conjunction is a well-established method to deduce the large-scale coronal structure. First performed with Pioneer 6 in 1968 (Goldstein, 1969; Levy, et al., 1969), it was continued with Helios (Volland, et al., 1977), Pioneer 10/11 (Woo, 1978), Viking (Woo and Armstrong, 1979), Voyager (Anderson, et al., 1987), Ulysses (Bird et al., 1994; Pätzold, et al., 1995), Galileo (Wohlmuth, et al., 1997a) and Cassini (Morabito et al., 2003). More recently, results from the solar conjunctions of Mars Express, Venus Express and Rosetta from 2004 to 2008 were summarized in Pätzold, et al. (2012). Soja et al. (2014) report on VLBI observations of radio sources near the solar disk which deliver similar quantities from the solar corona as the spacecraft conjunction experiments but may be performed on a more regular basis.

Radio sounding experiments at superior conjunction are conducted in two-way mode. The X-band uplink is transmitted from a ground station to the spacecraft and transponded (retransmitted) back to Earth at both X-band and S-band. The dense plasma of the solar corona, a dispersive medium for electromagnetic waves, induces phase shifts and propagation time delays onto the carrier signal. These changes can be measured to determine the total electron content and large-scale coronal structures, as well as short-time variations such as the passage of a coronal mass ejection (CME) through the ray path (Bird, 1982). Furthermore, it is possible to separate the frequency shifts imposed on the uplink path from those on the downlink path. Since the uplink and downlink raypaths are spatially separated, it is possible to determine the bulk propagation velocity the solar wind plasma in the coronal acceleration region (Wohlmuth, et al., 1997b).

7.2. Coverage

The Mars Express spacecraft has been used for radio sounding during the five superior conjunctions in 2004, 2006, 2008/09, 2010/11 and 2013. Fig. 7.2 (upper panel) shows the position of Mars as seen from Earth projected onto the plane of sky during each of these opportunities. The MEX spacecraft passed over the northern solar pole in 2004 and 2006 and south of the Sun for the last three conjunctions.

Including results from the solar conjunctions of the radio-science experiments RSI onboard Rosetta (ROS) (Pätzold, et al., 2007) and VeRa onboard Venus Express (VEX) (Häusler, et al., 2006), a total of 370 Doppler tracking passes were performed (see Fig. 7.2 and Table 7.1). Dual-frequency ranging data were recorded during 102 tracking passes.

Fig. 7.3 shows the sunspot number, a proxy for the solar activity level, for the years 2004 to 2012. The conjunctions in 2004 and

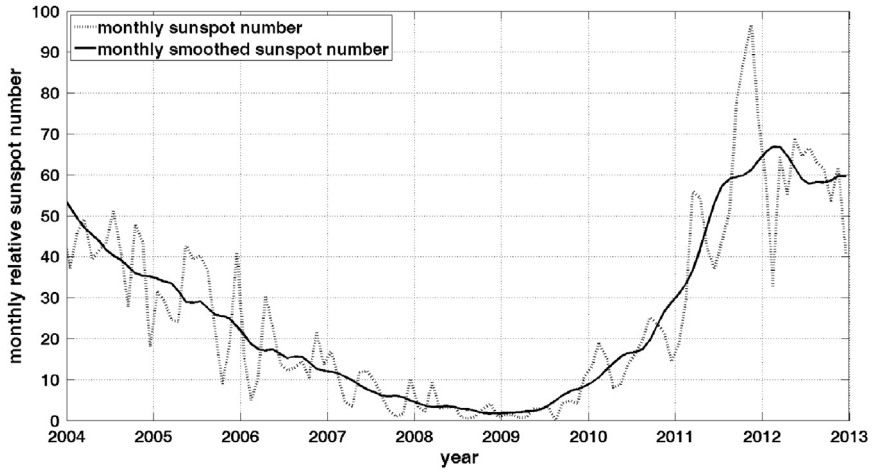

Fig. 7.3. Monthly relative sunspot number (proxy for the solar activity level) from 2004 to the end of 2012.
Source: http://sidc.oma.be/sunspot-data/; SIDC – Solar Influences Data Analysis Center, Royal Observatory of Belgium.

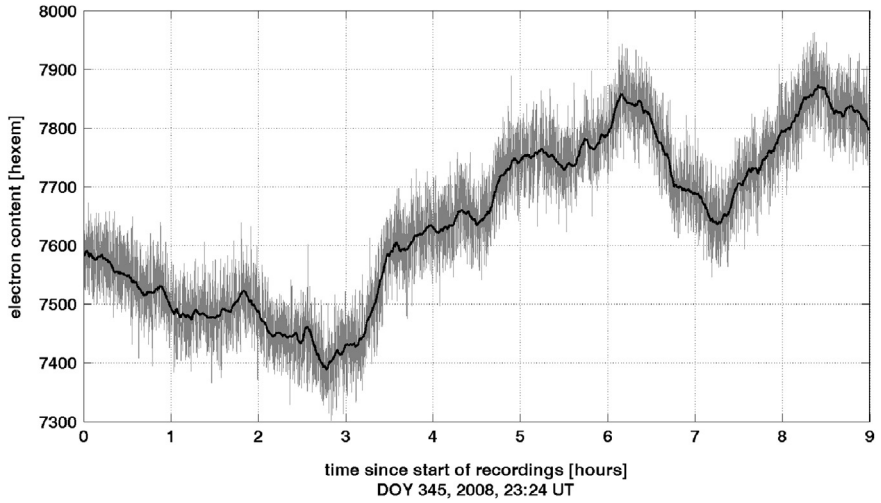

Fig. 7.4. Total electron content derived from the propagation delay time (gray curve). For comparison, the black curve is the change in electron content, derived from differential Doppler measurements, after shifting along the ordinate scale to coincide with the absolute value at the start of recording.

2006 took place during the declining phase of the solar activity cycle. During the third MEX conjunction (2008/09), the Sun was very near its activity minimum. The conjunctions in 2010/11 by MEX and ROS took place during the phase of increasing activity at the beginning of solar cycle 24. The latest MEX conjunction in 2013 most likely occurred during a phase of maximum activity. The MEX conjunctions thus cover nearly a full solar activity cycle.

7.3. Observed quantities

The coronal plasma induces strong phase shifts (Doppler) and propagation time delays (ranging) on the transmitted downlink signals at X-Band (8.4 GHz) and S-band (2.3 GHz). The slightly different Doppler shifts of these two coherently transmitted radio signals reveals variations in the electron content of the coronal plasma as a function of observation time. The total coronal electron content can be determined using the differential propagation time delay between ranging signals at X- and S-band (Bird, 1982).

7.3.1. Differential Doppler

Temporal changes of the electron density N_e along the line of sight y lead to changes in the frequency recorded at the ground station f_{rec} given by:

$$f_{rec} = f_0 - \frac{v_{rel}}{c} f_0 + \frac{40.31\ m^3 s^{-2}}{c} \frac{1}{f_0} \frac{d}{dt} \int_{S/C}^{Earth} N_e dy \tag{7.1}$$

where f_0 is the transmitted carrier frequency, vrel is the relative velocity between the spacecraft and ground station, and c is the speed of light (Pätzold, et al., 2012). The integral $\int_{S/C}^{Earth} N_e dy$ is the total electron density per unit area *TEC*, or column density, also sometimes called the total electron content (TEC).

Using dual frequency recordings at X-band and S-band with the known exact frequency ratio of $f_X/f_S = 11/3$, one may eliminate all nondispersive effects in (7.1) by computing the differential Doppler:

$$\delta f = f_{S,received} - \frac{3}{11} f_{X,received}$$

$$= \frac{40.31}{c} \left\{ \frac{1}{f_{S,down}^2} - \frac{1}{f_{X,down}^2} \right\} f_S \frac{d}{dt} \int_{S/C}^{Earth} N_e dy \tag{7.2}$$

Integration of the differential Doppler (7.2) over time yields the change in electron content ΔTEC since the beginning of the

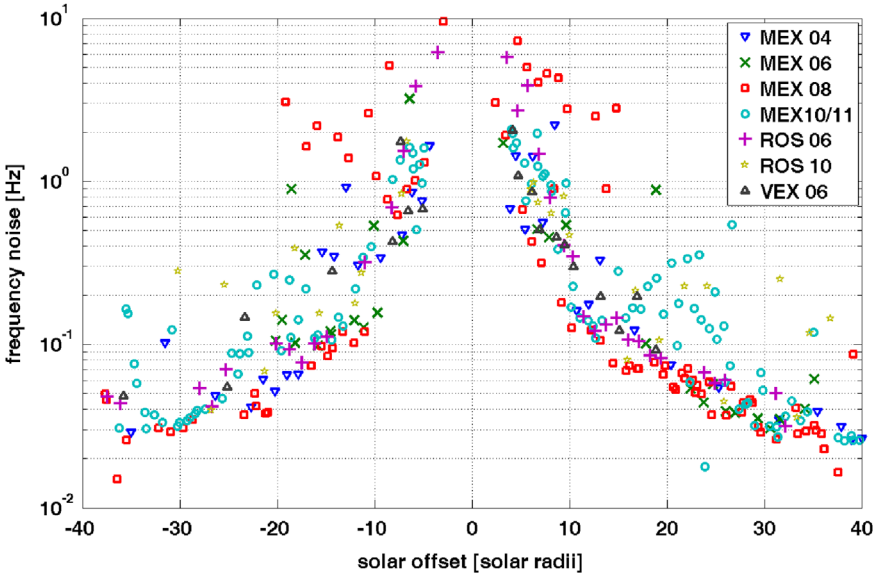

Fig. 7.5. Standard deviation (1σ) of the differential frequency (computed over the entire tracking pass) from all tracking passes during all seven conjunctions as a function of solar offset.

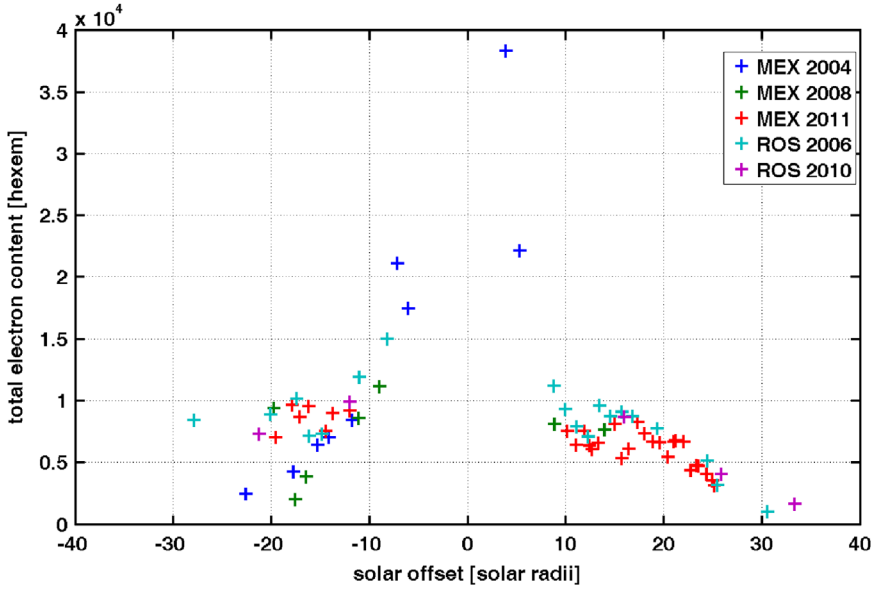

Fig. 7.6. Total electron content, averaged over the tracking pass for all available ranging observations during the MEX 2004/2008/2011 and Rosetta 2006/2010 conjunctions, as a function of solar offset.

measurement

$$\Delta TEC(t) = \frac{c}{40.31}\left\{\frac{1}{f_{S,down}^2} - \frac{1}{f_{X,down}^2}\right\}^{-1} \frac{1}{f_{S,down}} \int_0^t \delta f(t')dt'. \tag{7.3}$$

7.3.2. Differential ranging

The propagation time delay of a radio signal τ includes a dispersive term that is proportional to the total electron content along the line of sight:

$$\tau = \frac{y}{c} + \frac{40.31}{c}\frac{1}{f_0^2}\int_{S/C}^{Earth} N_e dy \tag{7.4}$$

where the first term is the vacuum propagation time. This term cancels out upon using dual-frequency measurements of range delay, yielding a quantity referred to as the differential range

$$\Delta\tau = \tau_S - \tau_X = \frac{40.31}{c}\left\{\frac{1}{f_{S,down}^2} - \frac{1}{f_{X,down}^2}\right\}\int_{S/C}^{Earth} N_e dy \tag{7.5}$$

which directly yields the total electron content *TEC*

$$TEC(t) = \int_{S/C}^{Earth} N_e dy = \frac{c}{40.31}\left\{\frac{1}{f_{S,down}^2} - \frac{1}{f_{X,down}^2}\right\}^{-1} \Delta\tau(t) \tag{7.6}$$

In the following the total electron content and change in electron content are given in units of hexems, where 1 [hexem] = 10^{16} electrons/m².

Fig. 7.4 shows an example for the total electron content as well as the change in electron content from MEX measurements on 2008 DOY 354. The total electron content (gray curve) is computed from the propagation delay time using (7.6). The change in electron content, computed from (7.3), is shown for the same

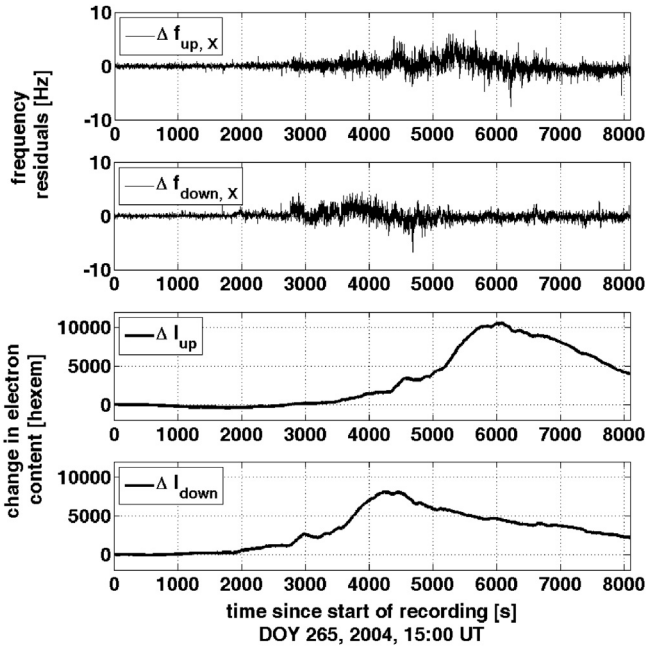

Fig. 7.7. Differential Doppler measurements recorded on 2004 DOY 265. Uplink and downlink X-band frequency residuals (top panels). Change in electron content observed on up- and downlink signal path (bottom panels).

observation (black curve). This latter curve was shifted vertically by a constant value to coincide with value for the total electron content at the beginning of the tracking pass. The noise associated with the change in electron content is significantly lower than that for the total electron content, thereby revealing the fine scale structure. Only the total electron content, however, provides absolute values. A preliminary assessment of the radial variation of the mean frequency fluctuation from (7.3) and the TEC from (7.6) for the MEX 2004 conjunction yielded excellent agreement with previous coronal sounding experiments (Efimov et al., 2010a).

7.4. Results

7.4.1. Large scale structure

Fig. 7.5 shows the mean differential frequency variation obtained from all solar conjunction phases. The 1σ standard deviation computed for each differential Doppler pass is plotted as a function of the solar offset distance. The standard deviation of the differential Doppler frequency is a measure of the density fluctuations along the downlink ray path during the tracking pass. The average differential Doppler variation level of the 2004 and 2010/2011 MEX conjunctions are higher compared to the MEX conjunction phase during the solar minimum. The MEX 2008/09 conjunction shows the lowest variations for solar offsets $R > 20\ R_\odot$, as expected for solar activity minimum (see Fig. 7.5). Inside 20 $R_\odot$, the fluctuations increase strongly and are subject to specific local structures like CMEs, coronal holes and streamers that evolve and intersect the radio ray path.

The measured values of TEC from (7.6) for all available differential ranging observations is shown in Fig. 7.6. Each point represents an average over the whole tracking pass. The TEC roughly follows a power law with the solar offset distance. There is no apparent dependence on the solar activity cycle. Occasional strong increases in TEC can most often be related to coronal streamers or CME events. Pätzold, et al. (2012) showed that the values generally follow the power-law model derived from Ulysses 1991 solar conjunction data (Bird et al., 1994)

7.4.2. Plasma Velocity Determination

As shown in Fig. 7.7 the coronal radio science experiment is carried out in a two-way mode. An X-band uplink signal f_{up} is generated by a hydrogen maser in the ground station and transmitted to the spacecraft. The onboard radio subsystem converts this signal to X-band and S-band downlink signals ($f_{X,down}$ and $f_{S,down}$, respectively), which are then received by the ground station. Between transmission and reception of the signals, both the ground station and spacecraft move a substantial distance, leading to a spatial separation of the uplink and downlink raypaths (Wohlmuth, et al., 1997b).

Plasma structures in the solar wind such as CMEs, propagating outward from the Sun with a velocity v_{CME}, can traverse both the uplink and the downlink signals. Pätzold, et al. (2012) have shown that it is possible to separate the frequency shifts due to the coronal plasma for the X-band downlink ($\delta f_{X,down}$) and X-band uplink (δf_{up}) signal path:

$$\delta f_{X,down} = \frac{3}{11}\frac{121}{112}\left[f_{S,received} - \frac{3}{11} f_{X,received}\right] = \frac{40.31}{c}\frac{1}{f_{X,down}}\frac{dTEC_{down}}{dt} \tag{7.7}$$

$$\delta f_{up,X} = \frac{749}{880}[\Delta f_X - \delta f_{X,down}] = \frac{40.31}{c}\frac{1}{f_{up}}\frac{dTEC_{up}}{dt} \tag{7.8}$$

where $f_{S,received}$ and $f_{X,received}$ are the received S- and X-band frequencies, c is the speed of light, $f_{X,down}$ is the X-band frequency transmitted by the spacecraft ($\approx$ 8.4 GHz), Δf_X are the Doppler frequency residuals and f_{up} is the uplink X-band frequency ($\approx$ 7.1 GHz).

Fig. 7.7 shows the up- and downlink frequency residuals computed according to (7.7) and (7.8) for the MEX recording on 2004 DOY 265, and the respective changes in electron content. Qualitatively, the same plasma structure is observed on the uplink and the downlink signal paths with a temporal offset τ_{Plasma}. Note that the electron content of the uplink path depends strongly on the frequency residuals Δf_X, which are computed using a predicted X-band frequency. This prediction can contain unmodeled errors which affect the results of (7.8). Fig. 7.8 shows the observation geometry. Due to the motion of spacecraft and Earth, the uplink and the downlink raypaths are spatially separated. An outward moving plasma structure like a CME on the west solar limb first crosses the uplink signal path (at point P_{Up}) and then the downlink signal path (at point P_{Down}). The perturbed signature of the CME from the uplink travels from point P_{Up} to the spacecraft and then down to the ground station on Earth. The downlink signature, however, travels from P_{Down} to the ground station directly. As a

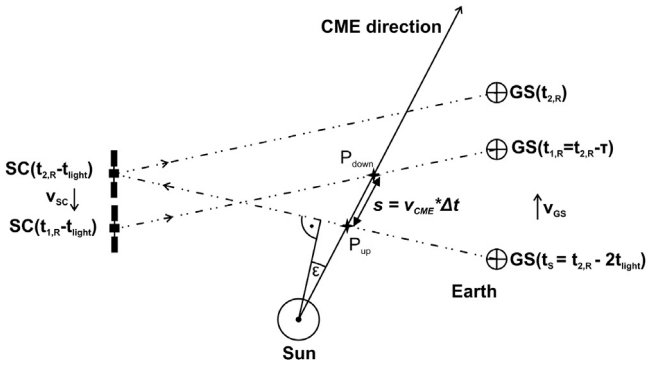

Fig. 7.8. Observation geometry during a solar corona sounding measurement, viewed from above onto the plane defined by uplink and downlink. Due to the motion of spacecraft and Earth, the uplink and downlink signal paths are well separated. A plasma structure such as CME, moving radially outward at the indicated angle ε, is thus detected at two positions P_{up} and P_{down} along the uplink and downlink, respectively, which are separated by the distance s.

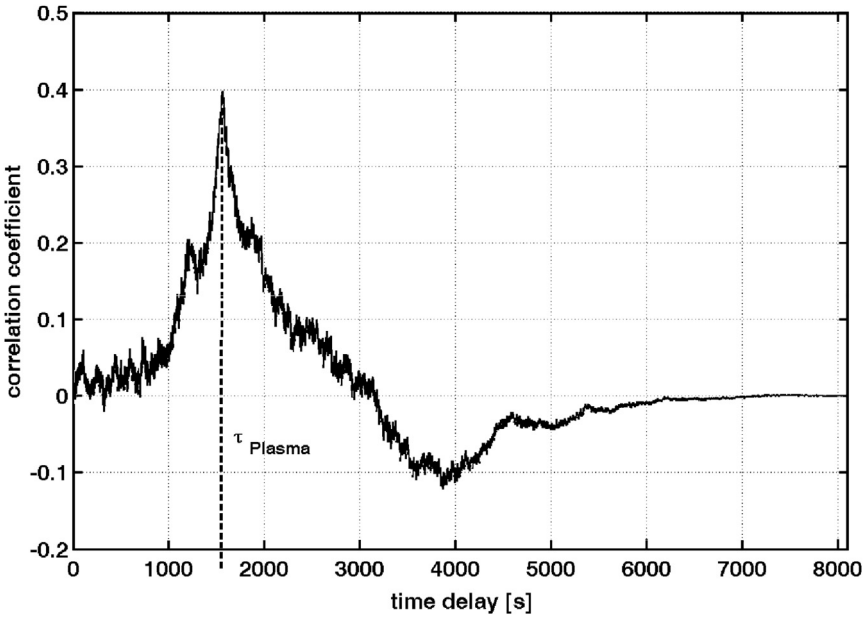

Fig. 7.9. Cross correlation function of the MEX uplink and downlink frequency residuals recorded on 2004 DOY 265. The time delay between the uplink and downlink detections at the ground station is $\tau_{plasma} = 1567$ s.

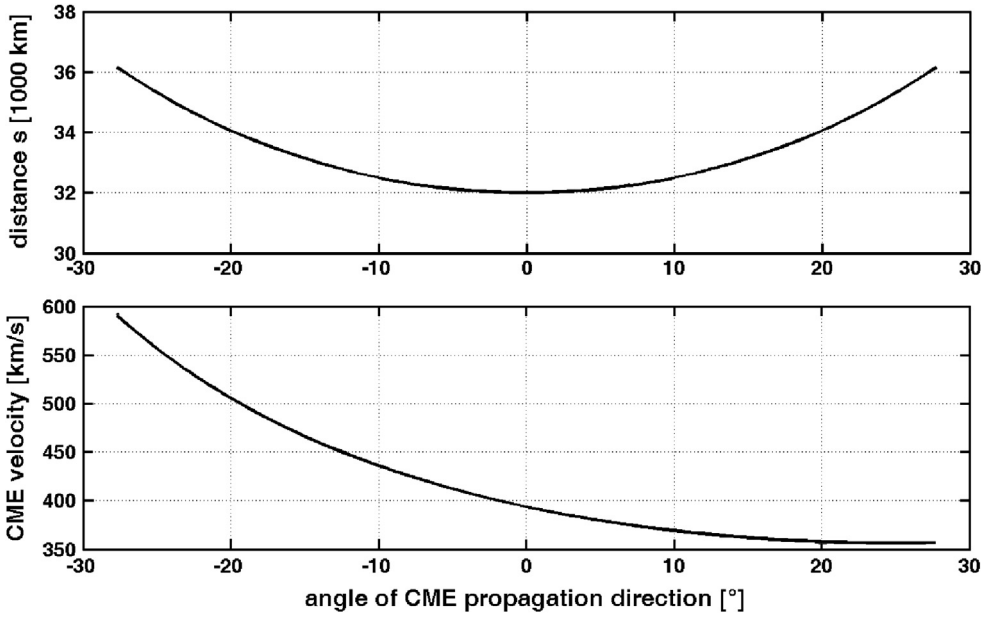

Fig. 7.10. Results of the MEX uplink/downlink cross correlation analysis for 2004 DOY 265. The upper panel shows the distance between the points where the CME crosses the uplink and the downlink signal path as a function of the propagation direction. The direction is denoted by the angle ε to the direction of the closest approach (see Fig. 7.8). Negative angles indicate propagation into the region between spacecraft and proximate point; positive values of ε for the region between proximate point and Earth. The bottom panel shows the derived CME velocity as a function of the propagation direction angle ε.

Table 7.2
CMEs detected by radio coronal sounding and with LASCO.

Year	DoY	Date	Solar offset [$R_\odot$]	Start [UT]	End [UT]	LASCO [UT]
2004	247	03 SEP	15.6	14:05:00	18:00:00	12:18
2004	249	05 SEP	13.2	14:00:00	17:55:00	12:42
2004	263	19 SEP	6.3	13:28:00	17:20:00	14:43/22:18
2004	265	21 SEP	8.5	15:00:00	17:15:00	none
2004	269	25 SEP	13.1	13:00:00	17:05:00	16:42
2010	360	26 DEC	35.5	00:56:50	05:29:00	none
2011	046	15 FEB	9.5	03:01:28	06:14:10	03:54
2011	068	09 MAR	26.6	04:49:20	06:47:29	00:54

result, although the the plasma structure first hits the uplink, its signature is seen first in the downlink signal. The observed temporal offset τ_{Plasma} is not merely the difference of the signal travel times. The CME also needs the time Δt to travel between the two points of interaction on the uplink and downlink, which depends on the distance s between these points and the CME propagation velocity v_{CME}. For any given CME propagation direction, the distance s can be computed from the precisely known Earth and spacecraft trajectories. The total temporal offset τ_{Plasma} is given by

$$\tau_{Plasma} = \tau_{Up} - \tau_{Down} \pm \Delta t = \tau_{Up} - \tau_{Down} \pm \frac{s}{v_{CME}} \quad (7.9)$$

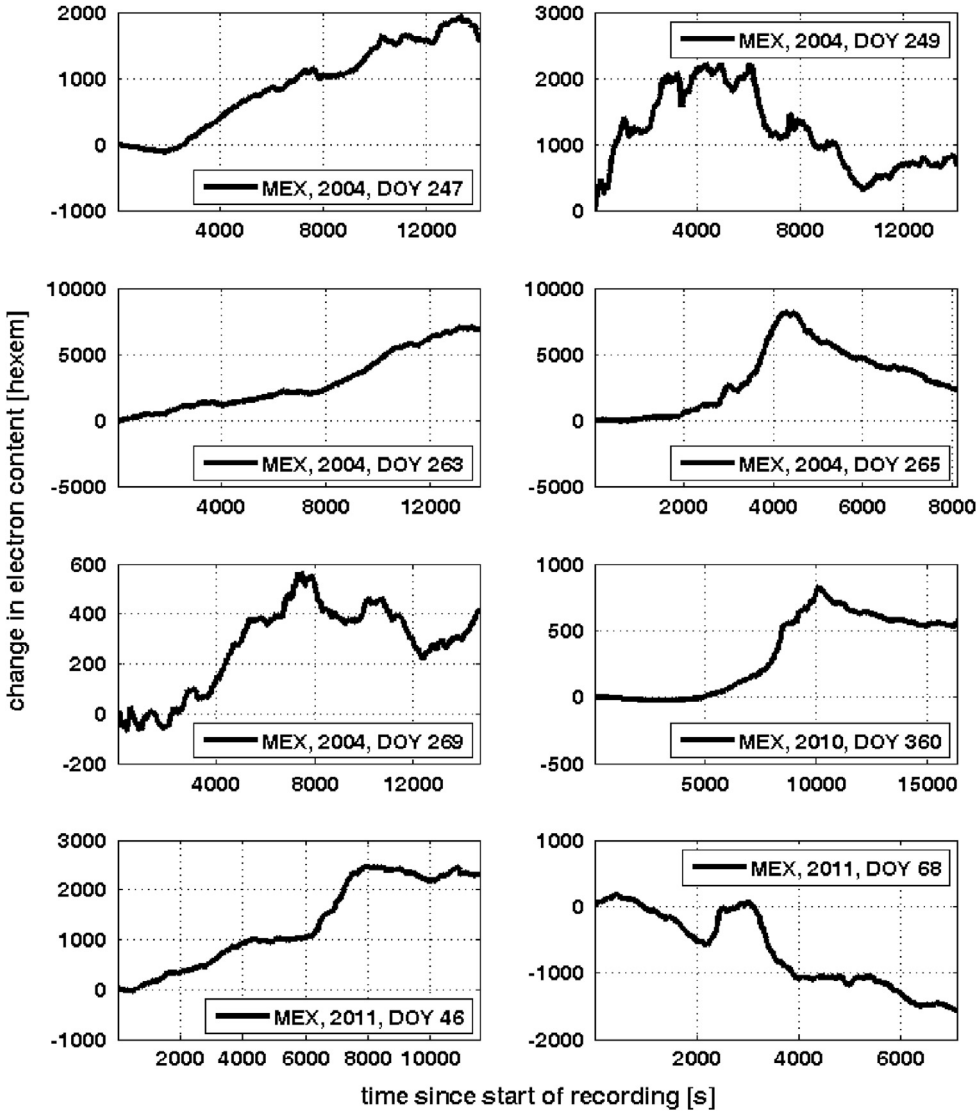

Fig. 7.11. The change of electron content for eight CMEs observed with MEX.

where τ_{Up} and τ_{Down} are the propagation times on the up- and downlink, respectively, which are computed from the CME propagation direction, the known spacecraft and Earth positions and the speed of light c. If the downlink signal is affected first (observation on the east limb of the solar disk) the plus sign holds in (7.9). For observations on the west limb, the uplink signal is perturbed first and the minus sign is valid. The offset τ_{Plasma} is given by the time lag of the maximum in the cross-correlation function between the two time series $\Delta f_{up,X}$ and $\Delta f_{down,X}$. Fig. 7.9 shows an example of the cross correlation function for the MEX observation of 2004 DOY 265. A value of $\tau_{Plasma} = 1{,}567$ s is clearly indicated as the estimated time delay between the signatures of the perturbations from the up- and downlink raypaths.

Fig. 7.10 shows the results from the velocity analysis for the MEX event of 2004 DOY 265. Allowing for different radial propagation directions on trajectories at angles between $\varepsilon = -30°$ and $\varepsilon = +30°$ from the solar limb, the distance s between the two points where the CME crosses the uplink and downlink path varies between 33,100 km and 38,300 km. As both paths are nearly parallel, the distance is smallest at the closest approach and increases for nonzero values of ε. A negative angle ε indicates propagation in the region between spacecraft and proximate point; positive ε is used for the region between Earth and the proximate point. The difference between the times τ_{Up} and τ_{Down}, however, changes linearly. The plasma velocity is determined to be higher if the CME is propagating in a direction with negative ε and lower if in a direction with positive ε. The analysis results in reasonable CME velocities between 380 km/s and 600 km/s.

7.4.3. Coronal mass ejections

Coronal radio sounding is well suited for observing Coronal mass ejections (CMEs) that pass through the signal raypath. The method provides high temporal resolution (usually 1 sample per second), complementary to coronagraph images that provide the full spatial extent and structure of a CME. Whereas white-light images are usually taken at a cadence of minutes to hours, radio sounding data provides the fine-scale temporal structure at a certain fixed position.

Several CMEs or CME related events could be identified in the data during the four MEX solar conjunctions. Table 7.2 lists the 8 most distinct events with their solar offset distances and the times of start and end of recording. Fig. 7.11 shows the change in electron content for these events derived from differential Doppler observations using (7.3).

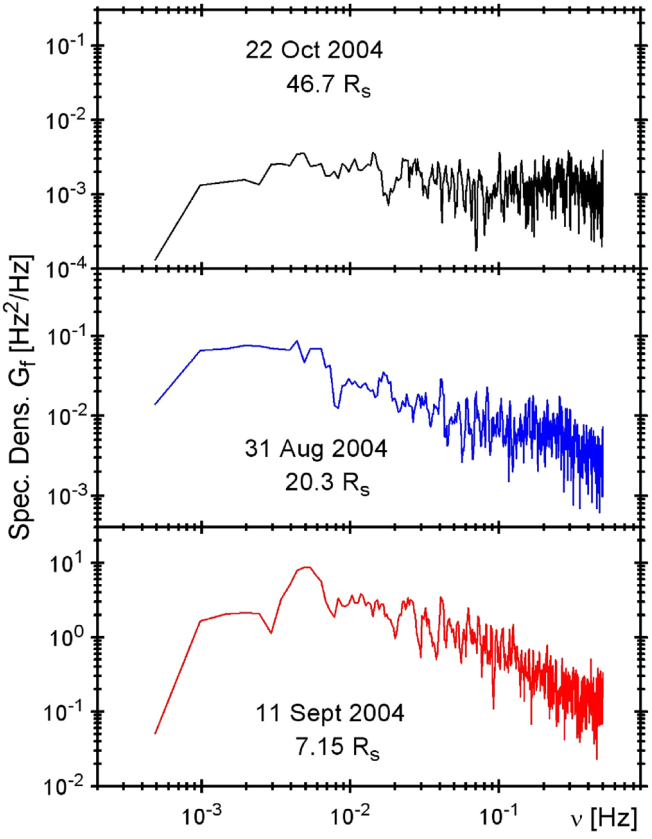

Fig. 7.12. MEX 2048-point RFF spectra. Upper panel: noise spectrum at large solar offset distance; Middle panel: typical power-law spectrum (80% of total) with a linear model fit used to determine the power-law index α over the interval 10^{-3} Hz $< \nu < 10^{-1}$ Hz; Bottom panel: spectrum with a Quasi-Periodic Component.

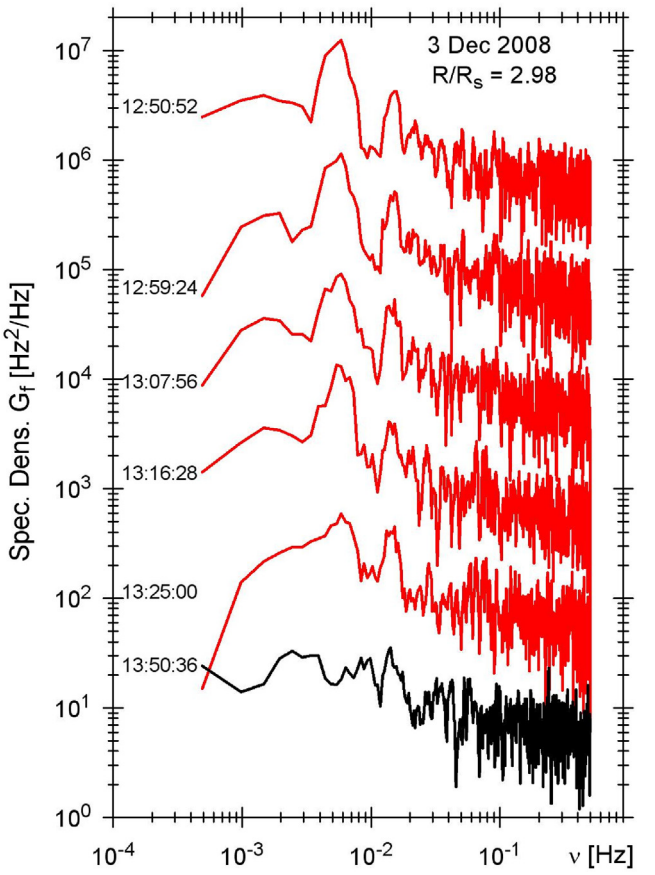

Fig. 7.13. Evolution of the QPC derived from MEX frequency fluctuations on 03 December 2008. The midpoint (UT) of the 2048-point interval associated with each spectrum is indicated. The length of the complete RFF record is 5632 s and the incremental time shift between spectra is 512 s. The MEX/Earth radio ray path was on the east solar limb (ingress) at a solar offset distance R ≈ _2.98 R⊛.

These CME observations were compared with coronagraph images taken by the LASCO coronagraph onboard the SOHO spacecraft (Pätzold et al., 2012)[3]. The LASCO (Large Angle and Spectroscopic Coronagraph, see Brueckner, et al., 1995) instrument consists of three white-light imagers that cover the solar corona at distances from 1.5 to 32 R⊛. The white-light intensity, which depends mainly on solar disk emission that is Thomson-scattered on electrons in the corona (November and Koutchmy, 1996), is thus directly comparable to the radio sounding observations of electron content. The observation geometry is also nearly the same for both methods. The SOHO spacecraft, located at the Lagrange point L1 between Earth and Sun, has the same viewing aspect of the solar corona as a radio tracking ground station on Earth. A detailed comparison of these observations can be found in Pätzold et al. (2012).

7.4.4. Radio frequency fluctuations: quasi-periodic component

The differential frequency residuals display significant fluctuations that increase toward smaller solar elongation. It has been known for many years that the mean frequency fluctuation level is directly related to the mean level of electron density fluctuations in the propagation medium. Moreover, the temporal spectrum of the radio frequency fluctuations (RFF) is related to the spectrum of coronal electron density irregularities. In order to study the electron density fluctuation spectrum in the inner heliosphere at different phases of the solar activity cycle, the RFF recordings are used as input to an extensive spectral analysis.

All solar wind parameters (magnetic field, density, velocity, etc.) display random fluctuations at virtually all spatial and temporal scales. The possibility of preferential turbulent frequencies in the corona would be of significance for determining the mechanisms of the solar wind acceleration to supersonic velocities. The presence of a quasi-periodic component (QPC) was discovered in some of the RFF spectra derived from radio science data acquired during the first MEX solar conjunction in 2004 (Efimov et al., 2010b). Meanwhile, further evidence has been found in data recorded at other solar conjunction opportunities from 1991 to 2009, thereby better defining the statistical characteristics of the QPC (Efimov et al., 2011, 2012). The QPC are also detected from a wavelet analysis, which has been shown capable of revealing oscillations with even longer periods (up to 1 hour or more) in the RFF data (Efimov et al., 2013).

Fig. 7.12 shows some typical examples of RFF spectra. Standard FFT (Fast Fourier ransform) algorithms were applied on RFF records with a sample time of 1 s and length 2048 s. The spectra are essentially flat, dominated by receiver noise, at large solar offsets (upper panel). Inside 30 R⊛, the most common form for the RFF spectrum is a power-law decrease with fluctuation frequency ν of the form $\nu^{-\alpha}$, where α is called the spectral index. (middle panel). Roughly 20% of the spectra display a distinct QPC (bottom panel).

The QPC appearance in the RFF records is evanescent. Fig. 7.13 displays the typical evolution for an example with MEX on 03 December 2008. Successive RFF spectra are presented from top to bottom with an incremental time shift of 512 s. The QPC, characterized by a rather

[3] See http://sohowww.nascom.nasa.gov.

broad maximum near $\nu_{max} \approx 5.69$ MHz, is already present at the start of the recording. The spectral amplitude at the QPC peak is nearly constant for the first four consecutive spectra and is about 5 times above the background spectral level. The QPC then faded and had disappeared completely for the bottom spectrum in Fig. 7.20. A higher frequency maximum at $\nu \approx 14.2$ MHz may possibly be a second harmonic of the QPC.The characteristic frequency of the QPC usually lies in the range 4-5 MHz, corresponding to a fluctuation period of about 4 min. The QPC has been observed both in equatorial regions and at high heliolatitudes and at heliocentric distances between 3 and 40 $R_\odot$. The QPC occurrence frequency of about 20% near the Sun ($3-6$ $R_\odot$) trends downward to about 12% at distances beyond 20 $R_\odot$. The present interpretation for the origin of the QPC are quasi-periodic electron density fluctuations associated with slow and fast mode magnetosonic waves. These modes are presumably generated locally from nonlinear interactions with a steady flux of Alfvén waves propagating upward from the coronal base.

8. Summary

In ten years of operation in Mars orbit, the Mars Express radio science experiment MaRS has achieved many objectives in the fields of atmospheric/ionospheric physics, geology, geophysics and solar science.

Although not yet fully covered over all seasons and local times on both planetary hemispheres, the MaRS occultations monitored the atmospheric conditions in the lower atmosphere from near the surface to about 50 km altitude. The boundary layer was investigated (Hinson et al., 2008a), and atmospheric waves, e.g. Kelvin waves, gravity waves from global to small scales were observed (Tellmann et al., 2013; Hinson et al., 2008b).

In contrast to MGS, MaRS is able to sound the entire ionosphere over the range of solar zenith angles from 55° (daytime) to 130° (night). MaRS followed the evolution of the ionosphere through the day, season and solar cycle (Withers et al., 2012a, 2012b; Peter et al., 2014), and documented the appearance of strange features (Withers et al., 2012a) and extra ionisation below the M1 layer (Pätzold et al., 2005) caused by the infall of meteors. Based on actual observation conditions, a MaRS model of the ionosphere has been developed (Peter et al., 2014) in order to verify the background neutral atmosphere model at ionospheric altitudes.

Ionospheric sounding at two coherent frequencies has proved to be highly advantageous. Features seen in the electron density profiles derived from the single X-band frequency or the dual-frequency differential Doppler could clearly be distinguished as either spacecraft induced or caused by the propagation of the radio signal through perturbed or turbulent plasma, respectively.

Many bistatic radar experiments (BSR) were performed over the past ten years, mostly at times near Earth/Mars opposition (Simpson et al., 2011). The two polarisations of the reflected radio signal were received on Earth by 70-m antennas of the Deep Space Network. Gradations of the dielectric constant were detected on horizontal scales of ten kilometers, implying that the surface is very heterogeneous, (Simpson et al., 2006b). In some exceptional cases, the shorter wavelength (X-band) yielded larger dielectric constants at single locations in the Northern plains (Simpson et al., 2006a), which can be interpreted as a centimeter size gravel and/or duricrust surface layer at these sites. MEX BSR detected extremely smooth isolated areas of several hundred km^2 near the poles. This detection came as a surprise and is not yet understood (Simpson et al., 2009).

The elliptical MEX orbit enabled two types of gravity investigations. The orbit perturbations induced during pericentre passes at 250 km over selected target areas were used to study the crustal structure of volcano bodies and valleys (Beuthe et al., 2007, 2012). The apocentre passes were used to reveal seasonal dependences of the low degree and order coefficients of the Martian gravity field caused by the condensation of CO2 over the local winter pole (Rosenblatt et al., 2008). In general, regular tracking data improved the ephemerides of the MEX and Phobos orbits (Rosenblatt et al., 2008; Lainey et al., 2007).

Several close Phobos flybys were performed in 2006, 2008 (Andert et al., 2010 Pätzold et al., 2014a) and 2013 which consolidated the Phobos mass within a range of 1% considering all past mass solutions (Pätzold et al., 2014b). A determination of the Phobos gravity coefficient C_{20} was attempted in 2010, but still has a large uncertainty (Pätzold et al., 2014a).

Planet Mars undergoes superior solar conjunction almost every two years. On these occasions the radio signals propagate through the solar corona and reveal the large-scale structure and turbulence of the coronal plasma. Together with the ESA spacecraft Rosetta and Venus Express, the coronal sounding observations cover a full solar cycle. The observations showed the change in coronal plasma turbulence over the solar cycle and (Pätzold et al., 2012), the occasional presence of a quasi-periodic component in the solar wind acceleration region (Efimov et al., 2010a, 2010b, 2011, 2012, 2013), and the detection and interpretation of CMEs and their velocities (Pätzold et al., 2012).

The MaRS radio science experiment will continue with its observations of the atmosphere and ionosphere over the next years. The investigation will be augmented by complementary observations on the MAVEN spacecraft, which arrived at Mars in September 2014.

Acknowledgements

The Mars Express Radio Science experiment (MaRS) is funded by the Bundesministerium für Wirtschaft BMWi, Berlin, via the German Space Agency DLR, Bonn, under grants 50QM1004, 50QM1401 and 50QM1002 (UniBw). Support for MaRS at Stanford University is provided by NASA through JPL contract 1217744. Support for the Multimission Radio Science Support Team is provided by NASA/JPL. We thank everyone involved with the Mars Express mission at ESTEC, ESOC, ESAC, JPL and in particular at the ESTRACK and DSN ground stations. The MaRS team expresses deep appreciation for the critical support provided by the MEX SGS at ESAC during the planning and the data acquisition periods. We are deeply indebted to Padma Varanasi and Tommy Thompson, both at JPL, for their dedicated support.

Appendix A

See Table A1.

Table A1
MEX Bistatic Radar Experiments Conducted 2004–2012.

Date	DOY	NASA DSN Antenna[a]	HGA[b]	Earth-Mars Distance (AU)	Notes
2003-08-27	239			0.373	Opposition
2004-05-21	141	14	I	2.303	
2005-02-27	058	43	I	1.843	
2005-04-03	093	43	I	1.584	
2005-04-10	100	43	I	1.534	
2005-04-24	114	14	I	1.436	
2005-07-06	187	43	I	0.975	
2005-07-24	205	14	I	0.873	
2005-08-26	238	14	I	0.694	
2005-08-27	239	63	I	0.689	
2005-08-31	243	63	I	0.668	
2005-09-06	249	63	I	0.637	
2005-10-01	274	14	I	0.525	
2005-10-19	292	14	I	0.474	
2005-10-30	303			0.464	Opposition
2005-10-31	304	63	I	0.464	
2005-11-04	308	63	I	0.466	
2005-12-10	344	14	I	0.607	
2005-12-12	346	63	I	0.621	
2006-01-21	021	14	I	0.956	
2006-01-22	022	14	S	0.966	
2006-04-02	092	63	I	1.654	
2006-04-07	097	63	I	1.702	
2006-04-08	098	14+AO	I	1.711	Arecibo S-Band reception
2006-04-21	111	43	I	1.830	
2006-04-23	113	43	I	1.848	
2006-05-30	150	14	S	2.147	
2006-06-24	175	43	S	2.316	
2006-08-10	222	43	S	2.528	
2007-12-19	353			0.589	Opposition
2008-01-25	025	63	S	0.727	
2008-02-03	034	63	S	0.794	
2008-02-08	039	63	S	0.835	
2008-02-23	054	43	S	0.968	
2008-02-29	060	43	S	1.024	
2008-03-23	083	14	S	1.249	
2008-07-03	185	63	S	2.124	
2008-08-18	231	14	S	2.363	
2009-04-19	109	63	S	2.129	
2009-04-25	115	63	S	2.111	
2009-06-26	177	14	S	1.912	
2009-06-27	178	14	S	1.908	
2009-07-03	184	14	S	1.886	
2009-07-04	185	14	S	1.882	
2009-07-12	193	14	S	1.850	
2009-07-18	199	14	S	1.826	
2009-08-14	226	14	S	1.706	
2009-08-22	234	14	S	1.659	
2009-09-03	246	63	S	1.592	
2009-09-12	255	14	S	1.538	
2009-09-13	256	14	S	1.531	
2009-09-17	260	14	S	1.506	
2009-10-11	284	14	S	1.342	
2009-10-18	291	14	S	1.291	
2010-01-18	018			0.664	Opposition
2010-02-10	041	14	S	0.684	
2010-02-20	051	14	S	0.723	
2010-02-24	055	14	S	0.744	
2010-04-16	106	63	S	1.150	
2010-04-25	115	43	S	1.232	
2010-05-01	121	63	S	1.287	
2010-05-08	128	43	S	1.350	
2010-05-15	135	63	S	1.412	
2010-05-22	142	63	S	1.474	
2010-06-06	157	63	S	1.600	
2010-06-19	170	63	S	1.703	
2010-07-03	184	63	S	1.807	
2010-08-06	218	43	S	2.022	
2010-08-12	224	63	S	2.054	
2012-02-07	038	14	S	0.756	
2012-02-15	046	63	S	0.717	
2012-03-06	066			0.674	Opposition
2012-04-08	099	63	S	0.783	
2012-04-10	101	43	S	0.796	
2012-04-20	111	63	S	0.862	

[a] NASA DSN antennas are near Barstow, CA (14), Canberra, Australia (43), and Madrid, Spain (63). At the time of the MEX BSR observation, Arecibo Observatory, near Arecibo, Puerto Rico, was operated by Cornell University for the National Science Foundation and NASA.
[b] I=inertial pointing; S=specular pointing.

References

Ahmad, B., Tyler, G.L., 1999. Systematic errors in atmospheric profiles obtained from abelian inversion of radio occultation data: effects of large-scale horizontal gradients. J. Geophys. Res. 104 (D4), 3971–3992.

Anderson, J. D., 1971. Feasibility of Determining the Mass of an Asteroid from a Spacecraft Flyby. In: Gehrels, T. (Ed.), Proc. of IAU Colloq. 12. National Aeronautics and Space Administration SP 267, Tucson, AZ, p. 577.

Anderson, J.D., Krisher, T.P., Borutzki, S.E., Connally, M.J., Eshe, P.M., Hotz, H.B., Kinslow, S., Kursinski, E.R., Light, L.B., Matousek, S.E., Moyd, K.I., Roth, D.C., Sweetnam, D.N., Taylor, A.H., Tyler, G.L., Gresh, D.L., Rosen, P.A., 1987. Radio range measurements of coronal electron densities at 13 and 3.6 centimeter wavelengths during the 1985 solar occultation of Voyager 2. Astrophys. J. Lett. 323, L141–L143.

Andert, T.P., Rosenblatt, P., Pätzold, M., Häusler, B., Dehant, V., Tyler, G.L., Marty, J.C., 2010. Precise mass determination and the nature of Phobos. Geophys. Res. Lett. 37, L09202. http://dx.doi.org/10.1029/2009GL041829.

Andrews, D.G., Holton, J.R., Leovy, C.B., 1987. Middle Atr. Elsevier, New York.

Avakyan, S.V., et al., 1998. Collision Processes and Excitation of UV Emission From Planetary Atmospheric Gases: A Handbook of Cross Sections. Gordon and Breach Science Publishers, Amsterdam and the Netherlands.

Banfield, D., Conrath, B.J., Smith, M.D., Christensen, P.R., Wilson, R.J., 2003. Forced waves in the martian atmosphere from MGS TES nadir data. Icarus 161, 319–345.

Barth, C.A., Stewart, A.I.F., Bougher, S.W., Hunten, D.M., Bauer, S.J., Nagy, A.F., 1992. Aeronomy of the Current Martian Atmosphere. In: Mars (Ed.), 1992. University Arizona Press, Arizona, pp. 1054–1089.

Berthias, J.-P., 1990. Analysis of the Phobos-2 radiometric data set 6th March 1990, 314-6, 1129, 1990. JPL Interoffice Memorandum.

Beuthe, M., Rosenblatt, P., Dehant, V., Barriot, J.-P., Pätzold, M., Häusler, B., Karatekin, Ö., Le Maistre, S., Van Hoolst, T., 2006. Assessment of the Martian gravity field at short wavelength with Mars Express. Geophys. Res. Lett. 33, L03203.

Beuthe, M., Le Maistre, S., Rosenblatt, P., Pätzold, M., Dehant, V., 2012. Density and lithospheric thickness of the Tharsis Province from MEX MaRS and MRO gravity data. J. Geophys. Res. 117, E04002.

Bird, M.K., 1982. Coronal investigations with occulted spacecraft signals. Space Sci. Rev. 33, 99–126.

Bird, M.K., Volland, H., Pätzold, M., Edenhofer, P., Asmar, S.W., Brenkle, J.P., 1994. The coronal electron density distribution determined from dual-frequency ranging measurements during the 1991 solar conjunction of the Ulysses spacecraft. Astrophys. J. 426, 373–381.

Brain, D.A., 2006. Mars Global Surveyor measurements of the Martian solar wind interaction. Space Sci. Rev. 126, 77–112. http://dx.doi.org/10.1007/s11214-006-9122-x.

Briggs, G.A., Leovy, C.B., 1974. Mariner 9 observations of the Mars north polar hood. Bull. Meteorol. Soc. 55, 278–296.

Brueckner, G.E., Howard, R.A., Koomen, M.J., Korendyke, C.M., Michels, D.J., Moses, J. D., Socker, D.G., Dere, K.P., Lamy, P.L., Llebaria, A., et al., 1995. The Large Angle Spectroscopic Coronagraph (LASCO). Sol. Phys. 162, 357–402.

Burns, J.A., 1992. Contradictory clues as to the origin of the Martian moons. In: Kiefer, H.H. (Ed.), Mars. University of Arizona Press, Tucson, pp. 1283–1301.

Campbell, M.J., Ulrichs, J., 1969. Electrical properties of rocks and their significance for lunar radar observations. J. Geophys. Res. 74, 5867–5881.

Carter, Lynn M., Campbell, Bruce, A., Watters, Thomas, R., Phillips, Roger, J., utzig, Nathaniel E., Safaeinili, Ali, Plaut, Jeffrey J., Okubo, Chris H., gan, Anthony F., Seu, Roberto, Biccari, Daniela, Orosei, Roberto, 2009. Shallow radar (SHARAD) sounding observations of the Medusae Fossae Formation, Mars. Icarus 199 (2), 295–302. http://dx.doi.org/10.1016/j.icarus.2008.10.007.

Chen, R.H., Cravens, T.E., Nagy, A.F., 1978. The Martian ionosphere in light of the Viking observations. J. Geophys. Res. 83, 3871–3876.

Chicarro, A., Martin, P., Trautner, R., 2004. The Mars Express Mission: An Overview SP-1240. ESA Special Publication, pp. 3–13.

Christensen, E.J., Born, G.H., Hildebrand, C.E., Williams, B.G., 1977. The mass of PHOBOS from Viking flybys. Geophys. Res. Lett. 4, 555–557.

Connerney, J.E.P., Acuna, M.H., Wasilewski, P.J., Kletetschka, G., Ness, N.F., Reme, H., Lin, R.P., Mitchell, D.L., 2001. Geophys. Res. Lett. 28 (21), 4015–4018.

Craddock, R.A., 2011. Are Phobos and Deimos the result of a giant impact? Icarus 211 (2), 1150–1161.

Creasey, J.E., Forbes, J.M., Hinson, D.P., 2006. Global and seasonal distribution of gravity wave activity in Mars' lower atmosphere derived from MGS radio occultation data. Geophys. Res. Lett. 33, 1803. http://dx.doi.org/10.1029/2005GL024037.

Duru, F., Gurnett, D.A., Frahm, R.A., Winningham, J.D., Morgan, D.D., Howes, G.G., 2009. Steep, transient density gradients in the Martian ionosphere similar to the ionopause at Venus. J. Geophys. Res. 114, A12310. http://dx.doi.org/10.1029/2009JA014711.

Efimov, A.I., Lukanina, L.A., Samoznaev, L.N., Rudash, V.K., Chashei, I.V., Bird, M.K., Pätzold, M., Tellmann, S., 2010a. Quasi-periodic fluctuations detected in Mars Express coronal radio sounding observations. In: Maksimovic, M., et al. (Eds.), Solar Wind, 12; 2010a, pp. 90–93.

Efimov, A.I., Lukanina, L.A., Samoznaev, L.N., Rudash, V.K., Chashei, I.V., Bird, M.K., Pätzold, M., Tellmann, S., 2010b. Coronal radio sounding experiments with Mars Express: Scintillation spectra during low solar activity. In: Maksimovic, M., et al. (Eds.), Solar Wind, 12; 2010b, pp. 94–97.

Efimov, A.I., Lukanina, L.A., Rogashkova, A.I., Samoznaev, L.N., Chashei, I.V., Bird, M. K., Pätzold, M., 2011. Dual-frequency radio sounding with spacecraft signals: quasi-periodic perturbations in the circumsolar plasma. J. Comm. Tech. Electron. 56 (12), 1407–1416.

Efimov, A.I., Lukanina, L.A., Samoznaev, L.N., Rudash, V.K., Chashei, I.V., Bird, M.K., Pätzold, M., 2012. Quasi-periodic frequency fluctuations observed during coronal radio sounding experiments 1991–2009 MEX VEX ROS Radio Science Team. Adv. Space Res. 49 (3), 500–508.

Efimov, A.I., Lukanina, L.A., Rogashkova, A.I., Samoznaev, L.N., Chashei, I.V., Bird, M. K., Pätzold, M., 2013. Quasi-periodic radio frequency fluctuations in the circumsolar plasma observed during radio-sounding experiments. J. Comm. Tech. Electron. 58 (5), 429–439.

Eshleman, V.R., 1975. Jupiter's atmosphere – problems and potential of radio occultation. Science 189, 876–878.

Fienga, A., Laskar, J., Morley, T., Manche, H., Kuchynka, P., Le Poncin-Lafitte, C., Budnik, F., Gastineau, M., Somenzi, L., 2009. INPOP08, a 4-D planetary ephemeris: from asteroid and time-scale computations to ESA Mars Express and Venus Express contributions. Astron. Astrophys. 507, 1675–1686.

Fjeldbo, G., Kliore, A.J., Eshleman, V.R., 1971. The Neutral Atmosphere of Venus as Studied with the Mariner V Radio Occultation Experiments. Astron. J. 76, 123.

Fjeldbo, G., 1964. Bistatic radar methods for studying planetary ionospheres and surfaces, Ph.D. thesis, Stanford University, SU-SEL-64-025, April.

Fjeldbo, G., Eshleman, V.R., 1965. The bistatic radar-occultation method for the study of planetary atmospheres. J. Geophys. Res. 70 (13), 3217–3225. http://dx.doi.org/10.1029/JZ070i013p03217.

Folkner, W.M., Williams, J.G., Boggs, D.H., 2008. The planetary and Lunar Ephemeris DE 421, Mem. IOM 343R-08-003, Jet Propul. Lab., Calif. Inst. Technol., Pasadena, California.

Fox, J.L., 2004. Advances in the aeronomy of Venus and Mars. Adv. Space Res. 33, 132–139.

Fox, J.L., Yeager, K.E., 2006. Morphology of the near-terminator Martian ionosphere: a comparison of models and data. J. Geophys. Res. 111, A10309. http://dx.doi.org/10.1029/2006JA011697.

Fox, J., Yeager, K.E., 2009. MGS electron density profiles: analysis of the peak magnitudes. Icarus 200, 468–479.

Fritts, D.C., Alexander, M.J., 2003. Gravity Wave Dynamics and Effects in the Middle Atmosphere. Rev. Geophys. 41 (1), 1003. http://dx.doi.org/10.1029/2001RG000106.

Gill, A.E., 1982. Atmosphere-Ocean Dynamics. 662. Academic Press, San Diego.

Giuranna, M., Grassi, D., Formisano, V., Montabone, L., Forget, F., Zasova, L., 2008. PFS/MEX observations of the condensing CO2 south polar cap of Mars. Icarus 197, 386–402.

Giuranna, M., Roush, T.L., Duxbury, T., Hogan, R.C., Carli, C., Geminale, A., Formisano, V., 2011. Compositional interpretation of PFS/MEx and TES/MGS thermal infrared spectra of Phobos. Planet. Space Sci. 59, 1308–1325.

Goldstein, R.M., 1969. Superior conjunction of Pioneer 6. Science 166, 598–601.

GRGS Team, 2012. Algorithmic documentation of the GINS software. Technical Report v1, CNES, December.

Häusler, B., Pätzold, M., Tyler, G.L., Simpson, R.A., Bird, M.K., Dehant, V., Barriot, J.-P., Eidel, W., Mattei, R., Remus, S., Selle, J., Tellmann, S., Imamura, T., 2006. Radio science investigations by VeRa onboard the Venus Express spacecraft. Planet. Space Sci. 54, 1315–1335.

Hall, A., 1878. Names of the satellites of Mars. Astronomische Nachrichten 92, 47.

Hanson, W.B., Sanatani, S., Zuccaro, D.R., 1977. The Martian ionosphere as observed by the Viking retarding potential analyzers. J. Geophys. Res. 82, 4351–4363.

Hanson, W.B., Mantas, G.P., 1988. Viking electron temperature measurements: evidence for a magnetic field in the Martian ionosphere. J. Geophys. Res. 93 (A7), 7538.

Hinson, D.P., Simpson, R.A., Twicken, J.D., Tyler, G.L., Flasar, F.M., 1999. Initial results from radio occultation measurements wit Mars Global Surveyor. J. Geophys. Res. 104, 26,997–27,012.

Hinson, D.P., Tyler, G.L., Hollingsworth, J.L., Wilson, R.J., 2001. Radio occultation measurements of forced atmospheric waves on Mars. J. Geophys. Res. 106, 1463–1480.

Hinson, D.P., Wilson, R.J., Smith, M.D., Conrath, B.J., 2003. Stationary planetary waves in the atmosphere of Mars during southern winter. J. Geophys. Res. Planets 108 (5004). http://dx.doi.org/10.1029/2002JE001949.

Hinson, D.P., Pätzold, M., Wilson, R.J., Häusler, B., Tellmann, S., Tyler, G.L., 2008a. Radio occultation measurements and MGCM simulations of Kelvin waves on Mars. Icarus 193, 125–138. http://dx.doi.org/10.1016/j.icarus.2007.09.009.

Hinson, D.P., Pätzold, M., Tellmann, S., Häusler, B., Tyler, G.L., 2008b. The depth of the convective boundary layer on Mars. Icarus 198, 57–66. http://dx.doi.org/10.1016/j.icarus.2008.07.003.

Hinson, D.P., Wang, H., 2010. Further observations of regional dust storms and baroclinic eddies in the northern hemisphere of Mars. Icarus 206, 290–305. http://dx.doi.org/10.1016/j.icarus.2009.08.019.

Hinson, D.P., Lewis, S.R., Pätzold, M., Tellmann, S., Häusler, B., Tyler, G.L., 2011. The depth of the convective boundary layer as observed by radio occultation with Mars Express, paper P21A-1645, Fall AGU Meeting, 5–9 December 2011, San Francisco, California.

Hinson, D.P., Wang, H., Smith, M.D., 2012. A multi-year survey of dynamics near the surface in the northern hemisphere of Mars: short-period baroclinic waves and dust storms. Icarus 219, 307–320. http://dx.doi.org/10.1016/j.icarus.2012.03.001.

Holton, J.R., 2004. An Introduction to Dynamical Meteorology, 4th ed. Academic Press, San Diego, p. 511.

Holmes, D.P., Simpson, R., Tyler, G.L., Pätzold, M., Dehant, V., Rosenblatt, P., Häusler, B., Goltz, G., Kahan, D., Valencia, J., Thompson, T., 2008. The challenges and opportunities for international cooperative radio science; Experience with the Mars Express and Venus Express Missions. Proc. AIAA/AAS Astrodynamics Specialist Conference 18, 2008-6395.
Hubbard, W.B., Hunten, D.M., Kliore, A., 1975. Effect of the Jovian oblateness on Pioneer 10/11 radio occultations. Geophys. Res. Lett. 2, 265–268.
Jacobson, R.A., 2008. The orbits of the Martian satellites. Bull. Am. Astron. Soc. 40, 481.
Jacobson, R.A., 2010. The orbits and masses of the Martian satellites and the libration of Phobos. Astron. J. 139, 668–679.
Jekeli, C., 2007. Potential theory and static gravity field of the Earth, in Treatise on Geophysics. In: Herring, T.A. (Ed.), Geodesy, vol. 3. Cambridge University Press, Cambridge, UK, pp. 11–42.
Jenkins, J.M., Steffes, P.G., Hinson, D.P., Twicken, J.D., Tyler, G.L., 1994. Radio occultation studies of the Venus atmosphere with the Magellan spacecraft. 2: Results from the October 1991 experiments. Icarus 110, 79–94.
Karayel, E.T., Hinson, D.P., 1997. Sub-Fresnel-scale vertical resolution in atmospheric profiles from radio occultation. Radio Sci. 32, 411–423.
Kaula, W.M., 1966. Theory of Satellite Geodesy. Blaisdell, Waltham, Mass.
Kliore, A.J., Cain, D.L., Levy, G.S., Eshleman, V.R., Fjeldbo, G., Drake, F.D., 1965. Occultation experiment: Results of the first direct measurement of Mars' atmosphere and ionosphere. Science 149, 1243–1248.
Kliore, A.J., Luhmann, J.G., 1991. Solar cycle effects on the structure of the electron density profiles in the dayside ionosphere of Venus. J. Geophys. Res. 96 (21), 281–21,289.
Kliore, A.J., 1992. Radio occultation observations of the ionospheres of Mars and Venus, in: Venus and Mars, Atmospheres, ionospheres and solar wind interactions, Proceedings of the Chapman Conference, Balatonfured, Hungary, June 4–8, Washington D.C., AGU, pp. 265–276.
Kolyuka, Y.F., Efimov, A.E., Kudryatsev, S.M., Margorin, O.K., Tarasov, V.P., Tikhonov, V.F., 1990. Refinement of the gravitational constant of Phobos from Phobos-2 tracking data. Sov. Astron. Lett. 16 (2), 168–170.
Konopliv, A.S., Yoder, C.F., Standish, E.M., Yuan, D.-N., Sjogren, W.L., 2006. A global solution for the Mars static and seasonal gravity, Mars orientation, Phobos and Diemos masses, and Mars ephemeris. Icarus 182, 23–50.
Konopliv, A.S., Yoder, C.F., Standish, E.M., Yuan, D.-N., Sjogren, W.L., 2006. A global solution for the Mars static and seasonal gravity, Mars orientation, Phobos and Deimos masses, and Mars ephemeris. Icarus 182, 23–50.
Konopliv, A.S., Asmar, S.W., Folkner, W.M., Karatekin, Ö., Nunes, D.C., Smrekar, S.E., Yoder, C.F., Zuber, M.T., 2011. Mars high resolution gravity fields from MRO, Mars seasonal gravity, and other dynamical parameters. Icarus 211, 401–428.
Kopp, E., 1997. On the abundance of metal ions in the lower ionosphere. J. Geophys. Res. 102, 9667–9675.
Lainey, V., Dehant, V., Pätzold, M., 2007. First numerical ephemerides of the Martian moons. Astron. Astrophys. 465 (1075), 2007. http://dx.doi.org/10.1051/0004-6361:20065466.
Lemoine, F.G., Smith, D.E., Rowlands, D.D., Zuber, M.T., Neumann, G.A., Chinn, D.S., Pavlis, D.E., 2001. An improved solution of the gravity field of Mars (GMM-2B) from Mars Global Surveyor 23,359-23,376. J. Geophys. Res. 106 (E10).
Levy, G.S., Sato, T., Seidel, B.L., Stelzried, C.T., Ohlson, J.E., Rusch, W.V.T., 1969. Pioneer 6: Measurement of transient Faraday rotation phenomena observed during solar occultation. Science 166, 596–598.
Lewis, S.R., et al., 1999. A climate database for Mars. J. Geophys. Res. 104 (E10), 24177–24194.
Lewis, S.R., Hinson, D.P., Spiga, A., 2011. Variations in martian convective boundary layer depth: Observations and modelling studies. In: Forget, F., Millour, E. (Eds.), Mars Atmosphere – Modelling and Observations, pp. 82–85.
Lipa, B., Tyler, G.L., 1979. Statistical and computational uncertainties in atmospheric profiles from radio occultation - Mariner 10 at Venus. Icarus 39, 192–208.
Marty, J.C., Balmino, G., Duron, J., Rosenblatt, P., Le Maistre, S., Rivoldini, A., Dehant, V., Van Hoolst, T., 2009. Martian gravity field model and its time variations from MGS and ODYSSEY data. Planet. Space Sci. 57 (3), 350–363. http://dx.doi.org/10.1016/j.pss.2009.01.004.
McCleese, D.J., et al., 2008. Intense polar temperature inversion in the middle atmosphere of Mars. Nat. Geosci. 1, 745–749. http://dx.doi.org/10.1038/ngeo332.
McCleese, D.J., et al., 2010. Structure and dynamics of the Martian lower and middle atmosphere as observed by the Mars Climate Sounder: Seasonal variations in zonal mean temperature, dust, and water ice aerosols. J. Geophys. Res. 115, E12016. http://dx.doi.org/10.1029/2010JE003677.
Mendillo, M., Smith, S., Wroten, J., Rishbeth, H., Hinson, D., 2003. Simultaneous ionospheric variability on Earth and Mars. J. Geophys. Res. 108, 1432.
Mendillo, M., Withers, P., Hinson, D., Rishbeth, H., Reinisch, B., 2006. Effects of solar flares on the ionosphere of Mars. Science 311, 1135–1138. http://dx.doi.org/10.1126/science.1122099.
Mendillo, M., Lollo, A., Withers, P., Matta, M., Pätzold, M., Tellmann, S., 2011. Modeling Mars' ionosphere with constraints from same-day observations by Mars Global Surveyor and Mars Express. J. Geophys. Res. 116, A11303. http://dx.doi.org/10.1029/2011JA016865.
Mignard, F., 1981. Evolution of the Martian Satellites, 194. MNRAS, pp. 365–379.
Millour, E., F. Forget et al., 2011. An improved Mars Climate Database, The 4th Intl. WS on Mars Atmosphere Modeling and Observations, Paris, 8–11 February.
Mitchell, D.L., Lin, R.P., Mazelle, C., Rème, H., Cloutier, P.A., Connerney, J.E.P., Acuña, M.H., Ness, N.F., 2001. Probing Mars' crustal magnetic field and ionosphere with the MGS Electron Reflectometer. J. Geophys. Res. 106 23,419–23,428.
Molina-Cuberos, G.J., Witasse, O., et al., 2003. Meteoric ions in the atmosphere of Mars. Planet. Space Sci. 51 (3), 239–249.
Morabito, D.D., Shambayati, S., Finley, S., Fort, D., 2003. , The Cassini May 2000 solar conjunction. IEEE Trans. Antennas Propag. 51, 201–219.
Morgan, D.D., Gurnett, D.A., Kirchner, D.L., Fox, J.L., Nielsen, E., Plaut, J.J., 2008. Variation of the Martian ionospheric electron density from Mars Express radar soundings, J. Geophys. Res. (Space Phys). 113, A09303. http://dx.doi.org/10.1029/2008JA013313.
Moyer T.D., 1971. Mathematical formulation of the double-precision orbit determination program (DPODP), JPL Tech. Rep. 32-1527, Jet Propul. Lab., Pasadena, Calif.
Muhleman, Duane O., Butler, Bryan, J., Grossman, Arie, W., Slade, Martin, A., 1991. Radar images of Mars (ISSN 0036-8075). Science 253, 1508–1513.
Nagy, A.F., et al., 2004. The plasma environment of Mars. Space Sci. Rev. 111, 33–114. http://dx.doi.org/10.1023/B:SPAC.0000032718.47512.92.
November, L.J., Koutchmy, S., 1996. White-light coronal dark threads and density fine structure. Astrophys. J. 466, 512–528.
Owen, T., 1992. The composition and early history of the atmosphere of Mars}, in Mars, Editor: M. George, 818-834, Honolulu.
Pätzold, M., Bird, M.K., Edenhofer, P., Asmar, S.W., McElrath, T.P., 1995. Dual-frequency radio sounding of the solar corona during the 1995 conjunction of the Ulysses spacecraft. Geophys. Res. Lett. 22, 3313–3316.
Pätzold, M., Wennmacher, A., Häusler, B., Eidel, W., Morley, T., Thomas, N., Anderson, J.D., 2001. Mass and density determinations of 140 Siwa and 4979 Otawara as expected from the Rosetta flybys. Astron. Astrophys. 370, 1122–1127.
Pätzold, M., Neubauer, F.M., Carone, L., Hagermann, A., Stanzel, C., Häusler, B., Remus, S., Selle, J., Hagl, D., Hinson, D.P., Simpson, R.A., Tyler, G.L., Asmar, S.W., Axford, W.I., Hagfors, T., Barriot, J.-P., Cerisier, J.-C., Imamura, T., Oyama, K.-I., Janle, P., Kirchengast, G., Dehant, V., 2004. MaRS: Mars Express Orbiter radio science. In: Wilson, A. (Ed.), Mars Express: The Scientific Payload. ESA, Noordwijk, pp. 141–163.
Pätzold, M., Tellmann, S., et al., 2005. A Sporadic Third Layer in the Ionosphere of Mars. Science 310, 837–839.
Pätzold, M., Häusler, B., Aksnes, K., Anderson, J.D., Asmar, S.W., Barriot, J.-P., Bird, M. K., Boehnhardt, H., Eidel, W., Grün, E., et al., 2007. Rosetta radio science investigations (RSI). Space Sci. Rev. 128, 599–627.
Pätzold, M., et al., 2009a. MaRS: Mars Express Radio Science Experiment SP-1291. Mars Express: The Scientific Investigations. European Space Agency, Special Publication, pp. 217–245.
Pätzold, M., Tellmann, S., Häusler, B., Bird, M.K., Tyler, G.L., Christou, A.A., Withers, P., 2009b. A sporadic layer in the Venus lower ionosphere of meteoric origin. Geophys. Res. Lett. 36, L05203. http://dx.doi.org/10.1029/2008GL035875.
Pätzold, M., Andert, T.P., Asmar, S.W., Anderson, J.D., Barriot, J.-P., Bird, M.K., Häusler, B., Hahn, M., Tellmann, S., Sierks, H., Lamy, P., Weiss, B.P., 2011. Asteroid 21 Lutetia: low mass, high density. Science 334, 491.
Pätzold, M., Hahn, M., Tellmann, S., Häusler, B., Bird, M.K., Tyler, G.L., Asmar, S.W., Tsurutani, B.T., 2012. Coronal Density Structures and CMEs: Superior Solar Conjunctions of Mars Express, Venus Express, and Rosetta: 2004, 2006, and 2008. Sol. Phys. 279, 127–152.
Pätzold, M., Andert, T., Häusler, B., Tellmann, S., Tyler, G.L., 2012. Ashes To Ashes, Dust To Dust: Phobos, The Life And Fate Of An Inhomogeneous Moon Of Second Generation DPS meeting #44, #211.01. American Astronomical Society.
Pätzold, M.T., Andert, G.L., Tyler, S.W., Asmar, B., Häusler, S., 2014a. Tellmann, Phobos mass determination from the very close flyby of Mars Express in 2010. Icarus 229, 92–98. http://dx.doi.org/10.1016/j.icarus.2013.10.021.
Pätzold, M., Andert, T.P., Jacobson, R., Rosenblatt, P., Dehant, V., 2014b. Phobos: observed bulk properties. Planet. Space Sci. 102, 86–94. http://dx.doi.org/10.1016/j.pss.2014.01.004.
Pavlis, D.E., Poulouse, S.G., Rowton, S.C., McCarthy, J.J., 2001. GEODYN Operations Manuals. Contractor Report, Raytheon ITTS, Lanham, MD.
Pavlis, D.E., Poulose, S., McCarthy, J.J., 2006. GEODYN Operations Manuals, contractor report, SGT Inc., Greenbelt, MD.
Pesnell, W.D., Grebowsky, J., 2000. Meteoric magnesium ions in the Martian atmosphere. J. Geophys. Res. 105 (E1), 1695–1707.
Peter, K., 2008. Beobachtungen der Ionsophären- und Ionopausenstrukturen des Mars mit dem Radio Science Experiment MaRS auf Mars Express. Universität zu Köln, Diplomarbeit, IGM.
Peter, K., Pätzold, M., Molina-Cuberos, G., Witasse, O., Gonzalez-Galindo, F., Withers, P., Bird, M.K., Häusler, B., Hinson, D.P., Tellmann, S., Tyler, G.L., 2014. The dayside ionospheres of Mars and venus: comparing a one-dimensional photochemical model with MaRS (Mars Express) and VeRa (Venus Express) observations. Icarus 233, 66–82.
Picardi, G.D., Biccari, R., Seu, J., Plaut, W.T.K., Johnson, R.L., Jordan, A., Safaeinili, D.A., Gurnett, R., Huff, R., Orosei, O., Bombaci, D., Calabrese, E., 2004. Zampolini, MARSIS: Mars Advanced Radar for Subsurface and Ionosphere Sounding SP1240. ESA Special Publication, pp. 51–69.
Pulido-Cobo, J.A., Schoenmaekers, J., 2004. Combined control of the operational Mars Express orbit and the spacecraft angular momentum, 18th international symposium on space flight dynamics, October 11–15th 2004, Munich, Germany.
Rishbeth, H., Mendillo, M., 2004. Ionospheric layers of Mars and Earth, Plan. Space Sci. 52 (9), 849–852.
Rosenblatt, P., Lainey, V., Le Maistre, S., Marty, J.C., Dehant, V., Pätzold, M., van Hoolst, T., Häusler, B., 2008. Accurate Mars Express orbits to improve the determination of the mass and ephemeris of the Martian moons. Planet. Space Sci. 56, 1043–1053. http://dx.doi.org/10.1016/j.pss.2008.02.004.

Rosenblatt, P., Dehant, V., 2010. Mars geodesy, rotation and gravity. Res. Astron. Astrophys. 10 (8), 713–736.
Rosenblatt, P., 2011. The origin of the Martian moons revisited. Astron. Astrophys. Rev. 19 (4).
Sanchez-Cano, B., Radicella, S.M., Herraiz, M., Witasse, O., Rodriguez-Caderot, G., 2013. NeMars: An empirical model of the martian dayside ionosphere based on Mars Express MARSIS data. Icarus 225, 236–247.
Sasaki, S., 1990. Long-term orbital evolution of a captured satellite (Phobos) in a primary atmosphere. Meteoritics 25, 404.
Shinagawa, H., 2000. Our current understanding of the ionosphere of Mars. Adv. Space Res. 26, 1599–1608.
Simpson, R.A., 1993. Spacecraft studies of planetary surfaces using bistatic radar. IEEE Trans. Geosci. Remote Sens. 31 (2), 465–482.
Simpson, R.A., Tyler, G.L., Pätzold, M., and Häusler, B., 2006aMars Express bistatic radar observations in northern plains with possible application to Phoenix landing site characterization, paper 1862, *37th Lunar and Planetary Science Conference*, Houston, TX, March 13–17.
Simpson, R.A., Tyler, G.L., Pätzold, M., Häusler, B., 2006b. Determination of local surface properties using Mars Express bistatic radar. J. Geophys. Res. 111, E06S05. http://dx.doi.org/10.1029/2005JE002580.
Simpson, R.A., Tyler, G.L., Nolan, M.C., Pätzold, M., Häusler, B., 2006cMars Express bistatic radar explores Stealth, paper 67.06, AAS Division for Planetary Science 38th Annual Meeting, Pasadena, CA, October 8–13.
Simpson, R.A., Tyler, G.L., Pätzold, M., Häusler, B., 2009. Bistatic radar probing of planetary surfaces, abstract 3071, RADARCON9, Pasadena, CA, May 4–8.
Simpson, R.A., Tyler, G.L., Pätzold, M., Häusler, Bernd, Asmar, Sami W., Sultan-Salem, Ahmed K., 2011. Polarization in bistatic radar probing of planetary surfaces: application to Mars Express data. Proc. IEEE 99 (5), 858–874.
Singer, S.F., 2007. Origin of the Martian satellites Phobos and Deimos. LPI Contributions 1377, 36.
Schunk, R.W., Nagy, A.F., 2009. Ionospheres: Physics, Plasma Physics, and Chemistry, 2nd edition. Cambridge University Press, Cambridge and others.
Smith, M.D., 2004. Interannual variability in TES atmospheric observations of Mars during 1999–2003. Icarus 167, 148–165.
Smith, D.E., Zuber, M.T., Frey, H.V., Garvin, J.B., Head, J.W., Muhleman, D.O., Pettengill, G.H., Phillips, R.J., Solomon, S.C., Zwally, H.J., Banerdt, W.B., Duxbury, T. C., Golombek, M.P., Lemoine, F.G., Neumann, G.A., Rowlands, D.D., Aharonson, O., Ford, P.G., Ivanov, A.B., Johnson, C.L., McGovern, P.J., Abshire, J.B., Afzal, R.S., Sun, X., 2001a. Mars Orbiter Laser Altimeter: experiment summary after the first year of global mapping of Mars. J. Geophys. Res. (Planets) 106, 23689–23722. http://dx.doi.org/10.1029/2000JE001364.
Smith, D.E., Lemoine, F.G., Zuber, M.T., 1995. Simultaneous estimation of the masses of Mars, Phobos and Deimos using spacecraft distant encounters. Geophys. Res. Lett. 22 (2), 171–2,174.
Smith, M.D., Pearl, J.C., Conrath, B.J., Christensen, P.R., 2001b. Thermal Emission Spectrometer results: Mars atmospheric thermal structure and aerosol distribution. J. Geophys. Res. 106, 23929–23945.
Soja, B., Heinkelmann, R., Schuh, H., 2014. Probing the solar corona with very long baseline interferometry Article number: 4166. Nat. Commun. 5. http://dx.doi.org/10.1038/ncomms5166.
Spiga, A., Forget, F., Lewis, S.R., Hinson, D.P., 2010. Structure and dynamics of the convective boundary layer on Mars as inferred from large-eddy simulations and remote-sensing measurements. Q. J. R. Meteorol. Soc. 136, 414–428.
Tellmann, S., Pätzold, M., Häusler, B., Hinson, D.P., Tyler, G.L., 2013. The structure of Mars lower atmosphere from Mars Express Radio Science (MaRS) occultation measurements. J. Geophys. Res. Planets 118, 306–320. http://dx.doi.org/10.1002/jgre.20058.
Tolson, R.H., Blackshear, W.T., Mason, M.L., 1977. The mass of PHOBOS. J. Geophys. Res. 4, 551–554.
Tolson, R.H., et al., 1978. Viking first encounter of PHOBOS: preliminary results. Science 199, 61–64.
Thuillot, W., Lainey, V., Dehant, V., De Cuyper, J.P., Arlot, J.E., Gurvits, L., Hussmann, H., Oberst, J., Rosenblatt, P., Marty, J.C., Vermeersen, B., Robert, V., Dirckx, D., Kudryashova, M., Le Maistre, S., 2012. ESPaCE: European Satellite Partnership for Computing Ephemerides Space Research achievements under the 7th Framework Programme is published by the Space Research and Development Unit in the European Commission's Directorate-General for Industry and Enterprise, Chapter 25. Proc. "Let's embrace space", Volume II. Luxembourg Publications Office of the European Union, pp. 291–297. http://dx.doi.org/10.2769/31208.
Tobie, G., Forget, F., Lott, F., 2003. Numerical simulation of the winter polar wave clouds observed by Mars Global Surveyor Mars Orbiter Laser Altimeter. Icarus 164, 33–49.
Tobiska, W.K., et al., 2000. The SOLAR2000 empirical solar irradiance model and forecast tool. J. Atmos. Sol.-Terr. Phys. 62 (14), 1233–1250.
Tyler, G.L., Balmino, G., Hinson, D.P., Sjogren, W.L., Smith, D.E., Simpson, R.A., Asmar, S.W., Priest, P., Twicken, J.D., 2001. Radio science observations with Mars Global Surveyor: orbit insertion through one Mars year in mapping orbit. J. Geophys. Res. 106, 23327–23348.
Volland, H., Bird, M.K., Levy, G.S., Stelzried, C.T., Seidel, B.L., 1977. Helios-1 Faraday rotation experiment: results and interpretations of the solar occultations in 1975. J. Geophys. 42, 659–672.
Watters, T.R., Campbell, B.A., Carter, L.M., Leuschen, C.J., Plaut, J.J., Picardi, G., Safaeinili, A., Clifford, S.M., Farrell, W.M., Ivanov, A.B., Phillips, R.J., Stofan, E.R., and the MARSIS Science Team, 2007. MARSIS Subsurface Radar Sounding of the Medusae Fossae Formation, Mars, 38th Lunar and Planetary Science Conference, (Lunar and Planetary Science XXXVIII), held March 12-16, 2007 in League City, Texas. LPI Contribution No. 1338, p. 1661.
Wedlund, S.C., Gronoff, G., et al., 2011. Comprehensive calculation of the energy per ion pair or W values for five major planetary upper atmospheres. Ann. Geophys. 29 (1), 187–195.
Williams, B.G., Duxbury, T.C., Hildebrand, C.E., 1988. Improved Determination of PHOBOS and Deimos Masses from Viking Fly - Bys. LPI Contributions 1647, 1274.
Willner, K., Oberst, J., Hussmann, H., Giese, B., Hoffmann, H., Matz, K.D., Roatsch, T., Duxbury, T., 2010. Phobos control point network and shape. Earth Planet. Sci. Lett 294, 541–546.
Wilson, R.J., 2002. Evidence for nonmigrating thermal tides in the Mars upper atmosphere from the Mars Global Surveyor Accelerometer Experiment. Geophys. Res. Lett. 29 (NO. 7), 1120. http://dx.doi.org/10.1029/2001GL013975.
Witasse, O., Nagy, A.F., 2006. Outstanding aeronomy problems at Venus. Planet. Space Sci. 54 (13–14), 1381–1388.
Witasse, O., et al., 2014. Mars Express investigations of Phobos and Deimos. Planet. Space Sci. 102, 18–34.
Withers, P., 2009. A review of observed variability in the dayside ionosphere of Mars. Adv. Space Res. 44, 277–307. http://dx.doi.org/10.1016/j.asr.2009. 04.027.
Withers, P., Fallows, K., Girazian, Z., Matta, M., Häusler, B., Hinson, D.P., Tyler, G.L., Morgan, D., Pätzold, M., Peter, K., Tellmann, S., Peralta, J., Witasse, O., 2012a. A clear view of the multifaceted dayside ionosphere of Mars. Geophys. Res. Lett 39, L18202. http://dx.doi.org/10.1029/2012GL053193.
Withers, P., Fillingim, M.O., Lillis, R.J., Häusler, B., Hinson, D.P., Tyler, G.L., Pätzold, M., Peter, K., Tellmann, S., Witasse, O., 2012b. Observations of the nightside ionosphere of Mars by the Mars Express Radio Science Experiment (MaRS) CiteID A12307. J. Geophys. Res.: Space Phys 117 (A12).
Withers, P., Christou, A.A., Vaubaillon, J., 2013. Meteoric ion layers in the ionospheres of venus and mars: early observations and consideration of the role of meteor showers. Adv. Space Res. 52, 1207–1216.
Wohlmuth, R., Plettemeier, D., Edenhofer, P., Bird, M.K., Asmar, S.W., 1997a. Analysis of Galileo Doppler measurements during the solar occultations in 1994 and 1995. In: Barbieri, C., Rahe, J.H., Johnson, T.V. (Eds.), The Three Galileos: The Man, The Spacecraft, The Telescope. Kluwer, Dordrecht, pp. 421–428.
Wohlmuth, R., Plettemeier, D., Edenhofer, P., Bird, M.K., Pätzold, M., Asmar, S.W., 1997b. Measurement of the propagation speed of plasma inhomogeneities in the solar corona using an uplink/downlink correlation method. Radio Sci. 32, 617–628.
Woo, R., 1978. Radial dependence of solar wind properties deduced from Helios 1/2 and Pioneer 10/11 radio scattering observations. Astrophys. J. 219, 727–739 [Erratum, Astrophys. J. 223, 704–705, 1978].
Woo, R., Armstrong, J.W., 1979. Spacecraft radio scattering observations of the power spectrum of electron density fluctuations in the solar wind. J. Geophys. Res. 84, 7288–7296.
Yeomans, D.K., Barriot, J.-P., Dunham, D.W., Farquhar, R.W., Giorgini, J.D., Helfrich, C. E., Konopliv, A.S., McAdams, J.V., Miller, J.K., Owen Jr., W.M., Scheeres, D.J., Synnott, S.P., Williams, B.G., 1997. Estimating the Mass of Asteroid 253 Mathilde from Tracking Data During the NEAR Flyby. Science 278, 2106.
Zhang, M.H.G., Luhmann, J.G., Kliore, A.J., Kim, J., 1990. A post-Pioneer Venus reassessment of the Martian dayside ionosphere as observed by radio occultation methods. J. Geophys. Res. 95, 14,829–14,839.
Zurek, R.W., Barnes, J.R., Haberle, R.M., Pollack, J.B., Tillman, J.E., Leovy, C.B., 1992. Dynamics of the atmosphere of Mars, Mars. University of Arizona Press, Tucson, pp. 835–933.